MECHANISMS FOR AERODYNAMIC FORCE GENERATION AND FLIGHT STABILITY IN INSECTS

By
Chao Zhang

A dissertation submitted to Johns Hopkins University in conformity with the requirements for the degree of Doctor of Philosophy

Baltimore, Maryland
February, 2015

A B S T R A C T

The motivation of the current study is to explore two major aspects of flapping flight in insects: the aerodynamic mechanisms that are employed by flying insects to generate lift, and the strategies employed by insects to stabilize their flight in quiescent as well as perturbed aerodynamic environments.

Regarding the former, despite intense study by physicists, biologists and engineers, we do not yet fully understand the unsteady aerodynamics that relate insect wing morphology and kinematics to lift generation. Here, we formulate a force partitioning method (FPM) and implement it within a computational fluid dynamic model to provide an unambiguous and physically insightful division of aerodynamic force into components associated with wing kinematics, vorticity, and viscosity. Application of the FPM to hawkmoth and fruit fly flight shows that while the leading-edge vortex is the dominant mechanism for lift generation, there is another, previously unidentified mechanism, the centripetal acceleration reaction force, which generates significant net lift. The centripetal acceleration reaction lift is power-efficient, and insensitive to Reynolds number and to environmental flow perturbations, making it an important contributor to insect flight stability and miniaturization.

The FPM method developed here has wide ranging applications to virtually all fields of fluid dynamics, and in particular, to vortex dominated flows and flows with dynamically moving bodies. Similarly, the centripetal acceleration reaction force that has been identified here likely plays an important role in flows that involve bodies undergoing complex motions such as those encountered in the flying and swimming of

animals, flow-induced vibration and deformation in biology and engineering, and multiphase flows.

In a quest to explore strategies employed by hovering insects to stabilize their flight, the intrinsic stability of a hovering hawkmoth is analyzed. Analysis starts with the simplest model - a three degree-of-freedom (3DoF) linear time-invariant (LTI) model, and proceeds through 6DoF LTI to linear time-periodic (Floquet) models, and ends with a fully coupled fluid-body interaction (FBI) model which couples a Navier-Stokes solver with the 6DoF equations of motion of a freely flying hawkmoth. The well-accepted notion that the most unstable mode is a longitudinal (pitching) mode is challenged by the 6DoF LTI analysis that shows that there exists a lateral mode that is as unstable as the unstable longitudinal mode. Comparison of the flapping wing model with an equivalent revolving wing model also shows that the revolving wing model is more unstable than the flapping wing flyer. The results of the FBI model indicate that the hovering hawkmoth is more unstable in pitch than that predicted by the LTI model and that the location of center-of-mass (CoM) of hawkmoth relative to the neutral stability axis is the crucial element for stability.

High speed videos of a freely hovering hawkmoth indicate that control of the CoM location relative to the neutral axis may be accomplished by the hawkmoth via rotation of the body relative the wing plane. Motivated by this, a simple sensory-motor control strategy for hover stabilization that relies on visual and mechanosensory feedback to drive small changes in the relative pitch between the body and the wing is hypothesized. Simulations are used to explore the viability of this control strategy as well as to determine the gains and latencies required by the sensory-motor control system to

accomplish stabilization. Results suggest that the proposed strategy is indeed effective and viable given our current knowledge of insect response to aerodynamic perturbation and their sensory-motor control apparatus. The same strategy could potentially be employed in bio-inspired flapping wing micro-aerial vehicles.

Advisor: Rajat Mittal

Reader: Tyson L. Hedrick

Tamer Zaki

A c k n o w l e d g e m e n t s

First and foremost I would like to express my deepest gratitude to my advisor, Professor Rajat Mittal, Professor of Mechanical Engineering Department at Johns Hopkins University, for his insightful guidance on my research and considerable help on my studies. I would never have been able to finish this dissertation without his guidance, help, encouragement and support. It has been a great experience to me working with him. I would also like to sincerely appreciate Professor Tyson L. Hedrick, Professor of the Department of Biology at University of North Carolina at Chapel Hill, for providing very valuable guidance from an experimental perspective. In addition, I would also like to thank Professor Tamer Zaki, Professor of Mechanical Engineering Department at Johns Hopkins University, for providing valuable comments on the thesis.

I would like to thank other current and former colleagues at the Flow Simulations and Analysis Group, Dr. Lingxiao Zheng, Dr. Jung-Hee Seo and Dr. Vijay Vedula for their suggestions and help. Special thanks go to Dr. Lingxiao Zheng for his well-done work on the reconstruction of hawkmoth wing kinematics.

I would also like to thank my parents. They were always supporting and encouraging me with their best wishes. They were always there cheering me up and stood by me through those ups and downs.

Finally, I would like to thank the AFOSR for their financial support through grant FA9550-10-1-0062 and the NSF for computer resource support through NICS grant TG-CTS100002.

TABLE OF CONTENTS

LIST OF TABLES

LIST OF FIGURES

CHAPTER 1. INTRODUCTION

Insects and other flying animals support themselves in the air using flapping wings which rely on aerodynamic mechanisms different from those found in man-made rotary and fixed wing configurations. Moreover, the unsteady aerodynamics of beating insect wings typically provide higher lift coefficients than these conventional wings, facilitating phenomenal flight performance over a variety of scales ranging from a few millimeters to tens of centimeters (Ellington, et al., 1984). Investigation of these unsteady mechanisms and associated flow features has a long history and ingenious experiments have been devised to delineate the individual contributions of these various mechanisms and features (Ellington, et al., 1996; VandenBerg, et al., 1997; Birch, et al., 2001; Birch, et al., 2004). These studies have showed the importance of the leading-edge vortex (LEV), which forms on a flapping wing operating at high angle of incidence with the surrounding fluid. In addition to the delayed shedding of this LEV ('delayed stall'), other unsteady mechanisms such as the clap-and-fling (Spedding, 1986), wing rotation (Dickinson, et al., 1999) and wake-capture (Birch, et al., 2003) have also been identified via these studies. However, experiments are limited in their ability to simultaneously measure velocity and vorticity in the three-dimensional flow-field, as well as the pressure and shear on the wing surface. This limits the extent to which individual contributions of various mechanisms can be delineated. For instance, to investigate lift production of fruit-fly flight at Reynolds number 100, Dickinson, et al. (1999) conducted a series of scaled solid fruit-fly wing flapping experiments to determine the various mechanisms and features that are responsible for the lift generation in flapping wings. In their experiments, the

mechanical fruit-fly wing is flapped in a prescribed way as shown in Fig 1-1(a). The strategy they employed was to separate the total lift into a quasi-steady component and a `rotational' lift component. The quasi-steady component is the lift generated by the wing revolving at a constant velocity (equal to the instantaneous velocity of the flapping wing) at the instantaneous angle-of-attack of the flapping wing. The rotational lift is the difference between the total lift and the quasi-steady lift. The idea behind this decomposition was that the rotational lift captures all the component and mechanisms that are unique to the flapping of the wing. As shown Fig 1-1(b), significant positive peaks in rotational lift were found at the beginning of upstroke and downstroke and these were attributed to the circulation enhancement due to wing rotation and wake capture. However, there are a number of issues with this decomposition: first, this decomposition does not fully delineate the contribution of vorticity to the lift since both the quasi-steady and rotational components contain the influence of vorticity. Furthermore, at anything but the very low Reynolds numbers, non-linear interactions make such a decomposition difficult. Thirdly, wake capture is a unique mechanism that is not expected to play a role in the hovering flight of all insects and finally, the experimental of Dickinson et al. (1999) did not account for wing flexibility and deformation, phenomena that are quite common in insect flight. Thus, while these studies were groundbreaking and insightful, a clear understanding of the aerodynamic mechanisms that generate the lift required to stay aloft, remained elusive.

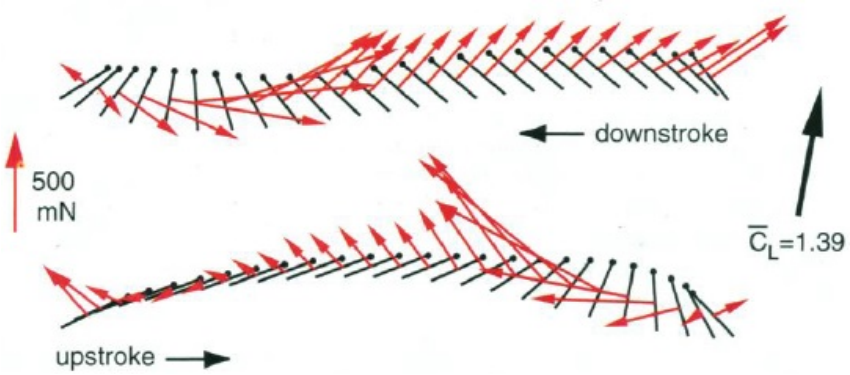

(a)

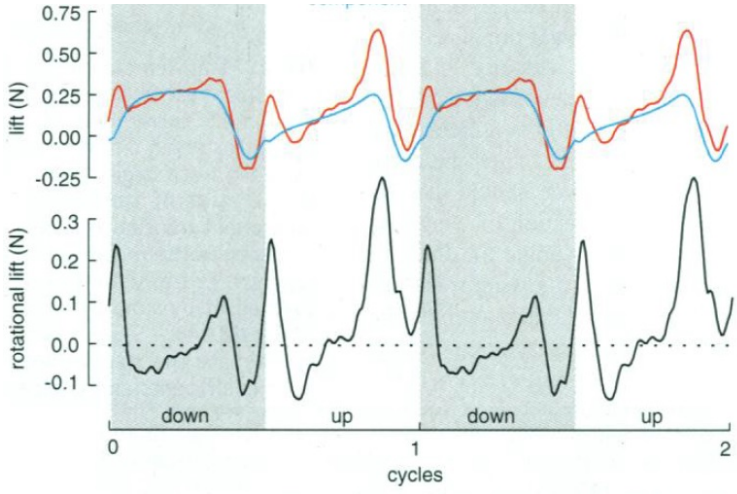

(b)

Figure 1-1 (a) Mechanical fruit-fly flapping wing kinematics from Dickinson, et al. (1999); (b) The time series of measured lift (red), quasi-steady estimation of lift (blue) and the discrepancy between them ("rotational" lift, black) (from Dickinson, et al. (1999)).

1.1. Force Partitioning Method for Deforming Body in Incompressible Flow

In history of fluid mechanics, the first well-known investigation on the mechanism of aerodynamic or hydrodynamic force production can be traced back to D'Alembert in 1752. The D'Alembert' paradox states that for an incompressible, inviscid potential flow, the drag force on a body moving through the fluid with constant velocity is zero. In 1828 Friedrich Bessel introduced the concept of added-mass effect to complete the classical theory of force production in potential flow. Added-mass, also called the force due to acceleration reaction, is the force produced by a body accelerating in an inviscid irrotational fluid, and is associated with the reaction to the acceleration of the fluid around the body. Fluid mechanists and mathematicians however realized that the force and moment exerted on a solid body immersed in a viscous incompressible fluid, are not merely contributed by the added-mass effect but also strongly depend on the vortex structures around it. In order to satisfy the momentum balance for the whole system, the momentum gained or lost to the internal body has to exactly match the momentum change of the fluid in the control volume, which in turn is affected by vortices. In this context, significant attention has been given to the mechanism (fluid phenomena and/or flow featrues) for the generation of force/moment on a body moving in a fluid. As quoted in J. Z. Wu's book-*Vorticity and Vortex Dynamics*, "The ultimate concern of aerodynamics, also its unique task, is expressing the force and moment in a way that can precisely capture the key physical mechanisms contributing to these integrated performances."

Thanks to its inherent advantage of decoupling the pressure field and velocity field, the vorticity dynamics equation along with its relevant derivative formulations have played a pioneering role in this field. Thompson (1883) introduced the concept of

hydrodynamic impulse in terms of moment of vorticity for the expression of total momentum of fluid. Subsequently, similar transformations were widely adopted and further developed into a methodology (Lamb 1932; Batchelor 1967; Lighthill 1986), which is referred to as the derivative-moment transformation or DMT (Wu, et al., 2006). Wu (1981) made substantial progress on the basis of DMT, and generalized the force and moment expressions in terms of the integral of the first and second moments of vorticity for objects in an open incompressible flow. The corresponding relationship with the classical circulation theory of force production is also interpreted under this framework. This spurred a surge of further investigations of the theoretical and numerical aspects of this framework (Noca, et al., 1999; Tan, et al., 2005; Wu, et al., 2006). Although the DMT method has multiple forms for the formulation of force, all of these involve vorticity and its integrated moments and so are unable to explicitly reveal how added-mass effects and viscous dissipation, contribute to force production.

Quartapelle and Napolitano (1983) proposed a novel method for delineating the contribution of various mechanisms on force production; a key element of this formulation was the introduction of a specific harmonic function with appropriate boundary conditions; by projecting the Navier-Stokes equation onto the space of the gradient of this harmonic function, the integrated pressure force on the body could be re-expressed in terms of flow features inside the fluid field and over the body surface. Subsequent studies with similar methods were also carried out by Howe (1995) and Ragazzo et al. (2007). Chang et al. (2008) applied this method in a two-dimensional numerical simulation of flow past multiple circular cylinders and decomposed the drag force into vortex-induced component and surface shear component respectively. Unlike

the vortex dynamic methodology, this approach allows one to express the force and moment experienced by body in terms of flow velocity and related quantities directly to separate out the vorticity related components by decomposing the whole field into a potential part and vorticity part. However, all the previous studies fail to connect the mathematical expression with the physical mechanism such as added mass effect and wing circulation theory.

A more complete methodology for partitioning the forces on a moving, deforming body such as an insect wing such that it would clearly delineate the contributions of vorticity, viscous shear, viscous dissipation and added mass effects could serve as an invaluable tool in the study of insect flight; this is the first objective of the current research.

1.2. Passive Stability of Flapping Wing Flyers

The second major part of this research is the analysis of stability of flight of insects and insect-inspired MAVs in urban environments. To better understand the challenge for MAVs in urban flows, consider the flow associated with a building that has a characteristic size of 10 meters, and a nominal wind speed of 2 m/s. Given a universal Strouhal number of about 0.16 (Roshko, 1954), the Kármán vortex shedding from such a building would occur at a frequency (f_K) of about 0.03 Hz. While this frequency is significantly lower than the typical wing flapping frequency of a MAV (which would be in the 10-100 Hz range), the frequency of vortex rollup in the separated shear layer, which scales as $f_{SL} \sim 0.02\,\mathrm{Re}^{0.67} f_K$ (Prasad and Williamson, 1996), would be about 10 Hz. While f_K and f_{SL} represent lower and upper bounds of the energetic range, non-linear interactions in the flow will, in fact, produce energetic scales at all intermediate

frequencies. The length scales of these perturbations will also range from $O(10m)$ (for the wake) down to a few centimeters for the smallest shear layer eddies. This is schematically shown in Fig. 1-2. Furthermore, given that typical perturbation velocities in a shear layer can be as high as 50% of the freestream velocity (Balachandar et al. 1997), MAVs in an urban environment could experience velocity perturbations of about a meter per second or more.

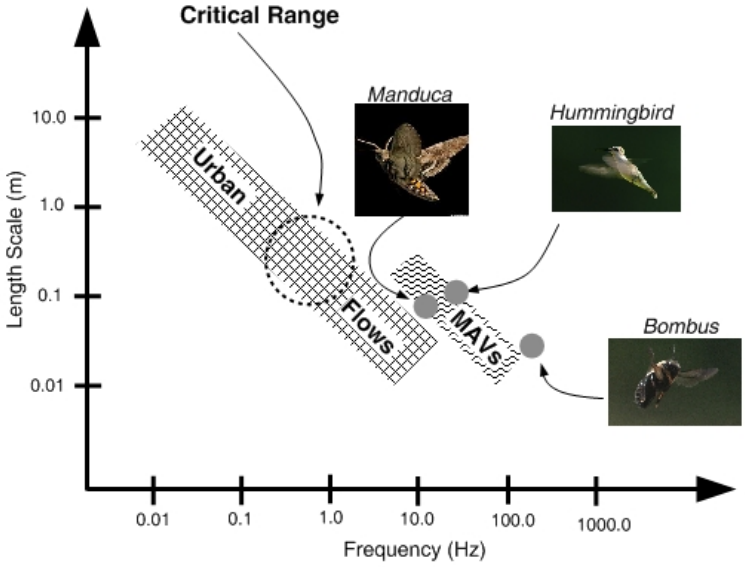

Figure 1-2 Comparison of frequency/length scales of urban flow perturbations with typical flapping wing MAVs and some selected animals.

Of all the aerodynamic perturbations, those with time and length scales which are one to two orders of magnitude larger than the MAV (denoted as the "critical range" in Fig. 1-2) are expected to be most troublesome. On the one hand, these scales are small/rapid enough that they cannot be considered to be in the "quasi-steady" regime for MAVs, and on the other, they are large enough to produce significant perturbation magnitudes. The simple scaling analysis described above clearly shows that such perturbations are indeed

expected to be present in urban flows, and therefore, MAVs will have to be designed to operate (fly, hover, and perhaps, perch and take-off) in the presence of such perturbed flows. Furthermore, negotiating tight exterior as well as interior (inside buildings) flight paths requires a high level of maneuverability. At the same time, MAVs have to be able to stabilize their flight in unsteady environments when required, and also be robust enough to remain operational despite incidental contact with solid objects. These are some of the key challenges for MAV design. It should be noted that atmospheric turbulence also poses somewhat similar challenges for flapping wings MAVs and although the current study was targeted specifically at urban environments, much of what has been learnt here is also relevant to MAV flight in atmospheric turbulence.

Figure 1-3 A hawkmoth experiencing a longitudinal vortex perturbation. In this case the vortex reaches the moth at approximately mid-downstroke and results in a pitch-up perturbation of the moth. Vortices that arrive at mid-upstroke result in pitch-down perturbations of the moth. Experiments have been

conducted by Tyson Hedrick at UNC Chapel Hill.

The ability to hover in a stable manner in complex aerodynamic environments is a distinguishing feature of insects such as moths, flies, wasps and mosquitoes, and birds such as hummingbirds, kingfishers and others. As presented in Fig 1-3, the series of snapshots taken from high speed video of free hovering hawkmoth experiencing vortex gun perturbation show that the hawkmoth is capable of stabilizing its flight in an agile manner even under gusty environment. Interest in understanding this ability is motivated both by organismal biology and designers of micro-aerial vehicles (MAVs).

A variety of methods have been employed in the past to analyze the stability of flying insects. The linear time invariant model has been firstly applied into the longitudinal stability of locust flight by Taylor and Thomas (Taylor and Thomas, 2003). This method assumed that the perturbations are small and therefore amenable to linearized analysis and further assumes that all the related variables can be regarded as time-invariant. A similar methodology has been used in the stability analysis of other insect flyers, such as hawkmoths and droneflies (Wu, et al., 2012). All their conclusions were based on three assumptions:

1. The longitudinal stability is the dominant instability.
2. All the forces and moments can be linearly expanded in 1st order Taylor series;
3. The variation of all involved quantities can be neglected without affecting the stability of insect flyers.

However, the validity of these assumptions cannot be achieved for all insects. Heavy insects such as hawkmoths in particular might not satisfy the time-invariant assumption.

A more accurate alterative methodology is the Floquet theory (Demir, 2000), which allows for a time-periodic (limit cycle) equilibrium state. Wu et al. (2012) used Floquet analysis to examine the stability of droneflies and hawkmoths and showed that the choice of the flapping frequencies for the flyer is crucial for the Floquet analysis to produce results that are matched by the LTI analysis. However, the biggest challenge for Floquet analysis is to determine the correct equilibrium limit cycle, since that can significantly affect the subsequent analysis. In the current work both LTI and Floquet stability analyse are conducted for a hovering hawkmoth. The stability models are based on highly accurate body dynamics models of the insects and include highly realistic models of the deforming, flapping wings. The stability analysis is also used to determine the potential advantage that the flapping wings might have over equivalent revolving wings in terms of flight stability. The analysis is also used to generate insight into the physical process that is responsible for flight instability in a hawkmoth.

1.3. Active Control of Flight Stability in Insects

The ultimate goal of the stability analysis is to explore possible strategies (that involve the sensory motor control system) that could be used by a hawkmoth to stabilize its flight in quiescent as well as perturbed aerodynamic environments. In this regard, the most widely used sensory system in the animal world is the visual system and this is true for flying insect also. Fry et al. (2009) have conducted a series of experiments to investigate the modulation of flight speed via the visual sensory system, and they eventually identified a meaningful high-level control principle by applying genetic algorithms. Straw et al. (2010) found the sensory-motor mechanism of motion control

employed by Drosophila can be identified as an integrated visual feedback approach in the horizontal and vertical planes simultaneously.

In addition to visual sensing, insects also employ mechanosensory mechanisms for flight control. The primary mechanosensors that are known to play a role in insect flight are halteres (Sane et al. 2007) and antennae. Halteres are not present in insects such as hawkmoths and therefore the antennae are the primary mechanosensor in these insects. It has been reported (Sane et al. 2007) that the mediation of rotational velocities in locomotion is accomplished by sensing the Coriolis force exerted on the flagellum of antenna, and this sensory modality could be much faster than the vision-based control (Mamiya, et al., 2011). These ideas are integrated in the current study to propose and test a new strategy for feedback flight control of insects: relative pitching motion between the insect body and flight plane.

CHAPTER 2. COMPUTATIONAL FLUID DYNAMICS METHODOLOGY

In this chapter we describe the salient features of the immersed boundary method (IBM) based solver ViCar3D that forms the backbone of this research. ViCar3D has been developed by the research group of Dr. Rajat Mittal over the last 10+ years. While the development of this solver is not an original contribution of this work, the brief description is included for completeness.

The original contribution to method development of the current research have been: (a) development of a robust coupling scheme between flow and body dynamics, which is described Chapter 6; (b) development of a computer program to execute the force partitioning algorithm that works in concert with ViCar3d, which is described in Chapter 4.

2.1. ViCar3D Immersed Boundary Solver

The governing equations for the aerodynamics of insect flight are the three-dimensional unsteady, viscous incompressible Navier-Stokes equations:

$$\frac{\partial u_i}{\partial x_i} = 0, \quad \frac{\partial u_i}{\partial t} + \frac{\partial u_i u_j}{\partial x_j} = -\frac{1}{\rho}\frac{\partial p}{\partial x_i} + \nu \frac{\partial}{\partial x_j}\left(\frac{\partial u_i}{\partial x_j}\right); \quad i, j = 1, 2, 3 \tag{2-1}$$

where u_i is the flow velocity component corresponding to direction i; p is the flow pressure, and ρ and ν are the fluid density and fluid kinematic viscosity, respectively. In space, the N-S equation above is discretized by a Cartesian grid with cell-centered, collocated arrangement of pressure p and cell-centered flow velocities u_i. In addition, the face-centered velocities, U_i, are also computed separately in purpose of eliminating

checkerboard problem of pressure distribution. In temporal dimension, the equations are integrated in time using the fractional-step method of Van-Kan (Van-Kan, 1986) which consists of three sub-steps. In the first sub-step of this method, a modified momentum equation is solved and an intermediate velocity u^* is obtained. A second-order, Adams–Bashforth scheme is then employed for the convective terms while the diffusion terms are discretized via an implicit Crank–Nicolson scheme to eliminate the viscous stability constraint. In this sub-step, the following modified momentum equation is solved at the cell-nodes,

$$\frac{u_i^* - u_i^n}{\Delta t} + \frac{1}{2}\left(3N_i^n - N_i^{n-1}\right) = -\frac{1}{\rho}\frac{\delta p^n}{\delta x_i} + \frac{1}{2}\left(D_i^* + D_i^n\right) \tag{2-2}$$

where $N_i = \dfrac{\partial\left(U_j u_i\right)}{\partial x_j}$ is the convective term and $D_i = \nu\left(\dfrac{\delta}{\delta x_j}\right)\left(\dfrac{\delta u_i}{\delta x_j}\right)$ is diffusive terms, and $\dfrac{\delta}{\delta x}$ denotes the second-order central difference. Thereby the discretized equation can be solved using a line-SOR scheme (Anderson et al., 1984). As shown in Fig. 2-1, the face-center velocities at this intermediate step U_i are computed by averaging the adjacent nodes values in the orthogonal directions. Similar to a fully staggered arrangement, only the face velocity component normal to the cell-face is calculated and used for computing the volume flux from each cell. The averaging procedure is followed as,

$$\tilde{u}_i = u_i^* + \Delta t \frac{1}{\rho}\left(\frac{\delta p^n}{\delta x_i}\right)_{cc} \tag{2-3}$$

$$\tilde{U}_1 = \gamma_w \tilde{u}_{1P} + (1-\gamma_w)\tilde{u}_{1W} \tag{2-4}$$

$$\tilde{U}_2 = \gamma_s \tilde{u}_{2P} + (1-\gamma_s)\tilde{u}_{2S} \tag{2-5}$$

$$\tilde{U}_3 = \gamma_b \tilde{u}_{3P} + (1-\gamma_b)\tilde{u}_{3B} \tag{2-6}$$

$$U_i^* = \tilde{U}_i - \Delta t \frac{1}{\rho}\left(\frac{\delta p^n}{\delta x_i}\right)_{fc} \tag{2-7}$$

where γ_w, γ_s and γ_b are the weights corresponding to linear interpolation for the west, south and back face velocity components respectively. Moreover, subscripts "cc" and "fc" denote gradients of corresponding quantities computed at cell-centers and face-centers, respectively.

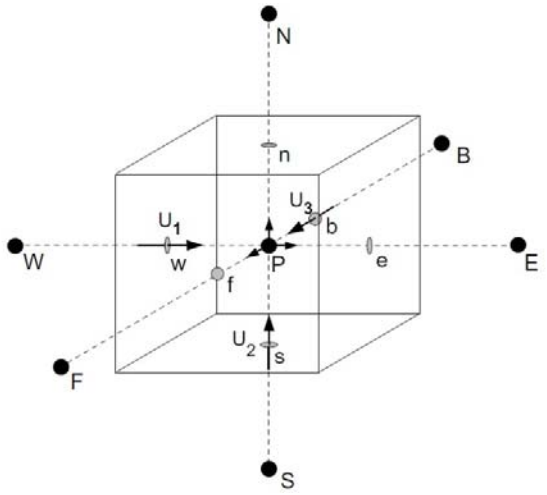

Figure 2-1 Schematic describing the naming convention and location of velocity components employed in the spatial discretization of the governing equation (From Mittal et al. (2008)).

The second sub-step requires the solution of the pressure correction equation,

$$\frac{u_i^{n+1} - u_i^*}{\Delta t} = -\frac{1}{\rho}\frac{\delta p'}{\delta x_i} \tag{2-8}$$

which is solved to satisfy that the final velocity u_i^{n+1} should be divergence-free discretely. The above equation together with the divergence free condition leads to the following Poisson equation for the pressure correction,

$$\frac{1}{\rho}\frac{\delta}{\delta x_i}\left(\frac{\delta p'}{\delta x_i}\right) = \frac{1}{\Delta t}\frac{\delta U_i^*}{\delta x_i} \tag{2-9}$$

along with the Neumann boundary condition imposed on this pressure correction at all boundaries.

This Poisson equation is solved with a highly efficient geometric multi-grid method (Mittal et al. 2008) with a Gauss–Siedel line-SOR smoother (Press et al., 1992). The ability to employ such methods is another key advantage of the current Cartesian grid approach over body-conformal unstructured grid approaches. Compared with conventional body-fitting approaches, geometrical multi-grid methods are relatively simple to implement and have very limited memory overhead. Furthermore, when coupled with powerful smoothers like line-Gauss–Siedel, they can lead to a numerical solution to the pressure Poisson equation which scales almost linearly with the number of grid points. In contrast, for unstructured body-conformal methods, one has to either resort to algebraic multi-grid methods (Stuben 2001) or other more complex methods such as agglomeration multi-grid (Mavriplis and Venkatakrishnan, 1994).

Once the pressure correction is obtained, the pressure and velocity are updated as,

$$p^{n+1} = p^n + p' \tag{2-10}$$

$$u_i^{n+1} = u_i^* - \Delta t \frac{1}{\rho}\left(\frac{\delta p'}{\delta x_i}\right)_{cc} \tag{2-11}$$

$$U_i^{n+1} = U_i^* - \Delta t \frac{1}{\rho}\left(\frac{\delta p'}{\delta x_i}\right)_{fc} \tag{2-12}$$

These separately updated face-velocities satisfy discrete mass-conservation to machine accuracy and use of these velocities in estimating the non-linear convective flux in Eq. (2-2) enforces geometric conservation for the convective flux. The methodology of calculating face-center velocities and node-center velocities separately was firstly proposed by Zang et al. (Zang et al., 1994) and then applied to the Cartesian grid in Ye et al. (Ye et al, 1999). The above collocated scheme is simpler to implement than a

conventional staggered mesh scheme (Zang et al., 1994) and especially when coupled with a central-difference spatial scheme, it performs with good discrete kinetic energy conservation properties (Felten and Lund, 2000).

2.2. Immersed Boundary Treatment

The current immersed boundary method employs a multi-dimensional ghost-cell methodology to impose the boundary conditions on the immersed boundary, which can be either stationary or moving. Firstly, the surface of the internal body is discretized by a mesh with triangular elements and then numerically "immersed" in the Cartesian grid as shown in Fig. 2-2. A ghost-cell is defined as cell located inside the solid that is adjacent to least one fluid cell. Since the cells in all categories are straightforward to distinguish numerically, the major challenge left is to find out the appropriate condition involving ghost-cells, which can enable us to implement the specified boundary condition. This is done by detecting the image-point (IP) of all the ghost-cells in the fluid, and the body intercept (BI) that lies on the boundary, midway between center of ghost-cell and the IP .

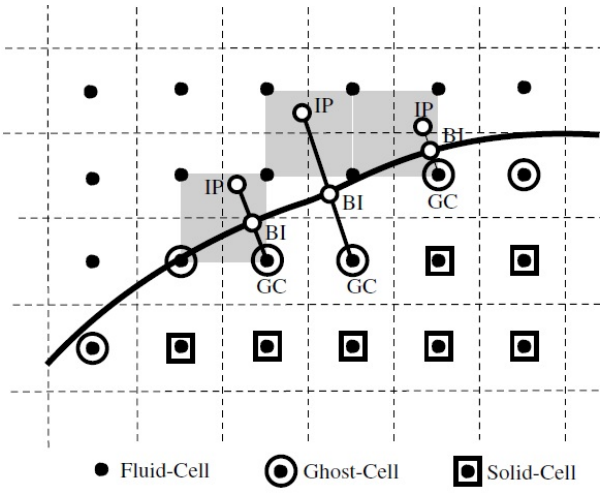

Figure 2-2 Schematic of two-dimensional spatial discretization and immersed boundary detection (From Mittal et al. (2008)).

Even though the identifications of "IP" and "BI" can be conceptually simple, the implementation to exactly locate them involves very complicated procedures especially for complex 3D immersed bodies. This is critical because if the incorrect detection is implemented, it leads to the wrong boundary conditions to be imposed and may result in a catastrophic instability. To guarantee that the BI is correctly determined, we first determine the closest element vertex on the surface to the corresponding ghost-cell and then search for the normal intercept among those surface elements which share the closest vertex. The same procedures should be repeated several times in order to examine the whole sub-set of possible elements.

Once the "BI" and "IP" for every ghost-cell are obtained, a tri-linear interpolation in three-dimensions (or bilinear in two-dimensions interpolation) is used to compute the value of all related quantities at IP in terms of the eight surrounding cells adjacent to it,

$$\phi(x_1, x_2, x_3) = C_1 x_1 x_2 x_3 + C_2 x_1 x_2 + C_3 x_2 x_3 + C_4 x_1 x_3 + C_5 x_1 + C_6 x_2 + C_7 x_3 + C_8 \quad (2\text{-}13)$$

where ϕ is the genetic variable at IP and expressed as the function of spatial coordinates; $\{C\}^T = \{C_1, C_2, C_3, \ldots, C_8\}$ are the unknown coefficients and can be calculated by solving the inverse problem,

$$\{C\} = [V]^{-1} \{\phi\} \quad (2\text{-}14)$$

where $[V]$ is the Vandermonde matrix corresponding to the tri-linear interpolation,

$$[V]=\begin{bmatrix} x_1x_2x_3|_1 & x_1x_2|_1 & x_2x_3|_1 & x_1x_3|_1 & x_1|_1 & x_2|_1 & x_3|_1 & 1 \\ x_1x_2x_3|_2 & x_1x_2|_2 & x_2x_3|_2 & x_1x_3|_2 & x_1|_2 & x_2|_2 & x_3|_2 & 1 \\ x_1x_2x_3|_3 & x_1x_2|_3 & x_2x_3|_3 & x_1x_3|_3 & x_1|_3 & x_2|_3 & x_3|_3 & 1 \\ \cdot & \cdot & \cdot & \cdot & \cdot & \cdot & \cdot & \cdot \\ \cdot & \cdot & \cdot & \cdot & \cdot & \cdot & \cdot & \cdot \\ \cdot & \cdot & \cdot & \cdot & \cdot & \cdot & \cdot & \cdot \\ x_1x_2x_3|_8 & x_1x_2|_8 & x_2x_3|_8 & x_1x_3|_8 & x_1|_8 & x_2|_8 & x_3|_8 & 1 \end{bmatrix} \tag{2-15}$$

where the subscripts $\{1,2,3,\ldots,8\}$ denote the index of surrounding cells. Thereby the value of quantities at the IP can be calculated as,

$$\phi_{IP}=\sum\beta_i\phi_i \tag{2-16}$$

where ϕ_i are the values of local neighboring nodes around IP and β_i are the corresponding weights that merely depends on the coordinates.

Using a central-difference approximation along the normal probe to the immersed boundary, we can implement the Dirichlet and Neumann boundary conditions via using the following scheme,

$$\phi_{GC}=2\phi_{BI}-\phi_{IP} \tag{2-17}$$

$$\phi_{GC}=\Delta l_p\left(\frac{\delta\phi}{\delta n}\right)_{BI}\phi_{BI}+\phi_{IP} \tag{2-18}$$

where Δl_p is the length of ghost-cell to the image point. By substituting Eq. (2-16) into (2-17) and (2-18) respectively, we can obtain,

$$\phi_{GC}+\sum\beta_i\phi_i=2\phi_{BI} \tag{2-19}$$

$$\phi_{GC}-\sum\beta_i\phi_i=\Delta l_p\left(\frac{\delta\phi}{\delta n}\right)_{BI}\phi_{BI} \tag{2-20}$$

In order to obtain the pressure and velocities, Eq. (2-2) and (2-9) are solved together with Eq. (2-19) or (2-20) in a fully coupled manner. This procedure ensures the second-order spatial and temporal accuracy.

Further details about ViCar3D can be found in Mittal et al. (2008) and Zheng (2013).

CHAPTER 3. FORCE PARTITIONING THEORY: DERIVATION AND ASSESSMENT

3.1. Introduction

The partitioning of the forces experienced by a body immersed in a fluid into components that can be attributed to various physical mechanisms and flow features has been a recurrent theme in fluid dynamics, and a variety of formulations have been developed that attempt to accomplish this. Among these, the derivative-moment transformation by Wu (Wu, 1981; Wu, et al, 2006) and the force projection methods by Quarterpelle and Napolitano (1983) and Howe (1995) are particularly worth mentioning here. In the current work, we follow the force decomposition approach of Quarterpelle and Napolitano (Quarterpelle, et al, 1983) but extend it in two ways: first by employing the Helmholtz velocity decomposition, we provide a clearer separation of the vortical components of force from the other components, and also separate the added-mass force into its translational and centripetal components. Second, while Quarterpelle and Napolitano (1983) limited the application of their formulation to canonical Stokes and inviscid flows with exact solutions, we implement our force partitioning method (FPM) into a general flow solver that enables the force partitioning to be applied to flows at finite Reynolds numbers with complex moving boundaries. The result is a powerful flow analysis tool that can be used to gain insights into the mechanisms of force production in a wide class of problems.

3.2. Derivation

3.2.1. Traditional Method of Force Calculation

Consider an object (here we consider a hovering hawkmoth) immersed in a domain of incompressible fluid with volume V_f bounded by the surface Σ as shown in Fig. 3-1. The net force on the immersed body is given by

$$\vec{F}_B = \int_B \left(p\hat{n} + \vec{\tau}_w \right) dS \tag{3-1}$$

where B is the surface of the body, $\hat{n}$ the unit normal vector of the surface pointing from inside to outside of the volume, and p and τ_w are the pressure and surface shear, respectively.

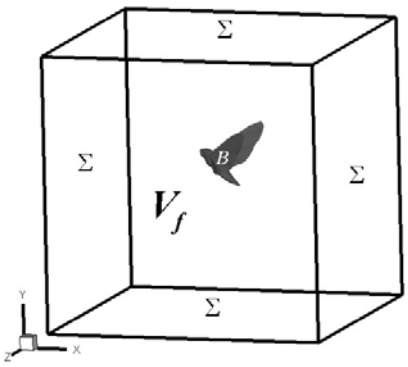

Figure 3-1 Schematics of control volume and internal body

A CFD simulation, usually provides full access to all the quantities in the above equation not only on the body surface but also in the the entire flow domain. Therefore Eq. (3-1) is usually employed as a traditional approach associated with CFD methodology to calculate forces. However, the above description of the force on the body

is insufficient to distinguish the partial contributions of the different mechanisms to the pressure on the surface. Doing so is non-trivial since pressure in an incompressible flow is governed by an elliptic equation and is therefore coupled to the flow velocity at every point in the flow field.

3.2.2. Force Partitioning Method (FPM)

Here we construct a formulation of the total force exerted by an incompressible Newtonian flow on an immersed body and delineate clearly the partial contributions of various physical mechanisms and features to the total aerodynamic force. The formulation is based on the force projection methodology presented by Quarterpelle, et al (1983), but we extend this formulation and implement it into a three-dimensional, sharp-interface immersed boundary Navier-Stokes solver (Mittal, et al, 2008).

The starting point for the method is the incompressible Navier-Stokes equation in the Lamb-Gromeka form (3-3) which is written as follows:

$$\rho\frac{\partial\vec{u}}{\partial t}+\rho\vec{\omega}\times\vec{u}+\frac{1}{2}\rho\vec{\nabla}\left(\vec{u}\cdot\vec{u}\right)=-\vec{\nabla}p-\mu\vec{\nabla}\times\vec{\omega} \tag{3-3}$$

where ρ and μ are the fluid density and absolute viscosity, and $\vec{u}$, p and $\vec{\omega}$ are the flow velocity, pressure and vorticity respectively. The boundary conditions for the above equations are

$$\vec{u}\left(\vec{x},t\right)=\begin{cases}\vec{U}\left(\vec{x},t\right), & on\ B\left(t\right)\\ \vec{V}_{\infty}+\vec{v}'\left(\vec{x},t\right), & on\ \sum\end{cases} \tag{3-4}$$

that correspond to the flapping flight of an animal in a freestream with velocity equal to $\vec{V}_{\infty}$. Also as in the schematic Fig 1, $B\left(t\right)$ represents the time-dependent surface of the

wing (and body), which may be moving and/or deforming, and $\vec{U}(t)$ is the velocity of this surface. Furthermore, $\sum$ represents the outer surface of the large, but finite domain (with volume denoted by V_f) and $\vec{v}'$ represents the perturbation to the free-stream on the outer boundary due to the immersed object. It is understood that for a large domain, $\vec{v}'$ would be much smaller than $\vec{U}$. Our study here addresses a typical case of hovering flight in quiescent flow with $\vec{V}_\infty \equiv 0$.

A harmonic function $\phi^{(i)}$ for $i = 1,2,3$ is now introduced, which satisfies at any time-instance $t = \tau$, the following equation:

$$\nabla^2 \phi^{(i)} = 0 \ with \ \vec{n} \cdot \vec{\nabla} \phi^{(i)} = \begin{cases} \vec{n} \cdot \vec{\nabla} x_i = n_i, & on \ B(\tau) \\ 0, & on \ \Sigma \end{cases} \tag{3-5}$$

Here $\phi^{(i)}$ for $i = 1,2,3$ can be obtained by solving Eq. (3-5) individually for each of the three components corresponding to three coordinates.

In order to completely separate the roles of potential flow (added mass effect) and vortex dynamics on the force production, we employ the Helmholtz cecomposition (Eq. (3-6)) to decompose the velocity field into potential part and rotational part (vorticity).

$$\vec{u} = \vec{u}_\Phi + \vec{u}_v = \vec{\nabla}\Phi + \vec{\nabla} \times \vec{A} \tag{3-6}$$

where $\vec{u}_\Phi$ is the potential flow velocity and $\vec{u}_v$ is the vorticity induced velocity, Φ and $\vec{A}$ are the corresponding scalar and vector. Therefore the Navier-Stokes equation can be also separated into potential flow momentum equation and vorticity flow momentum equation,

$$\rho \frac{\partial \vec{u}_\Phi}{\partial t} + \frac{1}{2} \rho \vec{\nabla} \left(\vec{u}_\Phi \cdot \vec{u}_\Phi \right) = -\vec{\nabla} p_\Phi \tag{3-7a}$$

$$\rho \frac{\partial \vec{u}_v}{\partial t} + \rho \vec{\omega} \times \vec{u} + \frac{1}{2} \rho \vec{\nabla} \left(2\vec{u}_v \cdot \vec{u}_\Phi + \vec{u}_v \cdot \vec{u}_v \right) = -\vec{\nabla} p_v - \mu \vec{\nabla} \times \vec{\omega} \tag{3-7b}$$

$$p = p_\Phi + p_v \tag{3-7c}$$

where p_Φ and p_v are pressure in potential flow and vorticity flow respectively.

The boundary conditions for the two equations above require careful consideration. If the velocity of the wing surface $\vec{U}$ can be decomposed into $\vec{U} = U_n\hat{n} + U_t\hat{t}$ where $U_n\hat{n}$ and $U_t\hat{t}$ are the components normal and tangential to the surface respectively, then the boundary condition $\vec{U}_\Phi \cdot \hat{n} = U_n$ on the wing surface ensures that $\vec{u}_\Phi$ is precisely the potential flow associated with this configuration and Eq. (3-7a) with this boundary conditions is the well-known Euler equation. The solution of the potential flow equations however, produces a slip velocity on the surface and total potential flow velocity on the surface therefore is $\vec{U}_\Phi = U_n\hat{n} + U_{\Phi_t}\hat{t}$ where U_{Φ_t} is the potential slip velocity. For condition Eq. (3-6) to hold, the surface boundary condition for the vortical component is $\vec{U}_v = \left(U_t - U_{\Phi_t}\right)\hat{t}$. Thus, the velocity of the surface of the internal body B can also be written as $\vec{U} = \vec{U}_\Phi + \vec{U}_v$, where we identify $\vec{U}_\Phi$ as the potential flow velocity on the surface and $\vec{U}_v$ the tangential component of surface velocity associated with the vortical component of the flow.

To express the force production in potential flow, Eqn. (3-7a) is projected onto the gradient of $\phi^{(i)}$ for a given $\phi^{(i)}$ as in Eq. (3-5), and the resulting equation is integrated over the domain volume V_f as follows:

$$\rho\int_{V_f}\frac{\partial\vec{u}_\Phi}{\partial t}\cdot\vec{\nabla}\phi^{(i)}dV + \frac{1}{2}\rho\int_{V_f}\vec{\nabla}\left(\vec{u}_\Phi\cdot\vec{u}_\Phi\right)\cdot\vec{\nabla}\phi^{(i)}dV = -\int_{V_f}\vec{\nabla}p_\Phi\cdot\vec{\nabla}\phi^{(i)}dV$$

$$\rho\int_{V_f}\frac{\partial\vec{u}_\Phi}{\partial t}\cdot\vec{\nabla}\phi^{(i)}dV + \frac{1}{2}\rho\int_{V_f}\vec{\nabla}\cdot\left(u_\Phi^2\vec{\nabla}\phi^{(i)}\right)dV = -\int_{V_f}\vec{\nabla}\cdot\left(p_\Phi\vec{\nabla}\phi^{(i)}\right)dV$$

$$\rho\int_{V_f}\frac{\partial\vec{u}_\Phi}{\partial t}\cdot\vec{\nabla}\phi^{(i)}dV+\frac{1}{2}\rho\int_{B+\Sigma}u_\Phi^2\vec{n}\cdot\vec{\nabla}\phi^{(i)}dV=-\int_{B+\Sigma}p_\Phi\vec{n}\cdot\vec{\nabla}\phi^{(i)}dS$$

$$\rho\int_{V_f}\frac{\partial\vec{u}_\Phi}{\partial t}\cdot\vec{\nabla}\phi^{(i)}dV+\frac{1}{2}\rho\int_{B}u_\Phi^2 n_i dV=-\int_{B}p_\Phi n_i dS$$

$$\rho\int_{V_f}\frac{\partial\vec{u}_\Phi}{\partial t}\cdot\vec{\nabla}\phi^{(i)}dV+\frac{1}{2}\rho\int_{B}u_\Phi^2 n_i dV=-\int_{B}p_\Phi n_i dS$$

So that the total force contributed by potential flow can be expressed as,

$$F_{PF}^i=\int_B p_\Phi n_i dS=-\rho\int_{V_f}\frac{\partial\vec{u}_\Phi}{\partial t}\cdot\vec{\nabla}\phi^{(i)}dV-\frac{1}{2}\rho\int_B u_\Phi^2 n_i dV$$

The unsteady term can be also further segregated in the following way,

$$\begin{aligned}\rho\int_{V_f}\frac{\partial\vec{u}_\Phi}{\partial t}\cdot\vec{\nabla}\phi^{(i)}dV&=\rho\int_{V_f}\vec{\nabla}\cdot\left(\frac{\partial\vec{u}_\Phi}{\partial t}\phi^{(i)}\right)dV\\&=\rho\int_{B+\Sigma}\vec{n}\cdot\frac{\partial\vec{U}_\Phi}{\partial t}\phi^{(i)}dS\\&=\rho\int_{B+\Sigma}\vec{n}\cdot\frac{d\vec{U}_\Phi}{dt}\phi^{(i)}dS-\rho\int_{B+\Sigma}\vec{n}\cdot\vec{\nabla}\left(\frac{1}{2}U_\Phi^2\right)\phi^{(i)}dS\\&=\rho\int_{B+\Sigma}\vec{n}\cdot\frac{d\vec{U}_\Phi}{dt}\phi^{(i)}dS-\rho\int_{V_f}\vec{\nabla}\cdot\left(\vec{\nabla}\left(\frac{1}{2}u_\Phi^2\right)\phi^{(i)}\right)dV\end{aligned}$$

Thus the formula for the total force induced by potential flow is obtained as,

$$F_{PF}^i=-\rho\int_{B+\Sigma}\vec{n}\cdot\frac{d\vec{U}_\Phi}{dt}\phi^{(i)}dS-\frac{1}{2}\rho\int_B U_\Phi^2 n_i dS+\rho\int_{V_f}\vec{\nabla}\cdot\left(\vec{\nabla}\left(\frac{1}{2}u_\Phi^2\right)\phi^{(i)}\right)dV \qquad (3\text{-}8)$$

where $\vec{U}_\phi$ is the surface velocity component induced by potential flow. We should note that according to D'Alembert's paradox, the only force generated by potential flow is the added mass force due to acceleration of body. Therefore, the above formula is also the expression of added mass force in potential flow.

A similar projection and segregation can be applied to Eq. (3-7b) and utilizing the same procedures, we can express the force purely generated by the viscous/vertical component of the flow as follows:

$$\rho\int_{V_f}\frac{\partial\vec{u}_v}{\partial t}\cdot\vec{\nabla}\phi^{(i)}dV+\rho\int_{V_f}(\vec{\omega}\times\vec{u})\cdot\vec{\nabla}\phi^{(i)}dV+\frac{1}{2}\rho\int_{V_f}\vec{\nabla}\left(2\vec{u}_v\cdot\vec{u}_\Phi+\vec{u}_v\cdot\vec{u}_v\right)\cdot\vec{\nabla}\phi^{(i)}dV$$
$$=-\int_{V_f}\vec{\nabla}p_v\cdot\vec{\nabla}\phi^{(i)}dV-\mu\int_{V_f}\left(\vec{\nabla}\times\vec{\omega}\right)\cdot\vec{\nabla}\phi^{(i)}dV$$

Due to $\left(\vec{\nabla}\times\vec{\omega}\right)\cdot\vec{\nabla}\phi^{(i)}=\vec{\nabla}\cdot\left(\vec{\omega}\times\vec{\nabla}\phi^{(i)}\right)$, it can be further derived,

$$\rho\int_{V_f}\frac{\partial\vec{u}_v}{\partial t}\cdot\vec{\nabla}\phi^{(i)}dV+\rho\int_{V_f}(\vec{\omega}\times\vec{u})\cdot\vec{\nabla}\phi^{(i)}dV+\frac{1}{2}\rho\int_{B}\left(2\vec{u}_v\cdot\vec{u}_\Phi+\vec{u}_v\cdot\vec{u}_v\right)n_i dS$$
$$=-\int_{B}p_v n_i dS-\mu\int_{B+\Sigma}\vec{n}\cdot\left(\vec{\omega}\times\vec{\nabla}\phi^{(i)}\right)dS$$

$$\rho\int_{V_f}\frac{\partial\vec{u}_v}{\partial t}\cdot\vec{\nabla}\phi^{(i)}dV+\rho\int_{V_f}(\vec{\omega}\times\vec{u})\cdot\vec{\nabla}\phi^{(i)}dV+\frac{1}{2}\rho\int_{B}\left(2\vec{u}_v\cdot\vec{u}_\Phi+\vec{u}_v\cdot\vec{u}_v\right)n_i dS$$
$$=-\int_{B}p_v n_i dS+\mu\int_{B+\Sigma}(\vec{\omega}\times\vec{n})\cdot\vec{\nabla}\phi^{(i)}dS$$

$$\rho\int_{V_f}\vec{\nabla}\cdot\left(\frac{\partial\vec{u}_v}{\partial t}\phi^{(i)}\right)dV+\rho\int_{V_f}(\vec{\omega}\times\vec{u})\cdot\vec{\nabla}\phi^{(i)}dV+\frac{1}{2}\rho\int_{B}\left(2\vec{u}_v\cdot\vec{u}_\Phi+\vec{u}_v\cdot\vec{u}_v\right)n_i dS$$
$$=-\int_{B}p_v n_i dS+\mu\int_{B+\Sigma}(\vec{\omega}\times\vec{n})\cdot\vec{\nabla}\phi^{(i)}dS$$

$$\rho\int_{B+\Sigma}\vec{n}\cdot\left(\frac{\partial\vec{U}_v}{\partial t}\phi^{(i)}\right)dS+\rho\int_{V_f}(\vec{\omega}\times\vec{u})\cdot\vec{\nabla}\phi^{(i)}dV+\frac{1}{2}\rho\int_{B}\left(2\vec{u}_v\cdot\vec{u}_\Phi+\vec{u}_v\cdot\vec{u}_v\right)n_i dS$$
$$=-\int_{B}p_v n_i dS+\mu\int_{B+\Sigma}(\vec{\omega}\times\vec{n})\cdot\vec{\nabla}\phi^{(i)}dS$$

$$\rho\int_{B+\Sigma}\vec{n}\cdot\left(\frac{d\vec{U}_v}{dt}\phi^{(i)}\right)dS-\rho\int_{V_f}\vec{\nabla}\cdot\left(\left(\vec{\omega}\times\vec{u}+\frac{1}{2}\rho\vec{\nabla}\left(2\vec{u}_v\cdot\vec{u}_\Phi+\vec{u}_v\cdot\vec{u}_v\right)\right)\phi^{(i)}\right)dV$$
$$+\rho\int_{V_f}(\vec{\omega}\times\vec{u})\cdot\vec{\nabla}\phi^{(i)}dV+\rho\int_{B}\left(\vec{U}_v\cdot\vec{U}_\Phi+\frac{1}{2}\vec{U}_v\cdot\vec{U}_v\right)n_i dS=-\int_{B}p_v n_i dS+\mu\int_{B+\Sigma}(\vec{\omega}\times\vec{n})\cdot\vec{\nabla}\phi^{(i)}dS$$

$$\rho \int_{B+\Sigma} \vec{n} \cdot \left(\frac{d\vec{U}_v}{dt} \phi^{(i)} \right) dS - \frac{1}{2} \rho \int_{V_f} \vec{\nabla} \cdot \left(\vec{\nabla} \left(2\vec{u}_v \cdot \vec{u}_\Phi + \vec{u}_v \cdot \vec{u}_v \right) \phi^{(i)} \right) dV - \rho \int_{V_f} \vec{\nabla} \cdot \left(\vec{\omega} \times \vec{u} \right) \phi^{(i)} dV$$
$$+ \rho \int_B \left(\vec{U}_v \cdot \vec{U}_\Phi + \frac{1}{2} \vec{U}_v \cdot \vec{U}_v \right) n_i dS = - \int_B p_v n_i dS + \mu \int_{B+\Sigma} \left(\vec{\omega} \times \vec{n} \right) \cdot \vec{\nabla} \phi^{(i)} dS$$

Finally,

$$\begin{aligned} F_{VF}^i = & -\rho \int_{B+\Sigma} \vec{n} \cdot \left(\frac{d\vec{U}_v}{dt} \phi^{(i)} \right) dS + \frac{1}{2} \rho \int_{V_f} \vec{\nabla} \cdot \left(\vec{\nabla} \left(2\vec{u}_v \cdot \vec{u}_\Phi + \vec{u}_v \cdot \vec{u}_v \right) \phi^{(i)} \right) dV \\ & + \rho \int_{V_f} \left[\vec{\nabla} \cdot \left(\vec{\omega} \times \vec{u} \right) \right] \phi^{(i)} dV - \rho \int_B \left(\vec{U}_v \cdot \vec{U}_\Phi + \frac{1}{2} \vec{U}_v \cdot \vec{U}_v \right) n_i dS \\ & + \mu \int_B \left(\vec{\omega} \times \vec{n} \right) \cdot \vec{\nabla} \left(\phi^{(i)} - x_i \right) dS + \mu \int_\Sigma \left(\vec{\omega} \times \vec{n} \right) \cdot \vec{\nabla} \phi^{(i)} dS \end{aligned} \tag{3-9}$$

Similar to the potential component of the surface velocity $\vec{U}_\Phi$, here $\vec{U}_v$ represents the component of the surface velocity associated with the viscous rotational component describe by Eq. 3-7b.

Given the force formulation in potential flow regime and vorticity flow regime, we can easily assemble both to get the total force formulation in the real incompressible viscous flow just as the way we decompose it. Eventually, the final version of FPM is expressed in the following equations,

$$F_B^i = F_\kappa^i + F_\omega^i + F_\sigma^i + F_\phi^i + F_\Sigma^i \tag{3-10a}$$

$$F_\kappa^i = -\rho \int_B \vec{n} \cdot \frac{d\vec{U}}{dt} \phi^{(i)} dS - \frac{1}{2} \rho \int_B U^2 n_i dS \tag{3-10b}$$

$$F_\omega^i = \rho \int_{V_f} \vec{\nabla} \cdot \left[\vec{\nabla} \left(\vec{u}_v \cdot \vec{u}_\Phi + \frac{1}{2} \vec{u}_v \cdot \vec{u}_v \right) \phi^{(i)} \right] dV + \rho \int_{V_f} \left[\vec{\nabla} \cdot \left(\vec{\omega} \times \vec{u} \right) \right] \phi^{(i)} dV \tag{3-10c}$$

$$F_\sigma^i = \mu \int_B \left(\vec{\omega} \times \vec{n} \right) \cdot \vec{\nabla} \left(\phi^{(i)} - x_i \right) dS \tag{3-10d}$$

$$F_{\phi}^{i} = \rho \int_{B} \vec{n} \cdot \left(\vec{\nabla} \left(\frac{1}{2} u_{\Phi}^{2} \right) \phi^{(i)} \right) dS \tag{3-10f}$$

$$F_{\Sigma}^{i} = -\rho \int_{\Sigma} \vec{n} \cdot \frac{d\vec{v}'}{dt} \phi^{(i)} dS + \rho \int_{\Sigma} \vec{n} \cdot \left(\vec{\nabla} \left(\frac{1}{2} u_{\Phi}^{2} \right) \phi^{(i)} \right) dS + \mu \int_{\Sigma} \left(\vec{\omega} \times \vec{n} \right) \cdot \vec{\nabla} \phi^{(i)} dS \tag{3-10g}$$

In the above, the total force is decomposed into four components according to different physical mechanisms. Here F_{κ}^{i} is a novel conception of a force component, which we term the "total added mass force", because it is determined solely by the kinematics (shape, velocity and acceleration) of the body; F_{ω}^{i} is the vortex induced force totally related to vorticity flow regime; The component F_{σ}^{i} is identified as the force due to viscosity on the body; F_{ϕ}^{i} is the force component merely associated with potential flow; The last component F_{Σ}^{i} is the force contribution by the flow and viscous shear on the outer boundary of the domain.

3.2.3. Discretization Schemes

In order to apply the force partitioning method to the cases being simulated by ViCar3D, we have developed a method, which is based on the well-developed multi-dimensional ghost-cell immersed boundary method, to solve the harmonic function $\phi^{(i)}, i = 1, 2, 3$ for any immersed body that can be addresses by ViCar3D. The key elements of this module are a subroutine for solving the Laplace equation for the harmonic function with a Neumann boundary condition (Eq. 3-5) and the estimation of various derivative terms in FPM terms.

The Laplace equation for the harmonic function is solved via a modified version of the Poisson solver that is used for solving for pressure inside ViCar3D. Similarly, all the

other derivative terms in FPM are evaluated using a second-order central difference scheme and values near the immersed boundary use the very same ghost-cell methodology that is used inside ViCar3D.

3.3. Discussion and Physical Interpretation of Terms in FPM

In this section, we will further discuss the partitioned force components and provide a physical perspective on these components.

3.3.1. The Harmonic Function

Before going further into the physical interpretation of the different force components, we interpret the harmonic function $\phi^{(i)}$ in terms of its mathematical properties and physical meaning because it is explicitly involved in almost every term in the FPM Eq. (3-10). According to the mathematical prescription in Eq. (3-5), $\phi^{(i)}$ can be identified as the instantaneous potential function associated with the inviscid, irrotational flow past the given body with non-deforming shape corresponding to $t=\tau$, translating in the x_i direction with constant unit velocity.

In this context, we may recognize that the harmonic function $\phi^{(i)}$ will decay as the distance from the internal body increases. The rate of decay of $\phi^{(i)}$ in terms of distance from the body r, it can be derived using fundamental vector theory as follows

$$\begin{aligned}\int_{V_f} \vec{\nabla}\phi^{(i)} dV &= -\int_{V_f} \vec{x}\nabla^2\phi^{(i)} dV + \int_{B+\Sigma} \vec{x}\left(\vec{\nabla}\phi^{(i)}\cdot\vec{n}\right) dS \\ &= 0 + \int_{B} \vec{x}\left(\vec{e}_i\cdot\vec{n}\right) dS \\ &= \int_{V_B} \vec{e}_i dV = V_B\vec{e}_i\end{aligned} \tag{3-11}$$

where $\vec{x}$ is the coordinates vector, $\vec{e}_i$ is the unit vector pointing in the i direction and V_B is the volume of the immersed body. And it is straightforward that,

$$\left|\vec{\nabla}\phi^{(i)}\right| \sim O\left(\frac{V_B}{r^d}\right) \text{ and } \phi^{(i)} \sim O\left(\frac{V_B}{r^{d-1}}\right) \tag{3-12}$$

where $d = 2,3$ is the dimension.

3.3.2. Total Added Mass Force

As clearly manifested in Eq. (3-10b), the only decisive factors for the total added mass force are the local acceleration of the body and the harmonic function $\phi^{(i)}$, both of which are solely dependent on the instantaneous body kinematics. Therefore, if given the body kinematics, we can simply calculate the total added mass force component by solving the Laplace equation for $\phi^{(i)}$ instead of expensively solving the Navier-Stokes Equation.

For simplicity, if we only consider the non-deforming objects in the flow, the surface velocity can be expressed as the sum of translational velocity and rotational velocity as in Eq. (3-13).

$$\vec{U}\left(\vec{x}\right) = \vec{U}_C + \vec{\Omega} \times \left(\vec{x} - \vec{x}_C\right) \tag{3-13}$$

We now substitute Eq. (3-13) into the term $\frac{\rho}{2}\int_B U^2 n_i dS$ in Eq. (3-10bas follows

$$
\begin{aligned}
\frac{\rho}{2}\int_B U^2 n_i dS &= \frac{\rho}{2}\int_B \left(\vec{U}_C + \vec{\Omega}\times\left(\vec{x}-\vec{x}_C\right)\right)^2 n_i dS \\
&= \frac{\rho}{2}\left[\int_B U_C^2 n_i dS + \int_B \left(\vec{\Omega}\times\left(\vec{x}-\vec{x}_C\right)\right)^2 n_i dS + 2\int_B \vec{U}_C\cdot\left(\vec{\Omega}\times\vec{x}\right) n_i dS\right] \\
&= \frac{\rho}{2}\left[U_C^2\int_B n_i dS + \int_B \left(\vec{\Omega}\times\left(\vec{x}-\vec{x}_C\right)\right)^2 n_i dS + 2\left(\vec{U}_C\times\vec{\Omega}\right)\cdot\int_B \vec{x}\vec{e}_i\cdot\vec{n}dS\right] \\
&= \frac{\rho}{2}\left[0+\int_B\left[\Omega^2\left(\vec{x}-\vec{x}_C\right)^2-\left(\vec{\Omega}\cdot\left(\vec{x}-\vec{x}_C\right)\right)^2\right] n_i dS + 2\left(\vec{U}_C\times\vec{\Omega}\right)\cdot\vec{e}_i V_B\right] \\
&= \frac{\rho}{2}\left[0+\vec{e}_i\cdot\int_{V_B}\vec{\nabla}\left[\Omega^2\left(\vec{x}-\vec{x}_C\right)^2-\left(\vec{\Omega}\cdot\left(\vec{x}-\vec{x}_C\right)\right)^2\right] dV + 2\left(\vec{U}_C\times\vec{\Omega}\right)\cdot\vec{e}_i V_B\right] \\
&= \frac{\rho}{2}\left[0+0-0+2\left(\vec{U}_C\times\vec{\Omega}\right)\cdot\vec{e}_i V_B\right] \\
&= \rho V_B\left(\vec{U}_C\times\vec{\Omega}\right)\cdot\vec{e}_i
\end{aligned}
$$

and this leads to the following expression for this term:

$$
\frac{\rho}{2}\int_B U^2 n_i dS = \rho V_B\left(\vec{U}_C\times\vec{\Omega}\right)\cdot\vec{e}_i \tag{3-14}
$$

where V_B is the body volume, $\vec{U}_C$ is the translational velocity of the center-of-mass (CoM), $\vec{\Omega}$ is rotational velocity and $\vec{x}$ and $\vec{x}_C$ represent the local coordinates and the coordinates of CoM respectively. The RHS in Eq. (3-14) shows that this force is some kind of body Coriolis force resulting from the simultaneous rotation and translation of the body.

For an unbounded domain, F_ϕ^i in Eq. (3-10e) can be proved to be zero,

$$
\rho\int_B \vec{n}\cdot\left(\vec{\nabla}\left(\frac{1}{2}u_\Phi^2\right)\phi^{(i)}\right) dS = 0 \tag{3-15}
$$

The following is the proof of Eq. (3-15) for solid bodies. For unsteady potential flow, according to Bernoulli Equation, we have

$$\vec{\nabla}\left(\frac{1}{2}u_{\Phi}^2+p_{\Phi}+\frac{\partial\Phi}{\partial t}\right)=0$$

where Φ is the real potential function associated with the body instantaneous kinematics. Therefore,

$$\rho\int_B \vec{n}\cdot\left(\vec{\nabla}\left(\frac{1}{2}u_{\Phi}^2\right)\phi^{(i)}\right)dS=-\rho\int_B \vec{n}\cdot\left(\vec{\nabla}p_{\Phi}\phi^{(i)}\right)dS-\rho\int_B \vec{n}\cdot\frac{\partial\vec{u}_{\Phi}}{\partial t}\phi^{(i)}dS$$

Since $\rho\int_{\Sigma}\vec{n}\cdot\frac{\partial\vec{u}_{\Phi}}{\partial t}\phi^{(i)}dS\sim O(\frac{1}{r^d})$ this implies that, for infinitely large unbounded domain, $\rho\int_{\Sigma}\vec{n}\cdot\frac{\partial\vec{u}_{\Phi}}{\partial t}\phi^{(i)}dS=0$, so that

$$\begin{aligned}\rho\int_B \vec{n}\cdot\left(\vec{\nabla}\left(\frac{1}{2}u_{\Phi}^2\right)\phi^{(i)}\right)dS&=-\rho\int_B \vec{n}\cdot\left(\vec{\nabla}p_{\Phi}\phi^{(i)}\right)dS-\rho\int_{B+\Sigma}\vec{n}\cdot\frac{\partial\vec{u}_{\Phi}}{\partial t}\phi^{(i)}dS\\&=-\rho\int_B \vec{n}\cdot\left(\vec{\nabla}p_{\Phi}\phi^{(i)}\right)dS-\rho\int_{V_f}\vec{\nabla}\cdot\left(\frac{\partial\vec{u}_{\Phi}}{\partial t}\phi^{(i)}\right)dS\end{aligned}$$

From Eq. (3-10), we can show that,

$$\begin{aligned}\rho\int_B \vec{n}\cdot\left(\vec{\nabla}\left(\frac{1}{2}u_{\Phi}^2\right)\phi^{(i)}\right)dS&=-\rho\int_B \vec{n}\cdot\left(\vec{\nabla}p_{\Phi}\phi^{(i)}\right)dS-\rho\int_{B+\Sigma}\vec{n}\cdot\frac{\partial\vec{u}_{\Phi}}{\partial t}\phi^{(i)}dS\\&=-\rho\int_B \vec{n}\cdot\left(\vec{\nabla}p_{\Phi}\phi^{(i)}\right)dS-\rho\int_{V_f}\vec{\nabla}\cdot\left(\frac{\partial\vec{u}_{\Phi}}{\partial t}\phi^{(i)}\right)dS\\&=-\rho\int_B \vec{n}\cdot\left(\vec{\nabla}p_{\Phi}\phi^{(i)}\right)dS-\rho\int_{B+\Sigma}\vec{n}\cdot\frac{d\vec{U}_{\Phi}}{dt}\phi^{(i)}dS+\rho\int_{V_f}\vec{\nabla}\cdot\left(\vec{\nabla}\left(\frac{1}{2}u_{\Phi}^2\right)\phi^{(i)}\right)dV\end{aligned}$$

Finally, we have $\rho\int_B \vec{n}\cdot\left(\vec{\nabla}p_{\Phi}\phi^{(i)}\right)dS=-\rho\int_{B+\Sigma}\vec{n}\cdot\frac{d\vec{U}_{\Phi}}{dt}\phi^{(i)}dS$.

On the other hand, we consider for steady potential flow with exactly the same instantaneous body kinematics, we have

$$\vec{\nabla}\left(\frac{1}{2}u_{\Phi}'^{2}+p_{\Phi}'\right)=0$$

where p_{Φ}' is the pressure of the steady potential flow. Note that since the body kinematics is the same at $t=\tau$, so that the induced steady flow velocity is the same as unsteady flow velocity instantaneously,

$$u_{\Phi}'=u_{\Phi}\left(t\right),\ t=\tau$$

In the end, we found that,

$$F_{\phi}^{i}=\rho\int_{B}\vec{n}\cdot\left(\vec{\nabla}\left(\frac{1}{2}u_{\Phi}^{2}\right)\phi^{(i)}\right)dS=\rho\int_{B}\vec{n}\cdot\left(\vec{\nabla}\left(\frac{1}{2}u_{\Phi}'^{2}\right)\phi^{(i)}\right)dS=-\rho\int_{B}\vec{n}\cdot\left(\vec{\nabla}p_{\Phi}'\phi^{(i)}\right)dS=0$$

Therefore, for a non-deforming body moving in an unbounded fluid domain, the total added mass force has the following expression,

$$F_{\kappa}^{i}=-\rho\int_{B}\vec{n}\cdot\frac{d\vec{U}}{dt}\phi^{(i)}dS-\rho V_{B}\left(\vec{U}_{C}\times\vec{\Omega}\right)\cdot\vec{e}_{i} \tag{3-16}$$

Using the Helmholtz decomposition (Eq. (3-6)), which separates the total velocity into a potential part and a vorticity part, the total added mass force can be further decomposed as follows:

$$\begin{aligned}F_{\kappa}^{i}&=-\rho\int_{B}\vec{n}\cdot\frac{d\vec{U}}{dt}\phi^{(i)}dS-\rho V_{B}\left(\vec{U}_{C}\times\vec{\Omega}\right)\cdot\vec{e}_{i}\\&=-\rho\int_{B}\vec{n}\cdot\frac{d\vec{U}_{\Phi}}{dt}\phi^{(i)}dS-\rho\int_{B}\vec{n}\cdot\frac{d\vec{U}_{v}}{dt}\phi^{(i)}dS-\rho V_{B}\left(\vec{U}_{C}\times\vec{\Omega}\right)\cdot\vec{e}_{i}\end{aligned} \tag{3-17}$$

where $\vec{U}_{\Phi}$ and $\vec{U}_{v}$ are the surface velocity components induced by potential flow and the viscous rotational flow respectively.

From Eq. (3-8) & (3-17), it is straightforward that when a non-deforming body is translating in the flow without rotation, term $\frac{d\vec{U}_v}{dt}\cdot\vec{n}$ is zero so that the total added mass force F_κ^i is equivalent to classical added mass force F_{PF}^i in this scenario. For example, in i direction, the analytical expression of total added mass force can be obtained in the same expression of classical added mass force.

In order to better understand the terms in the above equation, consider a solid sphere translating and accelerating in an otherwise quiescent flow. In order to compute the total added mass force on this sphere, we need solve the harmonic function first. In this spherically symmetric case, the analytical solution of harmonic function $\phi^{(i)}$ in Eq. (3-5) can be easily found as,

$$\phi^{(i)} = -\frac{R^3\cos\theta}{2r^2}$$

where r and θ represent the radial coordinate and zenith angle and R is the radius of the solid sphere. Therefore, for a sphere translating in i direction, the total added mass force is

$$\begin{aligned}
F_\kappa^i &= -\rho\int_B \vec{n}\cdot\frac{d\vec{U}_\Phi}{dt}\phi^{(i)}dS \\
&= -\rho\int_B \vec{n}\cdot\frac{d\vec{U}}{dt}\phi^{(i)}dS \\
&= -\rho\frac{d\vec{U}}{dt}\cdot\vec{e}_i\int_0^{2\pi}\int_0^{\pi}\cos\theta\frac{R\cos\theta}{2}R^2\sin\theta d\theta d\phi \\
&= -\rho\frac{d\vec{U}}{dt}\cdot\vec{e}_i\pi R^3\int_0^{\pi}\cos^2\theta d\cos\theta \\
&= \rho\frac{2\pi R^3}{3}\frac{dU_i}{dt}
\end{aligned}$$

where U_i is the translational velocity. This is the classical expression for the added-mass force on an accelerating sphere (Batchelor 1967). Thus, the first term in Eq. 3-17 is indeed the classical added mass force term

However for the more general case body that is undergoing a complex combination of translation and rotation or is deforming, the term $\frac{d\vec{U}_v}{dt}\cdot\vec{n}$ may not be zero, and would then contribute to the net force on the body. In order to better understand the physical underpinning of this force, we consider a case with a solid semi-circular plate (arc) rotating about its center in a large fluid domain. We choose the following conditions for this plate: radius= $0.2m$ and the rotational velocity= $3.14 rad/s$ and Reynolds number equal to 5000. This high Reynolds number is chosen so as to minimize the force due to viscous shear on the plate.

The total (centripetal) added mass force for this only consists of the second term in Eq. 3-17 since $\vec{U}_n$ is zero and V_B is zero. It is relatively easy to obtain the expression for the lift force associated with the second term in Eq. 3-17 as

$$
\begin{aligned}
F_K^y &= -\rho\int_B \vec{n}\cdot\frac{d\vec{U}}{dt}\phi^{(2)}dS \\
&= -\rho\int_B \vec{n}\cdot\frac{d\vec{U}_v}{dt}\phi^{(2)}dS \\
&= -\rho\omega^2 R\int_B \phi^{(2)}dS \\
&= -\rho\omega^2 R\int_0^{\pi}\left(-R\sin\theta\right)Rd\theta \\
&= -2\rho\omega^2 R^3 \approx -0.496\left(N\right)
\end{aligned}
$$

where the fluid density ρ is assumed to be equal to one. Thus, this is a case for which the second term in the total added mass force is the dominant term and one can obtain an analytical expression of the force for validation.

The simulations for this case are conducted using ViCar3D on a dense, 1024x1024 grid (Fig. 3-3 b) and. Fig3-3c shows the time variation of the various components of the lift force in the early stages of the rotation where no vorticity has been shed from the plate. As can be seen, the total added mass force dominates the total force and its predicted value is very nearly equal to that obtained from the analytical expression.

We can now conjecture as to the physical origin of the force associated with the second term in the total added mass force i.e. $\int_B \frac{d\vec{U}_v}{dt} \cdot \vec{n}\phi^{(i)} dS$. It is our view that just as the classical added mass force is considered a reaction to the linear acceleration of the body (relative to the flow), the force associated with the second term should be considered a reaction to the centripetal acceleration of the flow adjacent to the body. This force component is only activated if the no-slip boundary conditions is satisfied since only then can the body impart a tangential acceleration to the fluid layer adjacent to it. The term also requires local rotation of the body otherwise $\frac{d\vec{U}_v}{dt} \cdot \vec{n}$ is identically zero. Thus, any body undergoing complex motions in a viscous fluid (such as a flapping insect wing for instance), is expected to experience this type of force.

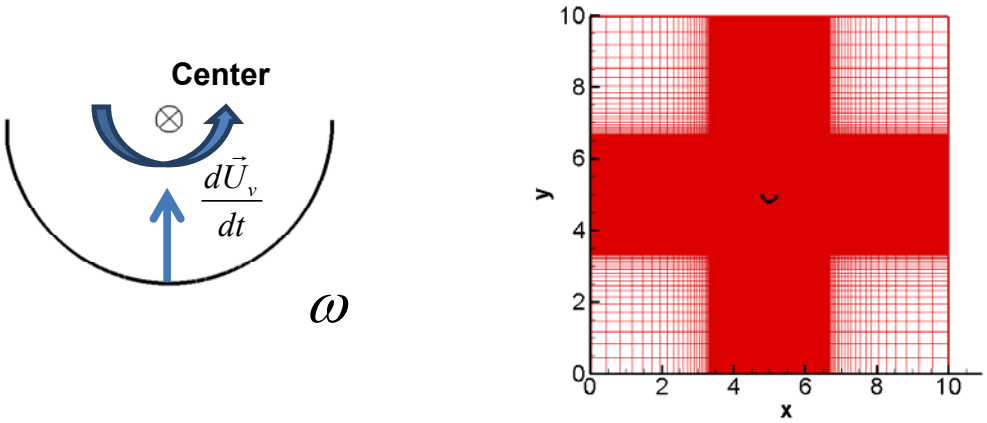

(a) (b)

Figure 3-2 (a) Schematic of 2D rotating semi-circular plate (b) Computational Set-up

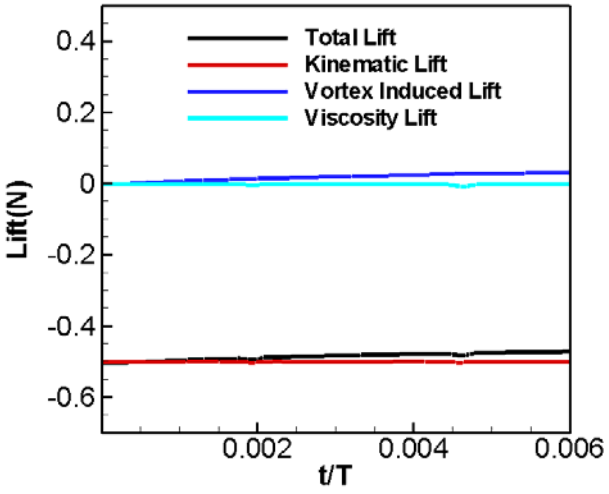

Figure 3-3 Lift components of rotating semi-circular plate

3.3.3. Vortex Induced Force

Usually vortex-induced forces play a dominant role in generation of hydro/aerodynamic forces and these forces are particularly important in the study of insect flight. For instance, the leading-edge vortex is known to be important for lift generation in flapping flight (Ellington, et al, 1996; Dickinson, et al, 1999). Moreover, the interaction of a flapping wing with vortices created during a previous stroke (so called "wake-capture") is known to provide additional lift for some insects. However, it has typically been difficult to precisely determine the contribution of individual vortices on force production and most of the past studies have relied on indirect (and imprecise) methods for determining the contribution of vortices to force production.

In this regard, since we can evaluate the integral in F_{ω}^{i} in Eq. (3-10c) for every local patch of vorticity, our FPM can be deployed to determine the contribution of any particular vortex on force generation with a precision that has not been available before. In order to demonstrate this we consider the canonical case of flow past a circular cylinder at a Reynolds number of 1000. The flow domain is $25D \times 10D$ (D is the diameter of cylinder) in dimension and discretized by 1024×256 grid points with a region of fine mesh around the body and in the near wake.

Fig 3-4 shows the time series of the total drag coefficient calculated by the traditional method (TM) that employs Eq. (3-1), and the force partitioning method (FPM) formulation (Eq. (3-10)); also included in the plot are the vortex-induced and viscous components of the drag force as calculated from FPM. Note that the total added mass force is zero for this case. The result of the FPM shows very good agreement with the

result obtained by the traditional method and this validates the overall numerical procedure used in the FPM method.

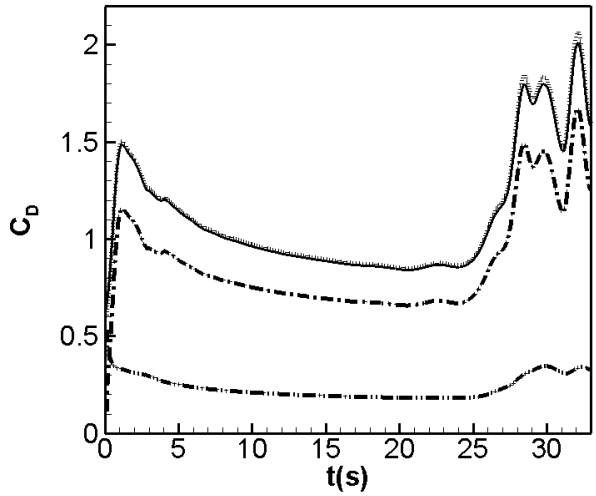

Figure 3-4 Time Series of drag coefficients. "——": total drag coefficient by TM; "……": total drag coefficient by FPM; "– . – ": vortex induced drag coefficient; "— . .": viscous drag coefficient.

Given Reynolds number is relatively high, the vortex induced force dominates the overall drag force. It is about 77% of the time-averaged total drag at fully-developed stage. When the flow is nearing the stationary state ($t = 34s$), we visualize the local vortex induced drag contribution by plotting the integrand in Eq. (3-10c) as shown in Fig 3-5. From the contour of local vortex induced drag, we clearly see that the majority of vortex-induced drag is contributed by vortices located very close to the cylinder. This is the consequence of decaying effect of the harmonic function $\phi^{(x)}$, which damps out the contribution of drag from vortices in the far field.

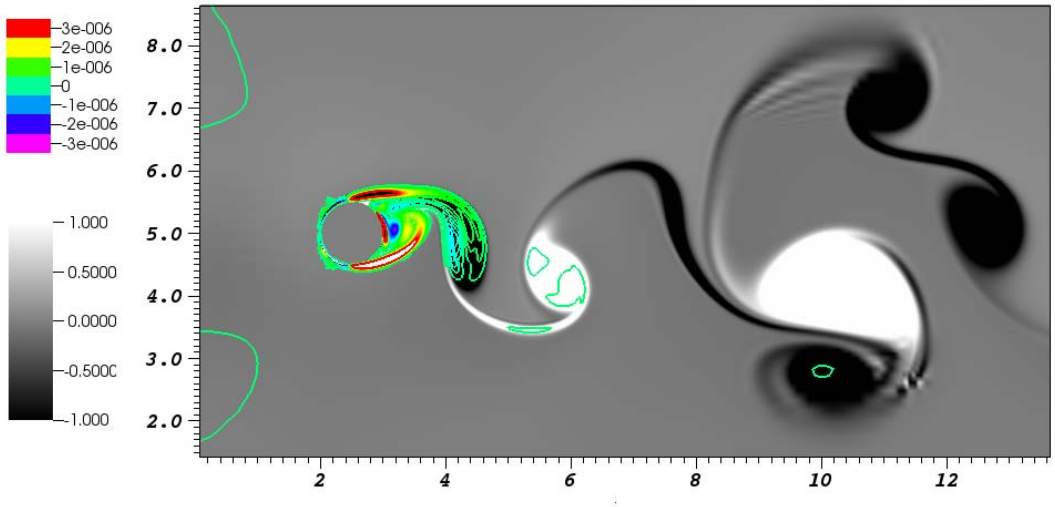

Figure 3-5 Black and white heat-map of vorticity field and color contour of local vortex induced drag.

If we carry out the similar analysis as in Eq. (3-12), we will easily find that for a fluid domain with open boundary, the rate of decay for fluid velocity with the distance from the body is given by:

$$|\vec{u}| \sim O\left(\frac{1}{r^d}\right) \tag{3-18}$$

Also due to Stokes' theorem $\oint_{\partial V} \vec{n} \times \vec{u} dS = \int_V \vec{\omega} dV$, we can easily find the decaying order for vorticity,

$$|\vec{\omega}| \sim O\left(\frac{1}{r^{d+1}}\right) \tag{3-19}$$

Thus, the decaying order of vortex induced force in an open domain is determined to be given by

$$F_\omega^i \sim O\left(\frac{1}{r^{2d+1}}\right) \tag{3-20}$$

In this 2D case, the order of decay of the vortex induced drag should be five. For validation of this scaling via our simulation, we split the wake region into strips of width D and then plot the integrated vortex induced drag for each strip as a function of the distance from the cylinder. The linear data-fitted line in Fig 3-6 clearly shows that the decaying order of vortex induced drag is pretty close to what we expect.

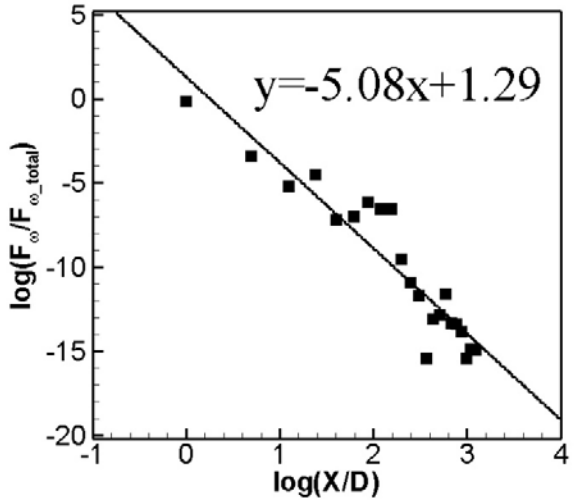

Figure 3-6 of vortex induced drag with distance from the cylinder.

3.3.4. Viscous Force

The concept of the viscous force in Eq. (3-10d) is also subtly different from the shear stress force calculated by integrating the shearing stress over the body surface (Batchelor, 1967) as shown in the equation below:

$$F_s^i = \vec{e}_i \cdot \int_B \vec{\tau}_w dS, \quad where\ \vec{\tau}_w = 2\vec{n} \cdot \vec{\nabla}\vec{u} + \vec{n} \times \vec{\omega} \tag{3-21}$$

Note that it is the only component explicitly related to viscosity, therefore it can represent the total force when it is in Stokes flow regime ($\mathrm{Re} \ll 1$), because the infinitesimally small Reynolds number makes the viscous force overwhelmingly dominate in the force production.

We use Stokes flow past a sphere with velocity U to examine the contribution of this force component. The harmonic function $\phi^{(i)}$ for this case is,

$$\phi^{(i)} = -\frac{R^3 \cos\theta}{2r^2}$$

The expression for the vorticity associated with this flow is also known (Batchelor, 1967) to be given by following

$$\vec{\omega} = \left(0, 0, -\frac{3U \sin\theta R}{2r^2}\right) \quad and \quad \vec{\omega} \times \vec{n} = \left(0, -\frac{3U \sin\theta R}{2r^2}, 0\right)$$

Therefore, the viscous force (which is also the total force for this case) exerted on the solid sphere is

$$\begin{aligned}
F_\sigma^i &= \mu \int_B (\vec{\omega} \times \vec{n}) \cdot \vec{\nabla} \left(\phi^{(i)} - x_i\right) dS \\
&= \mu \int_0^{2\pi} \int_0^{\pi} (\vec{\omega} \times \vec{n}) \cdot \vec{\nabla} \left(-\frac{R^3 \cos\theta}{2r^2} \right)\Bigg|_{r=R} R^2 \sin\theta d\theta d\phi - \mu \int_0^{2\pi} \int_0^{\pi} (\vec{\omega} \times \vec{n}) \cdot \vec{\nabla} \left(r \cos\theta\right)\Big|_{r=R} R^2 \sin\theta d\theta d\phi \\
&= \mu \int_0^{2\pi} \int_0^{\pi} \left(0, -\frac{3U \sin\theta}{2R}, 0\right) \cdot \left(\cos\theta, \frac{1}{2}\sin\theta, 0\right) R^2 \sin\theta d\theta d\phi - \\
&\quad \mu \int_0^{2\pi} \int_0^{\pi} \left(0, -\frac{3U \sin\theta}{2R}, 0\right) \cdot (\cos\theta, -\sin\theta, 0) R^2 \sin\theta d\theta d\phi \\
&= -\mu \int_0^{2\pi} \int_0^{\pi} \frac{3U \sin\theta}{2R} \cdot \frac{1}{2} \sin\theta R^2 \sin\theta d\theta d\phi - \\
&\quad \mu \int_0^{2\pi} \int_0^{\pi} \frac{3U \sin\theta}{2R} \sin\theta R^2 \sin\theta d\theta d\phi \\
&= 2\pi\mu UR + 4\pi\mu UR = 6\pi\mu UR
\end{aligned}$$

The result via the FPM agrees with the analytical solution for drag force of sphere in Stokes flow (Batchelor, 1967). We point out there that the FPM indicates that the viscous contribution is split into two parts: $\mu\int_B (\vec{\omega}\times\vec{n})\cdot\vec{\nabla}\phi^{(i)}dS\,(=2\pi\mu UR)$ is the pressure force on the solid sphere induced by the viscous diffusion of momentum into the flow and $-\mu\int_B (\vec{\omega}\times\vec{n})\cdot\vec{\nabla}x_i dS\,(=4\pi\mu UR)$ is force due to the surface shear stress.

3.3.5. Outer Boundary Force

The FPM provides a distinct expression for the contribution of the flow at the outer boundary on the force on the body. The scaling of the individual terms in this force component can be estimated as follows;

$$\begin{cases} \rho\int_\Sigma \vec{n}\cdot\dfrac{d\vec{v}'}{dt}\phi^{(i)}dS \sim O\left(\dfrac{V_B}{r^d}\right) \\ \rho\int_\Sigma \vec{n}\cdot\left(\vec{\nabla}\left(\dfrac{1}{2}u_\Phi^2\right)\phi^{(i)}\right)dS \sim O\left(\dfrac{V_B}{r^{2d}}\right) \\ \mu\int_\Sigma (\vec{\omega}\times\vec{n})\cdot\vec{\nabla}\phi^{(i)}dS \sim O\left(\dfrac{V_B}{r^{d+2}}\right) \end{cases} \tag{3-22}$$

where r is the distance and V_B is the immersed body volume. Since rate of decay is very large, the outer boundary force as shown in Eq. (3-10e) can be approximated to be zero when a large-enough control volume is employed.

3.4. Conclusion

In this chapter, we describe the derivation and analysis of a novel force partitioning method. Based on this method the total force experienced by a body is decomposed into distinct components, each of which is associated with a clear physical mechanisms. Simple cases are used to validate and assess the various force components. This theory is

general and comprehensive and works for complex deforming bodies in an incompressible flow; it therefore provides a powerful tool to investigate the mechanism of force production in virtually all fields of fluid dynamics, and, in particular, to vortex dominated flows and flows with dynamically moving bodies. Similarly, the mechanism of centripetal added mass force that has been identified here likely plays an important role in flows that involve bodies undergoing complex motions such as those encountered in the flying and swimming of animals, flow induced vibration and deformation in biology and engineering, and multiphase flows.

Application of FPM to the analysis of insect flight is described in Chapter 4.

CHAPTER 4. INSIGHTS INTO MECHANISMS FOR LIFT GENERATION IN INSECT FLIGHT

4.1. Introduction

Despite intense study by physicists and biologists, we do not fully understand the unsteady aerodynamics that relate insect wing morphology and kinematics to lift generation. Here, we use force partitioning method (FPM) discussed in Chapter 3 and implement it within a computational fluid dynamic model to provide an unambiguous and physically insightful division of aerodynamic force into components associated with wing kinematics, vorticity, and viscosity.

In this context, computational fluid dynamic (CFD) modeling has the potential to provide all the quantities needed for a clear delineation of force production. However, straightforward analysis of pressure and viscous shear on the wing surface does not provide a quantitative delineation of the underlying mechanisms. As discussed in Chapter 3, while CFD can provide all the surface as well as field quantities at each time-instance, this does not distinguish the partial contributions of the different mechanisms.

In Chapter 3, we have described the derivation of a formulation of the total force exerted by an incompressible Newtonian flow on an immersed body such that it clearly delineates the partial contributions of various physical mechanisms and features to the total aerodynamic force. This force partitioning method (FPM), is implemented into a three-dimensional, sharp-interface immersed boundary Navier-Stokes solver (Mittal et al, 2008). Using this method, we are able to partition the total instantaneous aerodynamic force on a flapping wing into components associated with wing kinematics, vorticity, and viscous shear and dissipation.

The formulation is applied to the flapping wings of a hovering Manduca sexta (hawkmoth) and a Drosophila (fruit fly) to reveal the similarities and differences in the mechanism of lift production of these distinct flyers. Besides the dissimilarities in hovering kinematics and the shape and deformation characteristics of the wings (as seen in Fig. 4-1), the two flyers operate in Reynolds number regimes that are separated by over an order of magnitude. A comparative analysis of these two models therefore provides an excellent substrate for investigating the scaling of force production, especially lift generation, with scale.

Our analysis conclusively shows that while the LEV is the dominant mechanism for lift generation in these flapping wings, there is an additional mechanism, the "centripetal" added-mass force, that provides a significant contribution to the total lift force. This force component is completely determined by the acceleration of the wing tangential to its surface and has, to our knowledge, not been identified in any past study of flapping flight. This component of the lift force is generated with minimal power expenditure and is independent of the Reynolds number as well as environmental disturbances; as such it represents an efficient and robust mechanism for weight support at all scales. The implications of this new force generation mechanism go far beyond insect flight since this mechanism could also play an important role in a wide variety of vortex dominated flows as well as flows that involve bodies undergoing dynamic motion and deformation.

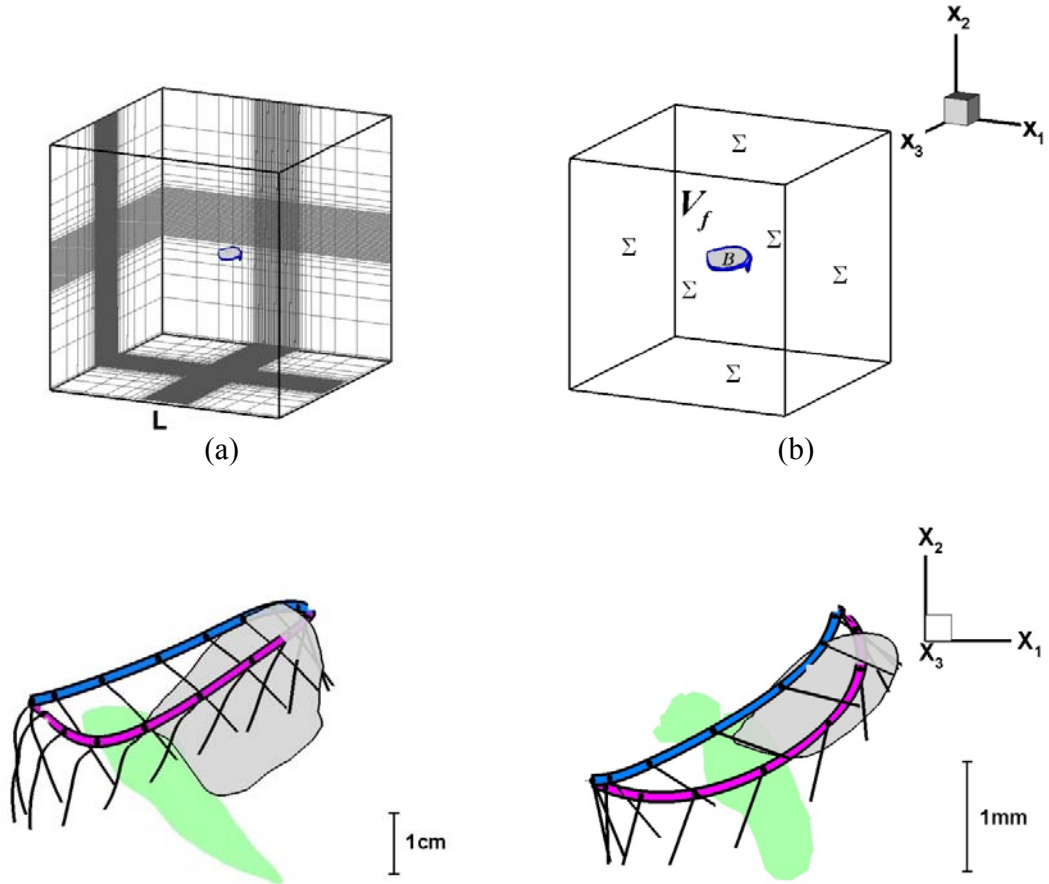

Figure 4-1 (a) Typical non-uniform Cartesian mesh employed in the current simulations. (b)

Schematic of the control volume (not to scale) employed for the simulations and FPM. (c) Kinematics of the wing of the hovering hawkmoth and (d) fruit fly. In these two plots, the trajectory of the leading edge of the wings at 2/3 span is identified by a thick line which is blue during downstroke and pink during upstroke. The chordlines at 2/3 span are also identified for up to 16 different phases in the flapping cycle by black lines with circular "heads". Time series of three characteristic angles (see insect in (f)) that define the wing kinematics for the (e) hawkmoth and (f) the fruit fly.

4.2. Force Partitioning Method (FPM)

As shown in Chapter 3, the derivation of FPM starts with the Lamb-Gromeka form of the Navier-Stokes equations. This equation is projected onto the gradient of $\phi^{(i)}$ for $i=1,2,3$, where $\phi^{(i)}(\tau)$ is the potential associated with the inviscid, irrotational flow past the body with shape and location corresponding to $t=\tau$, translating in the x_i direction with unit velocity. Following this projection and rearrangement of the various terms in this equation and the use of the Helmholtz velocity decomposition, we obtain the following partitioning of the total force on the wing

$$F_B^i = F_\kappa^i + F_\omega^i + F_\sigma^i + F_\phi^i + F_\Sigma^i, \quad for\ i=1,2,3;\ where \tag{4-2a}$$

$$F_\kappa^i = \underbrace{-\rho\int_B \vec{n}\cdot\frac{d\vec{U}}{dt}\phi^{(i)}dS}_{F_{\kappa I}^i} \underbrace{-\frac{1}{2}\rho\int_B U^2 n_i dS}_{F_{\kappa II}^i=0} \tag{4-2b}$$

$$F_\omega^i = \rho\int_{V_f}\vec{\nabla}\cdot\left[\vec{\nabla}\left(\vec{u}_v\cdot\vec{u}_\phi+\frac{1}{2}\vec{u}_v\cdot\vec{u}_v\right)\phi^{(i)}\right]dV + \rho\int_{V_f}\left[\vec{\nabla}\cdot\left(\vec{\omega}\times\vec{u}\right)\right]\phi^{(i)}dV \tag{4-2c}$$

$$F_\sigma^i = \mu\int_B\left(\vec{\omega}\times\vec{n}\right)\cdot\vec{\nabla}\left(\phi^{(i)}-x_i\right)dS \tag{4-2d}$$

$$F_{\phi}^{i} = \rho \int_{B} \vec{n} \cdot \left(\vec{\nabla} \left(\frac{1}{2} u_{\phi}^{2} \right) \phi^{(i)} \right) dS \tag{4-2e}$$

$$F_{\Sigma}^{i} = -\rho \int_{\Sigma} \vec{n} \cdot \frac{d\vec{v}'}{dt} \phi^{(i)} dS + \rho \int_{\Sigma} \vec{n} \cdot \left(\vec{\nabla} \left(\frac{1}{2} u_{\phi}^{2} \right) \phi^{(i)} \right) dS + \mu \int_{\Sigma} \left(\vec{\omega} \times \vec{n} \right) \cdot \vec{\nabla} \phi^{(i)} dS \tag{4-2f}$$

where $\vec{U}$ is the velocity of the surface of the wing and $\vec{u}_{\phi}$ and $\vec{u}_{v}$ are the curl-free (irrotational) and divergence-free (viscous) components of flow velocity respectively. In the above equations, F_{κ}^{i} is a force component that is determined solely by the kinematics (shape, velocity and acceleration) of the wing. In the first integral in this term (denoted by $F_{\kappa_I}^{i}$) $\frac{d\vec{U}}{dt}$ denotes the material acceleration of the immersed body and this force component is totally independent of the flow velocity and vorticity in the surrounding fluid, this is the total added-mass force. The second integral in F_{κ}^{i} (denoted by $F_{\kappa_{II}}^{i}$) depends only on the surface velocity.

Given that $\vec{u}_{v} = 0$ if $\vec{\omega} = 0$ (see details in Chapter 3), the force component F_{ω}^{i} is identically zero if $\vec{\omega}$ is zero; this force component is therefore associated exclusively with the vorticity in the flow. The component F_{σ}^{i} consists of the viscous wall shear as well as pressure induced by the viscous dissipation in the flow. The component F_{ϕ}^{i} is the force associated exclusively with the curl-free or potential component of the flow ($\vec{u}_{\phi}$) within the domain. Finally, F_{Σ}^{i} is the force contribution associated with the flow perturbation ($\vec{v}'$) and viscous shear on the outer boundary of the domain. $F_{\kappa_{II}}^{i}$ is identically zero for a zero-thickness membrane such as the wings modeled here, and as shown in Chapter 3, F_{ϕ}^{i} and F_{Σ}^{i} are zero (unbounded infinite large domain) compared to

the other force components for the cases simulated here; we therefore focus our attention on $F^i_{\kappa_1}$, F^i_{ω} and F^i_{σ}.

Flapping kinematics derived from two different insects, a hawkmoth and a fruit fly, form the basis of the current study. For the hawkmoth, the instantaneous 3D wing shape and kinematics were quantified via high-speed stereo videogrammetry from recordings of the animal hovering steadily in front of an artificial flower (Zheng et al., 2013). For the fruit fly, a flat-plate wing was constructed from a high-resolution image of a fruit fly wing. Flapping kinematics consisting of three angular degrees of freedom were then extracted via high-speed stereo videogrammetry of a fruit fly in flight, hovering shortly after takeoff, and imposed on the wing, resulting in rigid wing flapping kinematics. Fruit fly wings exhibit little deformation and the use of rigid wing kinematics is typical of mechanical (Sane et al., 2001) and computational (Ramamurti et al., 2002) models of the flight of these animals. The wing Reynolds number, defined as $\mathrm{Re} = \vec{V}_{tip}\bar{C}/\nu$, where $\vec{V}_{tip}$ and $\bar{C}$ are the average wingtip velocity and span-averaged wing-chord respectively, match typical values for these insects (1000 for the hawkmoth and 100 for the fruit fly). Simulations for these cases are carried out with an immersed boundary flow solver (Mittal, et al, 2008) and the resulting velocity and vorticity fields subjected to FPM. The grid topology and the computational domain employed in these simulations are shown in Fig. 4-1(a) and Fig. 4-1(b), respectively. Based on our previous experience in simulating such flows (Zheng, et al, 2013), grids with sizes ranging from 10 to 16 million points were chosen for the current simulations, and time-steps per flapping cycle ranged from 2500 to 4200 (Ellington, 1984).

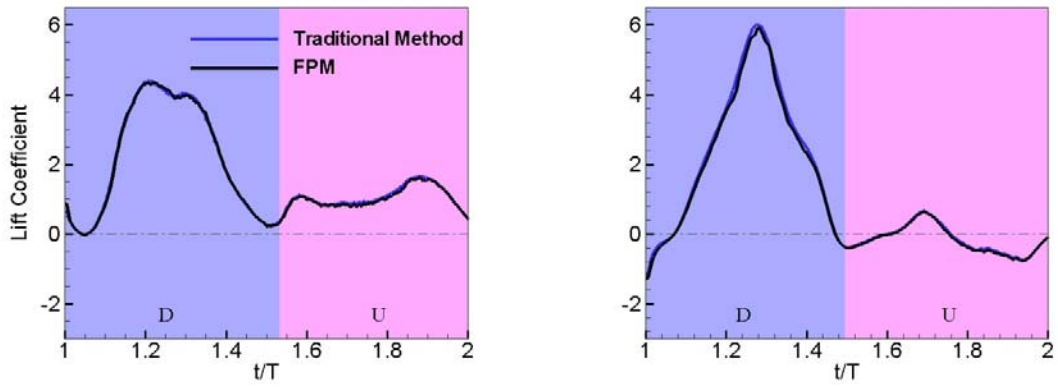

Figure 4-2 Comparison of lift calculation by traditional method (blue line) and Force Partitioning Method (FPM) (black line) in (a) Hovering Hawkmoth flight at Re=1000 and (b) Hovering Fruit fly at Re=100 throughout a full stroke cycle.

Table 4-1: Stroke-averaged lift and power coefficients for hawkmoth wing (Re=1000) and fruit fly wing (Re=100). Values in parentheses denote the percentage of the total attributed to the given component.

	Coeffs	Total	Added Mass		Vortex-Induced		Viscous	
			Value	Percent	Value	Percent	Value	Percent
Hawkmoth (Re=1000)	Lift	1.65	0.29	17.3%	1.36	82.5%	0.00	0.2%
	Power	3.64	0.02	0.5%	3.59	98.4%	0.04	1.0%
Fruit-fly (Re=100)	Lift	1.06	0.10	9.5%	1.22	114.5%	-0.27	-25.0%
	Power	4.06	0.02	0.5%	3.35	82.4%	0.69	17.0%

4.3. Validation

4.3.1. Lift Calculation via FPM v.s. Traditional Method

The total force computed from the traditional method, i.e. by integrating the pressure and shear on the surface (see Eq. (4-1)) should, in principle, match that obtained by applying FPM to the computed velocity and vorticity field. However, we note that Eq. (4-2) contains derivative terms above and beyond those in the Navier-Stokes equations (such as those in F_ω) that might be subject to truncation errors when evaluated using finite-difference methods. In the current study, we have evaluated all terms in Eq. (4-2) using a second-order central-difference scheme, which is consistent with the underlying flow solver. In Fig. 4-2 we compare the time-variation of the total lift obtained by the traditional method with that obtained from FPM for both cases and it should be noted that the differences are extremely small. This not only provides a consistency check for the FPM but also indicates that any discretization errors associated with the implementation of the FPM are negligible.

It is further noted that $F^i_{\kappa_{II}}$ is identically equal to zero at each time-instant for a zero thickness membrane such as the insect wings that are modeled here since the contribution to the surface integral from one side of the wing cancels out the contribution from the other side. Furthermore, dimensional analysis indicates that for a compact body in a three-dimensional domain, $F_\Sigma \sim O\left(\frac{1}{r^3}, \frac{\mu}{r^5}\right)$ where r is the distance between the body and the outer boundary of the domain.

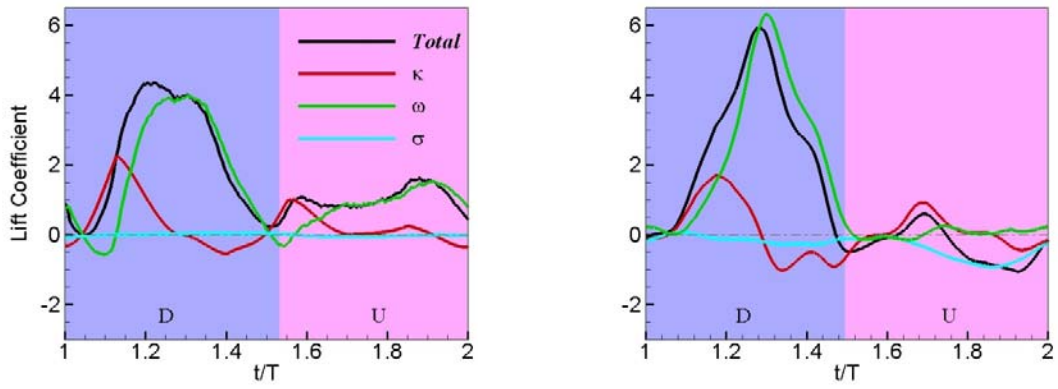

Figure 4-3 Components of instantaneous lift coefficient over one flapping cycle for the (a) hovering hawkmoth at Re=1000, and the (b) fruit fly at Re=100. The stroke is divided into two phases: downstroke (D) and upstroke (U).

Thus, a sufficiently large domain ensures that this term does not have a significant contribution to the force. Indeed, for the domain sizes employed in the current simulations, the root-mean square of the lift coefficient associated with this term is at most $O\left(10^{-4}\right)$, which is negligible compared to the $O(1)$ magnitude of the total lift. Similarly, the F_ϕ lift coefficient is also found to be $O\left(10^{-5}\right)$, and therefore negligible.

4.3.2. Numerical Validation of Dynamical Scaled Mechanical Fruit-fly Wing Model

Sane et al. (2001) have investigated the force production of a flapping wing via a dynamical scaled mechanical fruit-fly wing model which can perform different wing kinematics. Thier primary conclusion is that the quasi-steady model significantly underestimates the real lift generation especially during the beginning of each stroke

(wing rotation period). Thereby, the discrepancy of lift generation is attributed to wake capture and induced circulation by wing rotation. However, according to our observation as in Fig. 4-3, in both cases of hovering hawkmoth and fruit-fly, there is a surge of added mass lift generation at the beginning of downstroke and upstroke, respectively. It could probably explain the mismatch of quasi-steady force production model since the added mass force is typically not accounted for in any quasi-steady model. In order to validate our assumption, we conducted a numerical simulation of one case selected from Sane's experiment and carried out the FPM analysis for this case.

In this simulation, we note that the wing shape is as same as the solid fruit-fly wing shown in Fig. 4-1(d), the wing span is $0.5m$, the density of the surrounding fluid is $0.8kg/m^3$ and the flapping frequency is 25Hz; all of these result in a wing that Reynolds number of 100. The prescribed wing kinematics can also characterized by three angles shown in Fig. 4-1(f). The time series of the three angles are plotted in Fig. 4-4. The same mesh setup is used in this simulation as in the fruit-fly wing simulation.

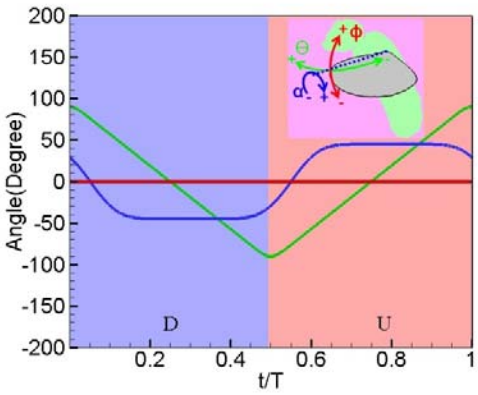

Figure 4-4 Time series of three characteristic angles: Sweeping Angle (Green), Elevation Angle (red) and AoA (Blue). The whole cycle is also divided into two phases at t/T=0.5: Downstroke

(D) and Upstroke (U). Details can be found in Sane, et al, 2001.

The CFD-calculated lift and drag are compared with the experimental result of Sane et al. (2001) in Fig. 4-5. It can be seen that both components of force are in reasonable agreement with experimental results. Moreover, as stated in Sane's paper, there exist two large peaks in both lift and drag generation at the beginning of each stroke and this is matched by the experimentsWe note that the overall match is not exact and the reason for this not clear. The CFD simulations have been checked for grid dependency and have be subjected to a comprehensive array of validation and verification studies. We do note that Sane's paper is somewhat ambiguous about some details of the wing kinematics (such as the center of pitch, and the precise distance of the rotary joint from wing root) and the simulation have made some assumptions about these unknown parameters. These might explain the slight difference between experiment and simulation data. We note here that the CFD is seen to overpredict the peak values of both the lift and drag when compared to the experiment.

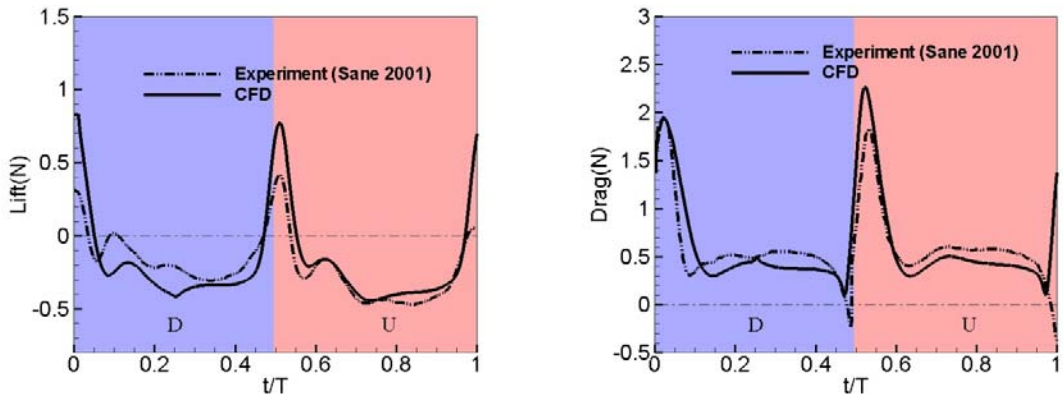

Figure 4-5 Comparison of force calculation via CFD simulation and experimental data (Sane, et al, 2001) in (a) lift component and (b) drag component.

We now partition the lift and drag into different components via FPM and the results are shown in Fig. 4-6(a)(b). It can be clearly seen that due to the large acceleration of wing motion at the beginning of each stroke, there are two high peaks of added-mass (or kinematic) components in both lift and drag. After a very short time lag with the added-mass peaks, there are also two vortex-induced peaks that follow, which could be probably attributed to the circulation enhancement of the force production due to wing rotation as quoted by Sane et al. (2001). Since the quasi-steady model is a semi-empirical model obtained by data fitting of flow past fixed wing experiments, which is expected to account for at least some part of the vortex induced viscosity-induced force into account, we can also compare the sum of vortex induced force and viscous force with the quasi-steady estimations in both lift and drag (shown in Fig. 4-6 (c)(d)).

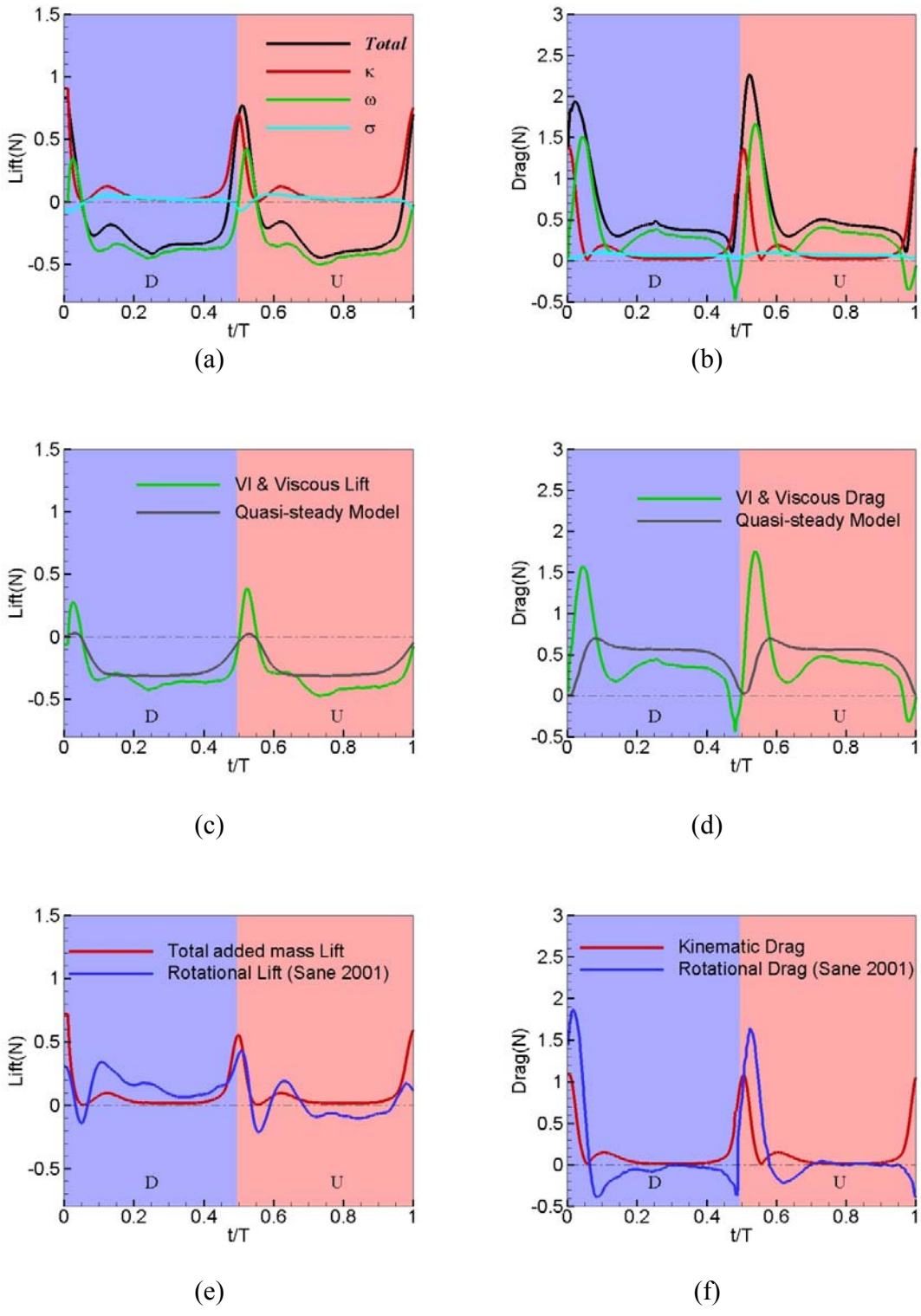

Figure 4-6 Time series of force decomposition via FPM in (a) lift and (b) drag; Comparison of

sum of vortex-induced and viscous components with quasi-steady estimated force in (c) lift and (d) drag; Comparison of total added mass lift component with "rotational" (e) lift and (f) drag.

Finally, in Fig. 4-6(e)(f) we compare the total total added mass force (which contains the linear acceleration reaction force as well as the centripetal acceleration reaction force) calculated via FPM with the corresponding estimation of the "rotational" force. We note that the rotational force in Sane et al. (2001) is defined as the difference between the total force and that obtained by the quasi-steady model. Interestingly, we note that the variations of the kinematic and the rotational lift are in phase with each other, although the magnitudes are not matched. Similarly for the drag, the two large peaks at the start of each half-strokes are somewhat in agreement with other and this suggest that the rotational lift as defined by Sane et al. (2001) has come components of total added mass force. However, we note that the decomposition of Sane et al. (2001) cannot completely match what is done in FPM since both the quasi-steady and rotational components of the force contain significant contributions of the vortex-induced lift. Nevertheless, the comparison and contrast of the FPM with the analysis of Sane et al. (2001) provides additional insights into the aerodynamic force production in flapping flight.

4.4. Results & Discussion

4.4.1. Analysis of Force Partitions

Fig 4-2 shows the time variation of the total lift coefficient (defined as $C_F = F / \rho A \beta^2 f^2 L^2$) where ρ is the fluid density, A and L the wing area and wing

length respectively, and β and f the stroke amplitude and frequency respectively) as well as its three significant components ($F^i_{\kappa_l}$, F^i_{ω} and F^i_{σ}) for the two cases studied here, and the table below summarizes the time-average values of these components over one flapping cycle. For the hawkmoth wing, the downstroke contributes the majority (70%) of the total lift but the upstroke also provides a significant (30%) contribution to weight support. In contrast, in this instance the fruit fly generates all of its weight support during the downstroke, with the upstroke and wing rotation periods generating a small net negative lift force. Thus, the differences in wing kinematics and Reynolds numbers between the two wings manifest as differences in the time course of aerodynamic force production. It is therefore expected that the application of FPM to these two contrasting configurations will provide useful and broad-based insights into lift generation with flapping wings.

The FPM demonstrates that the vortex-induced component dominates lift production for both cases. The vortex-induced lift (VIL) exhibits a large and distinct peak near mid-downstroke for both wings. During the upstroke however, while both wings generate positive VIL, the magnitudes are significant only for the hawkmoth wing. Overall, the vorticity in the flow contributes 82.5% of the total lift for the hawkmoth case where as for the fruit fly wing, the VIL is even more dominant; contributing a total of ~114% of the net lift over one stroke. This greater than 100% contribution results from the fruit fly's operation at a lower Reynolds number, where viscous forces induce a sizeable (25% of the net) negative lift over the cycle.

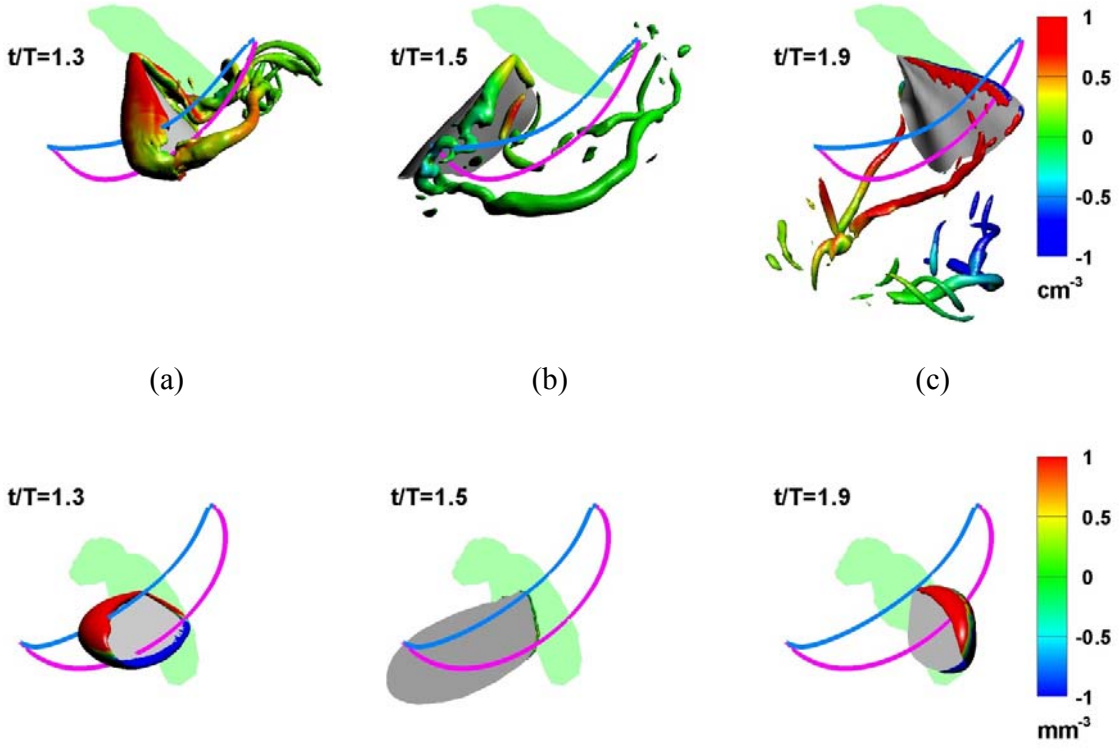

Figure 4-7 Vortex structures and local contribution of vortices to lift production. Vortex structures are identified by plotting an isosurface of the imaginary part of the complex eigenvalue of the local deformation tensor. Isosurfaces are shaded by the lift coefficient per unit volume (cm^{-3} for the hawkmoth and mm^{-3} for the fruit fly) contributed by local vorticity. Figures (a-c) and (d-f) show the three phases in the flapping of the hawkmoth and fruit fly respectively.

In the current study, since we can evaluate the integral in F_ω in Eq. (4-2) for every local patch of vorticity, our FPM can be deployed to determine the contribution of the

LEV and other vortices to lift with a precision that has not been available before (VandenBerg, et al., 1997; Birch, et al., 2001; Birch, et al., 2004). Fig. 4-7 shows the vortices over the wings color-coded for their contribution to F_ω. The hawkmoth wing, which is operating at a higher Reynolds number, generates a number of distinct vortices including the leading-edge vortex (LEV), a tip-vortex and a root-vortex. Fig. 4-7(a) which corresponds to the downstroke peak in VIL for the hawkmoth wing, indicates that the bulk of the lift-producing vorticity patches are associated with the LEV. At $t/T = 1.5$, which is at end downstroke, there is an identifiable spiralling LEV and a strong tip-vortex but neither of them generate much lift. At $t/T = 1.9$, which corresponds to the peak in VIL during late upstroke, the LEV on the ventral surface of the wing is relatively weak but the wing-tip vortex is seen to generate a noticeable contribution to lift.

By limiting the volume of integration to the region occupied by the LEV, we find for the hawkmoth wing that the LEV contributes (85%) percent of the total VIL at this instant, with the balance of the VIL coming from the other vortices. A similar analysis for selected instants during the flapping stroke shows that the LEV contributes 72% of the total lift over one stroke. Note that at this relatively high Reynolds number, the effect of viscous shear and dissipation (F_σ) on the lift is negligible.

For the fruit fly wing, which operates at a lower Reynolds number, the LEV is the most dominant vortical structure (see Fig. 4-7(d) and (f)) and it therefore follows that the LEV generates almost all of the vortex-induced lift. This is indeed borne out as seen in Fig. 4-2(b). During early downstroke (see Fig. 4-7(d)), the wing also generates an attached vortex on the trailing-edge of the wing (a TEV) and this vortex generates a negative lift contribution. Similarly, during late upstroke (Fig. 4-7(f)), there is an attached vortex on

dorsal wing-tip that produces a negative lift contribution. Furthermore, as noted earlier, viscous effect impart a sizeable (~ 25%) negative contribution to the net lift.

In addition to quantifying the role of the various vortices on lift production, our analysis reveals that the total added-mass force $F^i_{\kappa_I}$ also generates a sizeable net positive contribution to lift for both wings. For the hawkmoth wing, $F^i_{\kappa_I}$ contributes about 17% to the total net lift over one stroke where as for the fruit fly, the overall magnitudes are smaller, with $F^i_{\kappa_I}$ contributing about 10% to the net lift. The physical origin of the force associated with $F^i_{\kappa_I}$ is revealed by noting that the surface velocity can be decomposed as $\vec{U} = \vec{U}_\phi + \vec{U}_v$, where, as shown in Chapter 3, $\vec{U}_\phi$ and $\vec{U}_v$ are the flow velocities on the surface associated with the potential and viscous flow components respectively. $F^i_{\kappa_I}$ can therefore be decomposed as follows:

$$F^i_{\kappa_I} = -\rho \int_B \vec{n} \cdot \frac{d\vec{U}}{dt} \phi^{(i)} dS = \underbrace{-\rho \int_B \vec{n} \cdot \frac{d\vec{U}_\phi}{dt} \phi^{(i)} dS}_{F^i_{\kappa_i}} \underbrace{-\rho \int_B \vec{n} \cdot \frac{d\vec{U}_v}{dt} \phi^{(i)} dS}_{F^i_{\kappa_v}} \tag{4-3}$$

As shown in Chapter 3, the first term $F^i_{\kappa_i}$ on the right hand side of Eq. (4-3) is the classical invisid added-mass force that is experienced by a body accelerating in a potential flow. However, this inviscid added-mass cannot produce a net force on a body such as a flapping wing that is undergoing a periodic motion (see the next section in this Chapter). In Fig. 4-8 we show the time-variations of the two terms in $F^i_{\kappa_I}$ for the two wings and the stroke-average value of the inviscid added mass force $F^i_{\kappa_i}$ is indeed found to be negligible. It is the second term $F^i_{\kappa_v}$ in $F^i_{\kappa_I}$ that generates the non-zero net value for this force component. The similar form of the two terms on the right-hand-side of (4-3)

coupled with the fact that the second term appears only as a consequence of satisfying the no slip velocity boundary condition, suggests that this second term is a reaction to the acceleration of the flow tangential to the surface and may therefore be viewed as a "centripetal" added-mass force.

Thus, the current analysis shows that while the LEV contributes the dominant portion of the overall lift for hovering insects, there is another mechanism, what we term here as the centripetal added-mass force, that also contributes a significant portion of the net lift. This mechanism has a number of distinguishing features that are worth discussing. First, this mechanism is similar to the classical inviscid added-mass force in that it is an acceleration reaction, but is also different in that it requires the satisfaction of the no-slip condition. To our knowledge, this type of a force generation mechanism has never been identified before in the study of fluid-dynamics and certainly not in the context of flapping flight. The second interesting feature of this lift component is that the two noticeable positive peaks in $F_{\kappa_1}^{i}$ for the insects coincide with phases in the stroke where the vortex-induced lift is small or even negative. Thus, in addition to contributing to overall weight support, the centripetal added-mass lift also has the beneficial effect of reducing the time-variation in total lift.

In this context, it is interesting that positive added-mass lift is created even during the upstroke for both wings. We examine this further in Fig. 4-8(c-d) which shows the details of this force component at a few different phases in the flapping cycle for the two wings. Fig. 4-8(c) shows that for the hawkmoth, the centripetal added-mass lift peak during downstroke is generated from the region of the wing near the trailing-edge whereas the peak during upstroke is attributed to the wing-tip. For the fruit fly (Fig. 4-8(d)), the

situation is reversed, with the tip and the trailing-edge wings regions generating most of the added-mass lift during the down and upstrokes, respectively. The peak during upstroke occurs during the very early phase when the wing supinates and moves downward. During this time, the vectors corresponding to $d\vec{U}/dt$ and $-\hat{n}\left(\Delta\Phi^{(2)}\right)$ are pointing in similar directions so that their dot-product generates a positive (upward) lift force. We note that it is the large chordwise bending near the leading-edge hawkmoth that helps to produce a more noticeable downward motion during early downstroke, and this is responsible for generating a large positive local contribution to the centripetal added-mass force.

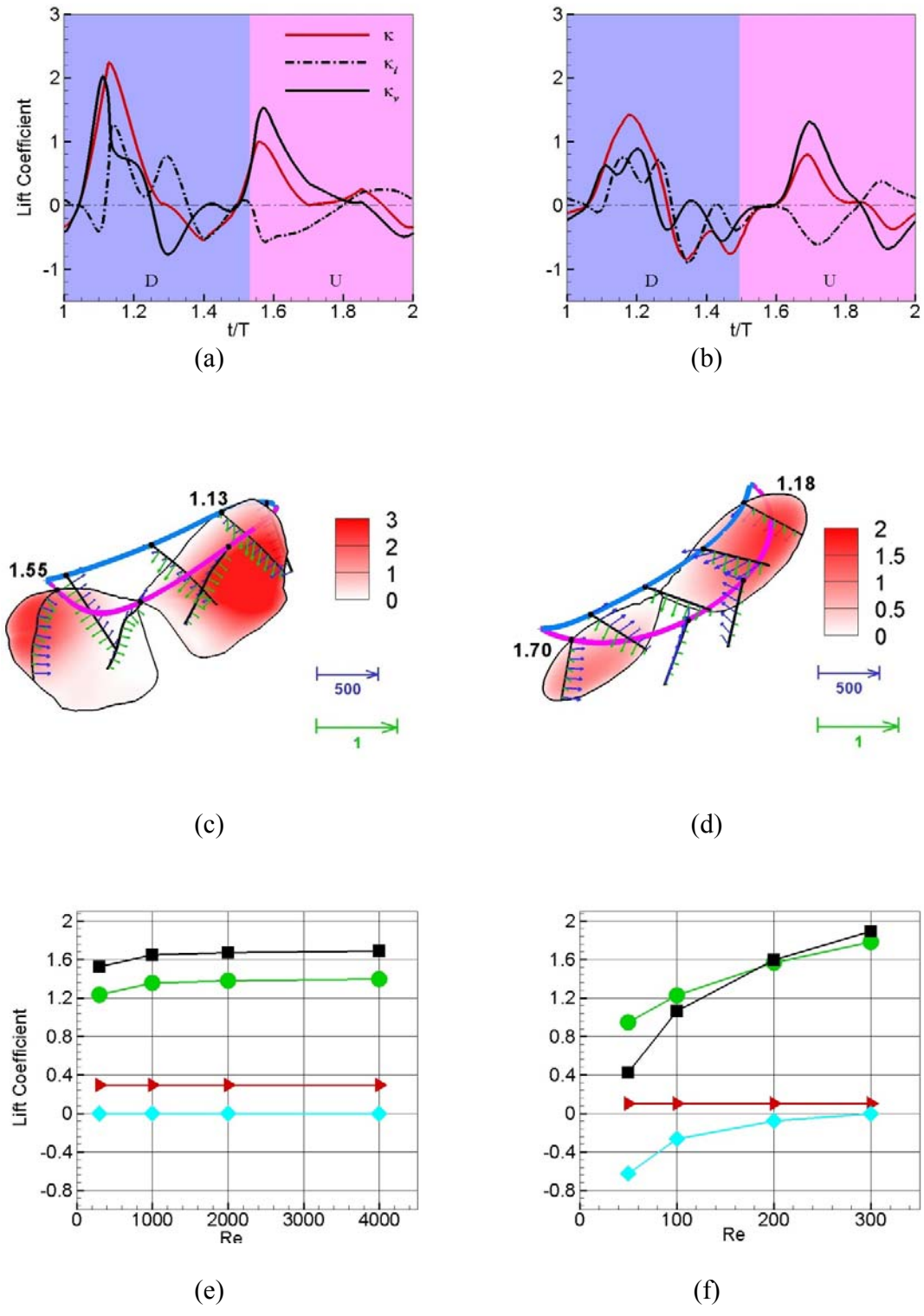

Figure 4-8 Time variation of the components of added mass lift $F_{\kappa}^{(2)}$ for the (a) hawkmoth and

(b) fruit fly over one flapping cycle. Surface contours of added-mass lift $F_{\kappa}^{(2)}$ at instants corresponding to peak values in the flapping cycle for the (c) hawkmoth and (d) fruit fly. Chord-lines at a few instances with black and green vectors corresponding to $D\vec{U}/Dt$ and $-\hat{n}\phi^{(2)}$ respectively where $\Delta\phi^{(2)}$ is the difference in scalar $\phi^{(2)}$ on the two sides of the wing, are also shown. Scaling of various components of lift with Reynolds numbers for the (e) hovering hawkmoth and (f) fruit fly. The black, green, red and cyan lines represent total, vortex-induced, added-mass and viscous components of lift, respectively.

A third distinguishing feature of the centripetal added-mass force is that while it is dependent on the satisfaction of the no-slip condition on the flapping wing, which necessitates a nonzero viscosity, the lift generated by this mechanism is independent of the actual magnitude of viscosity. From the viewpoint of hovering flight, this implies that for the same wing shape and wing kinematics, a change in the Reynolds number has no effect on the lift coefficient associated with the centripetal added-mass force. Figure 4-8(e-f), which shows the centripetal added-mass and vortex lift coefficients for the two wings over a range of Reynolds numbers confirms this assertion. The vortex-induced lift is found to decrease with Reynolds number for both cases, a trend that is very clear for the fruit fly, whereas the lift due to the total added mass F_{κ_I}, remains constant. In fact, at a Reynolds number of 50, the centripetal added-mass lift is 25% of the total lift and for the hawkmoth at Re=300, this number is 19%. This suggests that centripetal added-mass lift could be increasingly important for flight at the very small scales and it would therefore be very interesting to examine this mechanism for smaller insects such as thrips and parasatoid wasps.

The centripetal added-mass force also does not depend on the surrounding flow or vorticity field. This is important since it implies that insects flying in turbulent or otherwise disturbed airflows can rely on this mechanism of lift irrespective of the environmental conditions.

4.4.2. Power Consumption Associated with Different Lift Components

Finally, generation of lift requires expenditure of power by the animal and it is therefore of interest to examine the power consumed by each component of lift. The power expenditure associated with each component of force partitioned using FPM can be computed as the surface integral of the dot product of force component with the surface velocity; thus for instance, the instantaneous power associated with the total added mass force F_κ is given by $P_\kappa = \int_B U_i F_\kappa^{(i)} dS$, and similarly for other force components. Note that this requires the computations of all three vector components of each partitioned component of the force. Fig. 4-9 shows the time-variation of the coefficient of power, defined as $C_{\bar{p}} = \bar{p} / \rho A \beta^3 f^3 L^3$, for the total force as well as F_κ , F_ω and F_σ. Table 4-1 shows the coefficient of cycle-averaged power for the three primary components. The 17.3% and 9.5% contributions of centripetal added-mass to the lift of the hawkmoth and the fruit fly, respectively, are generated with less than 1% of the total power consumption. Examination of the time-varying power coefficient (shown in Fig. 4-9) reveals that unlike the vortex and viscosity induced components of lift, which consume power during all phases of the stroke, much of the power consumed by the insect to generate the centripetal added-mass component of lift at the initial phases of

downstroke and upstroke, is recovered during the deceleration phase in the latter halves of each half-stroke. Thus, even though the centripetal added-mass lift is not the dominant component, it is significantly more power-efficient than the dominant vortex-induced component of lift. In other words, if the percentage of added mass increases, the power efficiency will probably increases consequently.

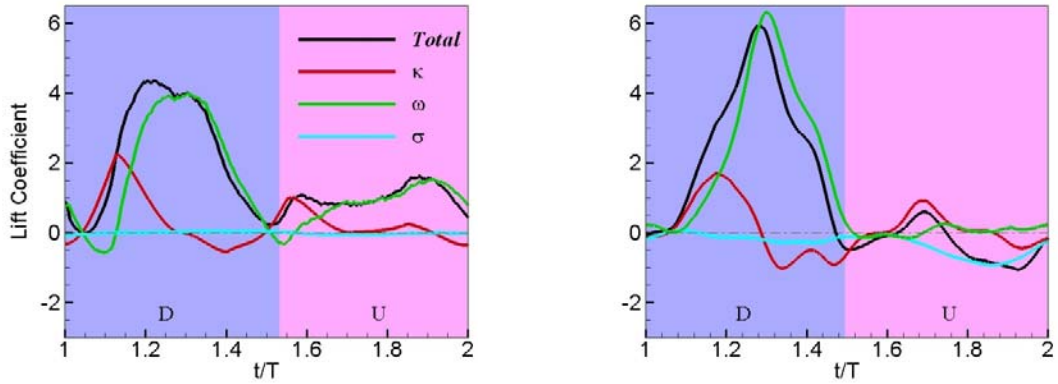

Figure 4-9 Time series of power coefficient in components (a) Hovering Hawkmoth flight at Re=1000 and (b) Hovering Fruit fly flight at Re=100 throughout a full stroke cycle, which is subdivided into two stages: Downstroke (D) and Upstroke (U). The black line represents the total power consumption; The red line is the power consumed by total added mass force; The green line represents the power consumed by vortex induced force; The cyan line shows power consumption by viscous force.

In order to validate the correlation of percentage of added mass component with the power efficiency, we carried out a set five simulations with various combinations of hawkmoth wing shape and kinematics and with fruit-fly wing shape kinematics. All the different wings were uniformly scaled with a same wing span length ($L = 41mm$) and all

numerical simulations are conducted at the same Reynolds number (Re = 300) so that the viscous effect can be neglected (<1%). The flapping frequency is also fixed to be 25Hz for all the five cases. As shown in Table 4-2, firstly comparing real flexible hawkmoth wing (case 1) and solid hawkmoth wing with hawkmoth wing kinematics (case 2), we see that the magnitudes of total added mass lift in both cases are quantitatively comparable whereas the solid hawkmoth wing generates less vortex-induced lift but with a higher power efficiency than real flexible hakwmoth wing. Moreover, if we sort the all five cases according to the power loading, which is defined as the ratio of total lift to the total power consumption, along with the percentage of total added mass lift, we clearly see that they are in the same order (2>1>5>3>4). It implies that the higher percentage of total added mass will increase the power efficiency to generate the same amount of lift.

Table 4-2 Performance of 5 Different Wing Shape and Kinematics (Re=300, Flapping Frequency=25, Wing span=41mm). Index 1 denotes real flexible hawkmoth wing; 2 denotes solid hawkmoth wing with hawkmoth wing kinematics; 3 denotes solid hawkmoth wing with fruit-fly wing kinematics; 4 denotes solid fruit-fly wing with fruit-fly wing kinematics; 5 denotes solid fruit-fly wing with hawkmoth wing kinematics.

Index	Total Lift(mN)	AM Lift		Vortex-Induced		Power Loading(N/W)
		Value(mN)	Percent	Value(mN)	Percent	
1	4.81	0.94	19.5%	3.86	80.2%	0.219
2	3.53	1.06	30.0%	2.43	68.8%	0.231
3	6.91	1.11	16.1%	5.78	83.6%	0.181
4	1.00	074	7.3%	9.24	92.4%	0.162
5	4.83	0.87	18.0%	3.93	81.3%	0.213

4.5. Conclusion

In summary, the FPM methodology developed here leads to a mathematically unambiguous and physically insightful partitioning of the fluid-dynamic forces experienced by a body immersed in a fluid. By using FPM, we have precisely quantified the contribution of the leading-edge vortex to lift production for two distinct insect flyers, the hawkmoth and the fruit fly. The analysis has also identified a new mechanism, what we call the centripetal added-mass force that contributes a significant component to the total lift. This mechanism, which is connected solely with the wing-kinematics, is independent of the Reynolds number and environmental flow disturbances, and requires little power. It therefore provides an efficient and robust mechanism for weight support at all scales.

While the focus of the current paper is on insect flight, FPM has wide ranging applications to virtually all fields of fluid dynamics, and in particular, to vortex dominated flows and flows with dynamically moving bodies. Similarly, the mechanism of centripetal added-mass force that has been identified here likely plays an important role in flows that involve bodies undergoing complex motions such as those encountered in the flying and swimming of animals, flow induced vibration and deformation in biology and engineering, and multiphase flows.

CHAPTER 5. STABILITY ANALYSIS OF HOVERING FLIGHT OF A HAWKMOTH

5.1. Introduction

In addition to generating forces sufficient for supporting the weight of the insect (or flying vehicle), flight stability is also a necessary condition for sustained hovering flight. While the ultimate objective of the current study is to understand the stabilization of hovering insects in the face of large-scale aerodynamic perturbations, a precursor to this is to examine the intrinsic (in the absence of large perturbation) flight stability of hovering insects.

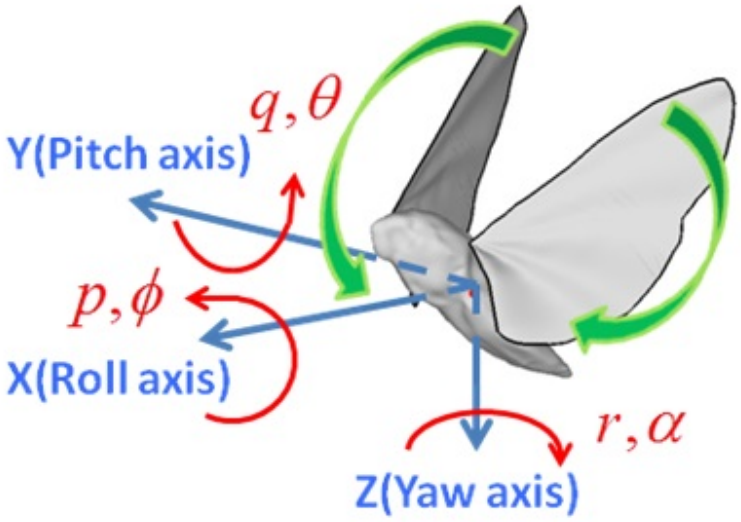

Figure 5-1 Schematic of Six Degree of Freedom (6DoF) motion in body-fixed frame.

Figure 5-1 defines the various degrees of freedom for a flying insect and the following questions come to mind regarding the stability of hovering flight of insects:

(a) What method/models are appropriate for examining the stability of hovering flight in insects and insect-inspired micro aerial vehicles? The vast majority of previous

stability analyses (Taylor, et al, 2003; Sun, et al, 2005) employ linearized analysis around a time-invariant (the so called linear time-invariant (LTI) base state that is assumed to represent the time-averaged state of the insect. Such an analysis assumes that the time-variations in the base state are "small" and/or the time-scales of the base state are sufficiently separated from the natural instability time-scales of the "vehicle" in question. This might be true for a revolving wing vehicle (where the time-variation in generated forces are negligible) or for insects such as mosquitoes, wasps and fruitflies that flap their wing at very high (>100Hz) frequencies. However, LTI modeling might not necessarily serve as an appropriate model for large insects such as hawkmoths, butterflies and beetles. These animals have a lower flapping frequency (~20Hz) and the large time-varying forces produced by the wings of these insects may induce significant oscillations in their body position and posture during hovering. In the face of this, it might be appropriate to adopt stability models such as Floquet models (Floquet, 1883) that allow for time-periodic based states. However, such stability models are considerably more complex than LTI models and implementation of these models for a flying insect is highly non-trivial.

(b) Is hovering flight in insects stable or does it require active stabilization? This is the fundamental question that needs to be answered. A number of studies of the flight stability of hovering insects have been conducted but the results are not consistent. For example, G. K. Taylor and A. L. R. Thomas has investigated the longitudinal stability of locust and found one unstable mode out of four longitudinal motion modes. In their linearized model, all related quantities are measured from the experiments. Afterwards, the same model was also conducted by M. Sun and his colleagues in 2005 via CFD

simulation to study the longitudinal stability of bumblebees. However they found two unstable conjugate modes among the four motion modes.

(c) If hovering flight is indeed unstable, what are the dominant modes of instability? Due to the bilateral body symmetry of insects, it has generally been assumed that longitudinal stability modes are most critical. This assumption coupled with the bilateral symmetry allows the use of stability models that are limited to the longitudinal stability modes (i.e. three-degree-of-freedom or 3DOF) and most studies in the past have employed such 3DOF models (Taylor, et al, 2003; Sun, et al, 2005). However, it is not clear if cross-coupling between various degrees of freedom could introduce additional complexities in the stability of these insects. Analysis of such complexities requires six-degree of freedom (6DOF) models but implementing such models for a complex configuration such as a flapping insect is highly time-consuming.

(d) What are the key differences in the hovering stability of flapping wing versus rotating wing MAVs? This question has practical importance since MAVs capable of hovering either employ flapping or revolving wings. In particular, does the bilateral symmetry of the flapping wings provide some inherent benefits for hover stabilizations?

All of the issues and questions raised above are addresses in the current chapter. The model organism employed in the current study is the Hawkmoth which is described in the earlier chapters. To reiterate, this is a large insect with wing span of about 10 cm and body mass of 1.6 grams and it flaps its wings at a frequency of about 25 Hz. As shown in Fig. 5.2, during hover, this insect undergoes small, but noticeable oscillations in the location of its center-of-mass during flapping flight.

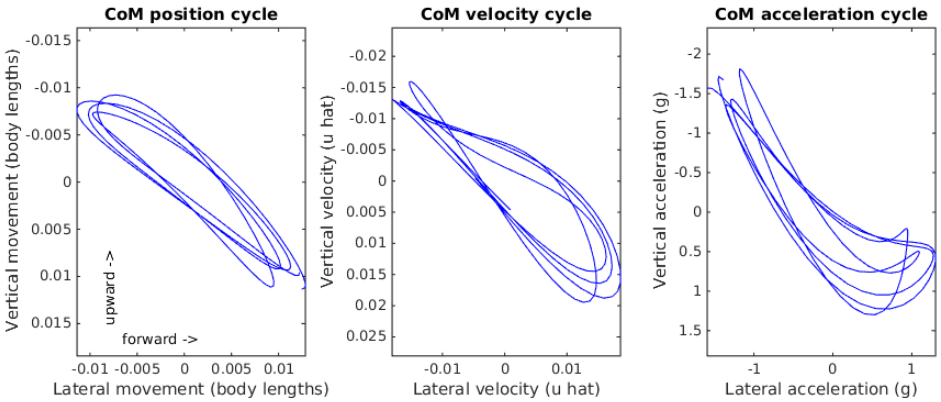

Figure 5-2 Experimental measurement of the cyclical motion of the center-of-mass of the moth during normal hover. Measurements have been communicated by Tyson Hedrick (UNC Chapel Hill).

The current analysis begins with a LTI model for a 3DOF system and this is followed by a first-of-its-kind, 6DOF stability analysis of a hovering hawkmoth. A revolving wing-hawkmoth model is also synthesized to provide direct comparison of the stability of flapping and revolving wing configurations. Finally, we employ a linear-time- periodic (LTP) model for the stability analysis of the hovering hawmoth and compare it to the LTI models. Based on all of these analyses, insights regarding the linear stability of a hovering hawkmoth are presented.

5.2. Linear Time Invariant (LTI) Model

The LTI model assumes a time-invariant equilibrium (base) state and examines the linearized equations for a small disturbance about the equilibrium state. The vast majority of insect flight stability analyses have employed this method (Taylor, et al, 2003; Sun, et al, 2005; Gao, et al, 2010) and the analysis has been applied to hovering flight of fruitflies, hoverflies, bumblebees and even the hawkmoth. The general conclusion of

these analyses is that all these insects are dynamically unstable (i.e. they exhibit an oscillatory unstable mode) in the longitudinal plane. However, with regard to the hawkmoth, the accuracy of this analysis depends on the fidelity with which the wing stroke kinematics are represented and in the past analyses of the hawkmoth stability (Sun et al., 2007), the wing kinematics that were employed were highly simplified. In the current work, we conduct stability analysis that is based on wing kinematics of the hawkmoth that include the observed wing deformation. Past studies (Zheng et al., 2013) have verified that CFD models based on these wing kinematics lead to a fairly accurate reproduction of the time-profile of forces on the wing.

5.2.1. Longitudinal (3DOF) Stability Analysis

In Fig 5-3, the schematic shows the body frame for a hovering hawkmoth defined by OXZ coordinates. The origin O is the center-of-mass of the hawkmoth; axis X pointing in the forward direction whereas axis Z points downwards in this frame. The longitudinal motion is defined by four variables: forward (u) and dorso-ventral (w) components of velocity along X and Z axes respectively, the angular velocity in pitch around the center of mass (q), and the pitch angle between the X axis and the lab-fixed horizontal line (θ). The X and Z components of the total aerodynamic force are denoted as F^X and F^Z, respectively, and the aerodynamic pitching moment is represented as M^Y; The total mass of the hawkmoth, the gravitational acceleration and the momentof-inertia of pitch motion denoted as m, g and I respectively. Newton's law in this frame can now be written as:

$$\frac{du}{dt} = -wq + \frac{F^X}{m} - g\sin\theta \tag{5-1a}$$

$$\frac{dw}{dt} = -uq + \frac{F^Z}{m} + g\cos\theta \tag{5-1b}$$

$$\frac{dq}{dt} = \frac{M^Y}{I} \tag{5-1c}$$

$$\frac{d\theta}{dt} = q \tag{5-1d}$$

where m and g denote the total mass and gravity; And in Eq. (5-1a) & (5-1b), the nonlinear cross terms wq and uq are Coriolis forces due to the pitching motion. In the model above, we assume that all the variables involved in the equations are time invariant throughout the flapping cycle. And they can be obtained via cycle-averaging calculation.

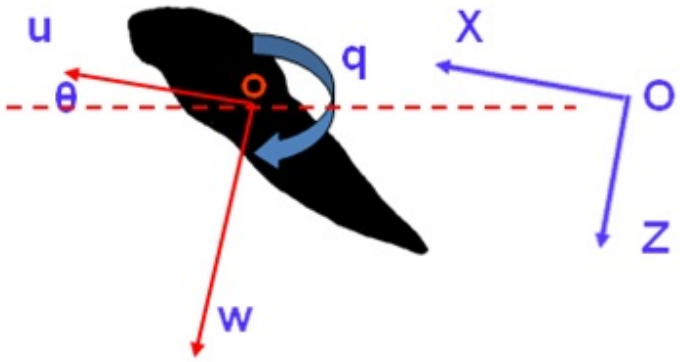

Figure 5-3 Schematic of longitudinal motion in body-fixed frame.

Eq. 5-1 is subsequently linearized about the base-state as $(u,w,q,\theta)=(\underline{u},\underline{w},\underline{q},\underline{\theta})\pm(\delta u,\delta w,\delta q,\delta\theta)$, where $(\underline{u},\underline{w},\underline{q},\underline{\theta})$ represents the time-invariant base (or equilibrium) state and $(\delta u,\delta w,\delta q,\delta\theta)$ is the small perturbation about equilibrium. Eq. 5-1a can be written as

$$\frac{d(\underline{u}+\delta u)}{dt}=-(\underline{w}+\delta w)(\underline{q}+\delta q)+\frac{F^X+\delta F^X}{m}-g\sin(\underline{\theta}+\delta\theta) \tag{5-2}$$

Neglecting the quadratic and higher order terms in the above equation and assuming the base variable for LTI model is all zero lead to the following equation

$$\frac{d\delta u}{dt}=-\delta w\delta q+\frac{\delta F^X}{m}-g \tag{5-3}$$

Here we also assume that all the forces and moments can be estimated by 1st order Taylor series expansion,

$$\delta F^X=F_u^X\delta u+F_w^X\delta w+F_q^X\delta q \tag{5-4a}$$

$$\delta F^Z=F_u^Z\delta u+F_w^Z\delta w+F_q^Z\delta q \tag{5-4b}$$

$$\delta M^Y=M_u^Y\delta u+M_w^Y\delta w+M_q^Y\delta q \tag{5-4c}$$

where the subscripts below F^X , F^Z and M^Y represent the partial derivatives with respect to u , w and q respectively. A similar procedure applied to the other equations in 5-1 leads to the following set of equations for the perturbation:

$$\dot{U} = AU$$

$$A = \begin{bmatrix} \frac{F_u^X}{m} & \frac{F_w^X}{m} & \frac{F_q^X}{m} & -g \\ \frac{F_u^Z}{m} & \frac{F_w^Z}{m} & \frac{F_q^Z}{m} & 0 \\ \frac{M_u^Y}{I} & \frac{M_w^Y}{I} & \frac{M_q^Y}{I} & 0 \\ 0 & 0 & 1 & 0 \end{bmatrix}, U = \begin{bmatrix} \delta u \\ \delta w \\ \delta q \\ \delta \theta \end{bmatrix} \quad (5\text{-}5)$$

Assumption of an exponential solution in time for the perturbation transforms the above system into an eigenvalue problem and the eigenvalue spectrum of the 4x4 matrix *A* determines the LTI stability of the system. Note that each eigenvalue can be real or complex (complex eigenvalues appear as pairs of complex conjugates) with the real part of the eigenvalue signifying growth (instability) or decay (stability) depending on whether it is positive or negative, respectively. A complex eigenvalue denotes a time-periodic mode with the imaginary part of the eigenvalue denoting the frequency of the periodic mode.

Thus, in order to determine the stability, the elements of matrix *A* need to be estimated. The mass (*m*) and pitch moment of inertia (*I*) is available from experimental data provided by Tyson Hedrick (Private communication) and these values are estimated to be $1.63\times10^{-3} kg$ and $4.23\times10^{-7} kgm^2$ respectively. Furthermore, acceleration due to gravity is also known (g= $9.8 N/kg$). Only the sensitivities of the forces and moments to the kinematic variables need to be determined and we employ the following procedure to obtain these values:

a) A base-state of hovering flight in the hawkmoth is assumed based on experimental observations. This state has been examined in detail in the past by Zheng et al. (2013a and 2013b). These simulations are carried out at a Reynolds

number of 400 on a local refined $128\times128\times128$ grid and Fig. 5-1 shows the forces and pitching moment for this configuration.

b) For each of the variables (u,w,q) we also compute two additional states by perturbing the particular variable. For instance, for, variable u, solutions are also computed by imposing a perturbed forward flow velocity of $\delta u = \pm 0.01 m/s$ over the moth. Cycle averaged forces and moments for these two conditions are computed and the derivative F_u^X estimated by employing a central-difference scheme as $F_u^X = \dfrac{F^X(u+\delta u,w,q) - F^X(u-\delta u,w,q)}{2\delta u}$. The other derivatives F_u^Z and M_u^Y are also computed in a similar manner. For w, we assume perturbed values of $\delta w = \pm 0.01 m/s$ and for q the values employed are $\delta q = \pm 0.01 rad/s$. Since the frame is fixed to the body, so all the forces and moment are irrelevant to the pitch angle θ. Subsequently, the derivative of the forces and moment w.r.t. these two variables are also estimated as described above. Thus, a total of 6 simulations (in addition to the base-state) were computed in order to obtain all the elements in the matrix.

Table 5-1 Cycle-averaged aerodynamics derivatives

F_u^X (Ns/m)	F_u^Z (Ns/m)	M_u^Y (Ns)	F_w^X (Ns/m)	F_w^Z (Ns/m)	M_w^Y (Ns)	F_q^X (Ns)	F_q^Z (Ns)	M_q^Y (Nms)
−5.28 $\times10^{-3}$	−0.99 $\times10^{-3}$	0.22 $\times10^{-3}$	−0.66 $\times10^{-3}$	−3.33 $\times10^{-3}$	0.10 $\times10^{-3}$	−0.27 $\times10^{-3}$	−0.01 $\times10^{-3}$	−2.28 $\times10^{-6}$

Once the elements of the matrix are available, it is a simple matter to obtain the eigenvalues of the 4x4 system.

Table 5-2 Eigenvalues and Eigenvectors of longitudinal LTI system matrix

Mode	1	2	3
Eigenvalues	-18.34	$4.66 \pm 16.06i$	-1.82
Eigenvectors			
δu	-12.22	$-6.11 \pm 7.58i$	0.00
δw	-5.42	$-2.74 \pm 3.63i$	1.10
δq	0.34	$-0.33 \mp 0.07i$	0.00
$\delta\theta$	-6.53	$-3.27 \mp 4.68i$	0.00

The calculated eigenvalues for this case appear as three distinct modes, with one pair of complex conjugates and two negative real ones as presented in Table 5-2. The two modes with real eigenvalues are both stable "subsistence" modes, with mode-1 being the fast and mode-3 the slow subsistence mode. The mode with the complex eigenvalue is unstable since it has a positive real part, which indicates the initial perturbation in this mode will increase with time. In order to measure the growth of the instability, the parameter of doubling-time t_{double} is introduced, which is the time taken to double the perturbation of the system. t_{double} is related to the real part of eigenvalue by the following expression:

$$t_{double} = \ln(2) / R \tag{5-6}$$

where R is either the magnitude of the real eigenvalue or the magnitude of the real part of the complex eigenvalue. Based on the eigenvalue in Table 5-2, the t_{double} for the unstable mode is $3.7T$ (T is the flapping cycle of hawkmoth, which is about 0.04 second); this corresponds to a fairly strong instability that essentially doubles in amplitude with every 3.7 flapping cycles.

The nature of this instability can be determined by analyzing the eigenmode corresponding to this eigenvalue. In this context proper normalization of each eigenmode component is required since each component has different dimensions. Here we calculate the normalized magnitudes of the eigenvector components by dividing by the corresponding characteristic variables as follow:

$$\begin{aligned} |\delta u|^{+} &= |\delta u| / n\Phi L, |\delta w|^{+} = |\delta w| / n\Phi L \\ |\delta q|^{+} &= |\delta q| / n\Phi, \quad |\delta\theta|^{+} = |\delta\theta| / \Phi \end{aligned} \tag{5-7}$$

where superscript "$+$" denotes the normalized magnitude and n, Φ and L represent the stroke frequency, stroke amplitude and wing length respectively. In this study, all characteristic properties are measured from the data for an actual hawkmoth ($n = 25Hz$, $\Phi = 1.56rad$, $L = 0.042m$) and used for the normalization and the normalized magnitudes of the eigenmode components are given in the table below:

Table 5-3 Normalized magnitude of eigenvector components in mode 1

Mode	$\lvert\delta u\rvert^{+}$	$\lvert\delta w\rvert^{+}$	$\lvert\delta q\rvert^{+}$	$\lvert\delta\theta\rvert^{+}$
Normalized Magnitude	5.95	2.78	0.01	3.66

Table 5-3 indicates that the unstable mode primarily consists of translational velocities δu, δw and pitch angle $\delta\theta$. According to the eigenvector of the unstable mode in Table 5-2, we also notice that the vertical velocity perturbation δw and the pitch angle perturbation $\delta\theta$ perform a high frequency oscillation while the horizontal velocity u is in low frequency oscillation in the unstable mode. Overall, the 3DOF LTI analysis gives results that are consistent with those by Wu (2009) who employed rigid wing kinematics for the hawkmoth.

5.2.2. Six Degrees of Freedom Linear Time Invariant (6DoF LTI) Stability Analysis

Although the bilateral symmetry of insect bodies suggests that the longitudinal stability should dictate the overall stability, this assumption has never been verified rigorously. Gao et al. (2011) used 6DoF fully coupled fluid-body interaction solver to predict the passive response of hovering fruit-fly to the different perturbations in all modes. They eventually found that fruit-fly is more sensitive to lateral perturbation rather than longitudinal ones and rotational perturbation is more crucial than translational perturbation in the flight stability. In order to assess the results of the longitudinal stability analysis as well as to eventually conduct the comparison with the revolving wing configuration, we have also conducted a six-degree of freedom (6DoF) stability analysis by using the LTI approach. This allows us to test the validity of longitudinal stability assumption, which has been widely used by many researchers (Taylor et al., 2003; Sun et al. 2005).

Similar to the 3DoF analysis, the body-fixed frame is also used in this study as shown in Fig. 5-3. The equations of motion shown below involve three translational velocities, three rotational velocities and three characteristic angles as system variables.

$$
\begin{cases}
\dot{u} = qw - rv + \dfrac{F^X}{m} - g\sin\theta \\
\dot{v} = ru - pw + \dfrac{F^Y}{m} - g\sin\phi \\
\dot{w} = pv - qu + \dfrac{F^Z}{m} - g\cos\left(\sqrt{\theta^2 + \phi^2}\right) \\
\dot{p} = \dfrac{-\left(I_r - I_q\right)qr + M^X}{I_p} \\
\dot{r} = \dfrac{-\left(I_p - I_r\right)qp + M^Z}{I_q} \\
\dot{q} = \dfrac{-\left(I_q - I_p\right)pr + M^Y}{I_r} \\
\dot{\theta} = q + p\sin\phi\tan\theta + r\cos\phi\tan\theta \\
\dot{\alpha} = r + p\sin\phi\tan\theta + q\cos\phi\tan\theta \\
\dot{\phi} = p + r\sin\phi\tan\theta + q\cos\phi\tan\theta
\end{cases}
\tag{5-8}
$$

where u, v and w denote the translational velocities in X, Y and Z axis respectively; p, q and r denote roll, pitch and yaw velocities and ϕ, θ and α are roll, pitch and yaw angle, respectively; M^X, M^Y and M^Z denote three components of total moment associated with roll, pitch and yaw respectively; I_p, I_q and I_r represent the leading diagonal elements in the moment of inertia tensor.

The 6DoF equations of motion (Eq. (5-8)) can also be linearized via the same approach of adding small perturbations to system variables as described before. The linearization of the resulting perturbation leads to the following 9×9 time invariant matrix as shown in Eq. (5-9).

$$\dot{U} = AU$$

$$A = \begin{bmatrix} \frac{F_u^X}{m} & \frac{F_v^X}{m} & \frac{F_w^X}{m} & \frac{F_p^X}{m} & \frac{F_r^X}{m} & \frac{F_q^X}{m} & 0 & 0 & -g \\ \frac{F_u^Y}{m} & \frac{F_v^Y}{m} & \frac{F_w^Y}{m} & \frac{F_p^Y}{m} & \frac{F_r^Y}{m} & \frac{F_q^Y}{m} & -g & 0 & 0 \\ \frac{F_u^Z}{m} & \frac{F_v^Z}{m} & \frac{F_w^Z}{m} & \frac{F_p^Z}{m} & \frac{F_r^Z}{m} & \frac{F_q^Z}{m} & 0 & 0 & 0 \\ \frac{M_u^X}{I_{xx}} & \frac{M_v^X}{I_{xx}} & \frac{M_w^X}{I_{xx}} & \frac{M_p^X}{I_{xx}} & \frac{M_r^X}{I_{xx}} & \frac{M_q^X}{I_{xx}} & 0 & 0 & 0 \\ \frac{M_u^Y}{I_{yy}} & \frac{M_v^Y}{I_{yy}} & \frac{M_w^Y}{I_{yy}} & \frac{M_p^Y}{I_{yy}} & \frac{M_r^Y}{I_{yy}} & \frac{M_q^Y}{I_{yy}} & 0 & 0 & 0 \\ \frac{M_u^Z}{I_{zz}} & \frac{M_v^Z}{I_{zz}} & \frac{M_w^Z}{I_{zz}} & \frac{M_p^Z}{I_{zz}} & \frac{M_r^Z}{I_{zz}} & \frac{M_q^Z}{I_{zz}} & 0 & 0 & 0 \\ 0 & 0 & 0 & 1 & 0 & 0 & 0 & 0 & 0 \\ 0 & 0 & 0 & 0 & 1 & 0 & 0 & 0 & 0 \\ 0 & 0 & 0 & 0 & 0 & 1 & 0 & 0 & 0 \end{bmatrix}, U = \begin{bmatrix} \delta u \\ \delta v \\ \delta w \\ \delta p \\ \delta r \\ \delta q \\ \delta \phi \\ \delta \alpha \\ \delta \theta \end{bmatrix} \tag{5-9}$$

The aerodynamic derivatives in the matrix are computed by conducting 12 separate simulations and this leads to the following values for the A matrix:

$$A = \begin{bmatrix} -3.345 & 0.056 & -0.417 & 0.003 & -0.000 & -0.174 & 0 & 0 & -9.8 \\ -0.057 & -1.890 & 0.022 & 0.098 & 0.007 & 0.001 & -9.8 & 0 & 0 \\ -0.630 & 0.016 & -2.114 & 0.002 & 0.001 & -0.005 & 0 & 0 & 0 \\ 28.99 & -153.8 & -14.23 & -29.38 & 11.40 & -1.809 & 0 & 0 & 0 \\ 19.45 & 88.76 & -3.121 & 13.34 & -0.088 & -1.271 & 0 & 0 & 0 \\ 523.6 & -252.3 & -240.96 & -10.52 & -9.980 & -5.386 & 0 & 0 & 0 \\ 0 & 0 & 0 & 1 & 0 & 0 & 0 & 0 & 0 \\ 0 & 0 & 0 & 0 & 1 & 0 & 0 & 0 & 0 \\ 0 & 0 & 0 & 0 & 0 & 1 & 0 & 0 & 0 \end{bmatrix}$$

The eigenvalue and eigenvectors of the 9x9 system are calculated in MATLAB and the results are shown in the Table below. Seven different modes emerge from this analysis: 5 stable real modes and 2 unstable complex modes. Mode 1 and mode 2 have the same real part of the eigenvalue (which corresponds to $t_{double} = 3.68T$) and these two modes are therefore equally unstable.

Table 5-4 Eigenvalues of 6DoF LTI system matrix

Mode	1	2	3	4	5	6	7
Eigenvalues	$4.7 \pm 16.6i$	$4.7 \pm 1.2i$	0.0	–1.7	–9.9	–17.8	–31.5

In Table 5-5, we have shown the eigenmodes associated with these two unstable modes. By examining the normalized magnitude of eigenvector in mode 1, we find that the dominant eigen-motion is identified by variables that lie in the longitudinal plane (horizontal velocity δu, vertical velocity δw, pitch angle $\delta\theta$, lateral velocity δv and roll angle $\delta\phi$), which is similar to the mode identified in the longitudinal stability analysis, although it is also coupled with the lateral degrees of freedom defined by δv and $\delta\phi$. In fact, we see that modes 1, 4 and 6 essentially represent the stability in the longitudinal plane. However the other unstable mode, mode-2 has no counterpart in the longitudinal plane and is dominated by rolling (ϕ) and sideways (v) motion. This indicates that the flight stability of a hovering hawkmoth is not only determined by longitudinal (pitching) instability, but that there exists a lateral instability mode that is equally strong also includes some degrees of freedom from the longitudinal plane. We

note that a similar observation has been made by Gao, et al, (2011) in their 6DoF analysis of a hovering fruit-fly.

Table 5-5 Eigen-motion of 6DoF LTI system matrix in the unstable modes (1 & 2)

	δu	δv	δw	δp	δr	δq	$\delta\phi$	$\delta\alpha$	$\delta\theta$
Component (Mode 1)	6.0± 7.8*i*	2.1± 3.4*i*	2.9± 3.4*i*	0.1± 0.1*i*	0.1± 0.1*i*	0.3± 0.1*i*	1.5± 1.6*i*	0.0	3.3± 4.5*i*
Normalized Magnitude (Mode 1)	6.0	2.4	2.7	0.0	0.0	0.0	1.4	0.0	3.6
Component (Mode 2)	–0.4± 0.1*i*	1.4± 2.9*i*	0.5± 0.1*i*	0.2± 0.1*i*	0.5± 0.0*i*	–0.0± 0.0*i*	0.2± 5.1*i*	0.0	0.6± 0.1*i*
Normalized Magnitude (Mode 2)	0.3	2.0	0.3	0.0	0.0	0.0	3.3	0.0	0.4

5.2.3. Stability Analysis of Hawkmoth with Artificial Revolving Wings

The question about the relative efficiency (in terms of power loading or other similar variable) of flight with flapping versus revolving wings has been addressed in many previous studies (Weis-Fogh, 1973; Dickinson, et al, 1999; Zheng, et al, 2013). However the one question that has never been directly addressed is the advantage (or disadvantage) of one configuration versus the other viz-a-viz the stability of hovering flight. In the context of design of a MAV, a configuration that is more unstable or exhibits a larger number of instability modes, would require complex control mechanisms and might therefore be less desirable. In this section, we conduct a 6DoF LTI analysis of a

synthesized “revolving wing hawkmoth” which provides some insight into the above question.

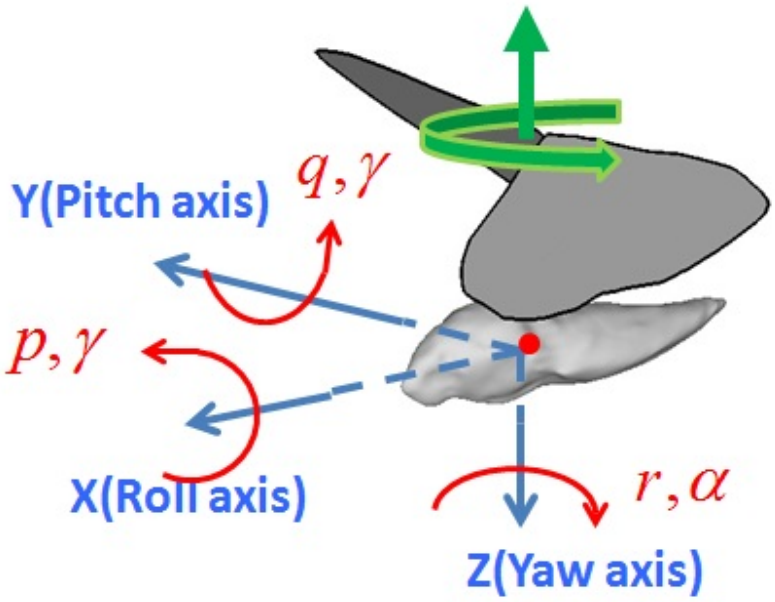

Figure 5-4 Schematic of Six Degree of Freedom (6DoF) motion of hawkmoth with revolving wings.

The revolving wing configuration is conceptually assembled by mounting a pair of moth-wing shape flat plates on top of the hawkmoth body (see Fig. 5-4). In order reproduce the same amount of mean lift generated by flapping wing model, the pitch angle of the wings was set to 45 degrees and the rotational velocity is set to be $157.1 rad/s$. Furthermore, the rotational axis of the revolving wing is exactly aligned with the location of the CoM so that the equilibrium condition for hovering is easily achieved. Unlike the bilateral symmetry of flapping wing model, the time-invariant equilibrium condition for the revolving wing model is more like an axi-symmetrical model so that only tilt angle between stroke plane and horizontal plane θ and roll angle Φ should be considered (as shown in Fig. 5-4). Moreover, the revolving wings bilateral

anti-symmetry; for example, even if a bilaterally symmetrical perturbation such as a horizontal velocity perturbation is given, a pair of unequal induced lift and drag forces are generated by the two 'rotor blades', which lead to an unbalanced roll torque and rolling motion. Therefore, the revolving wing hawkmoth has an intrinsic coupling between the longitudinal and lateral degrees of freedom and this configuration therefore requires a full 6DoF analysis. The equations of motion and the corresponding linearized ODEs for revolving wings model are shown as Eq. (5-10) & (5-11).

$$\begin{cases} \dot{u} = qw - rv + \dfrac{F^X}{m} - g\sin\gamma \\ \dot{v} = ru - pw + \dfrac{F^Y}{m} + g\cos\gamma\cos\phi \\ \dot{w} = pv - qu + \dfrac{F^Z}{m} - g\cos\gamma\sin\phi \\ \dot{p} = \dfrac{-\left(I_r - I_q\right)qr + M^X}{I_p} \\ \dot{r} = \dfrac{-\left(I_p - I_r\right)qp + M^Y}{I_q} \\ \dot{q} = \dfrac{-\left(I_q - I_p\right)pr + M^Z}{I_r} \\ \dot{\alpha} = r + p\sin\alpha\tan\gamma + q\cos\alpha\tan\gamma \\ \dot{\gamma} = p\cos\alpha - q\sin\alpha \end{cases} \tag{5-10}$$

$$\dot{U} = AU$$

$$A = \begin{bmatrix} \frac{F_u^X X_u}{m} & \frac{F_v^X X_v}{m} & \frac{F_w^X X_w}{m} & \frac{F_p^X X_p}{m} & \frac{F_r^X X_r}{m} & \frac{F_q^X X_q}{m} & 0 & -g \\ \frac{F_u^Y Y_u}{m} & \frac{F_v^Y Y_v}{m} & \frac{F_w^Y Y_w}{m} & \frac{F_p^Y Y_p}{m} & \frac{F_r^Y Y_r}{m} & \frac{F_q^Y Y_q}{m} & 0 & 0 \\ \frac{F_u^Z Z_u}{m} & \frac{F_v^Z Z_v}{m} & \frac{F_w^Z Z_w}{m} & \frac{F_p^Z Z_p}{m} & \frac{F_r^Z Z_r}{m} & \frac{F_q^Z Z_q}{m} & -g & 0 \\ \frac{M_u^X}{I_{xx}} & \frac{M_v^X}{I_{xx}} & \frac{M_w^X}{I_{xx}} & \frac{M_p^X}{I_{xx}} & \frac{M_r^X}{I_{xx}} & \frac{M_q^X}{I_{xx}} & 0 & 0 \\ \frac{M_u^Y}{I_{yy}} & \frac{M_v^Y}{I_{yy}} & \frac{M_w^Y}{I_{yy}} & \frac{M_p^Y}{I_{yy}} & \frac{M_r^Y}{I_{yy}} & \frac{M_q^Y}{I_{yy}} & 0 & 0 \\ \frac{M_u^Z}{I_{zz}} & \frac{M_v^Z}{I_{zz}} & \frac{M_w^Z}{I_{zz}} & \frac{M_p^Z}{I_{zz}} & \frac{M_r^Z}{I_{zz}} & \frac{M_q^Z}{I_{zz}} & 0 & 0 \\ 0 & 0 & 0 & 1 & 0 & 0 & 0 & 0 \\ 0 & 0 & 0 & 0 & 1 & 0 & 0 & 0 \end{bmatrix}, U = \begin{bmatrix} \delta u \\ \delta v \\ \delta w \\ \delta p \\ \delta r \\ \delta q \\ \delta \alpha \\ \delta \gamma \end{bmatrix} \quad (5\text{-}11)$$

where A is an 8×8 time-invariant matrix consisting of the corresponding aerodynamic derivatives. Different from the flapping wing model, due to axis-symmetry, the rotational coordinates of the revolving wing configuration can be identified only by the tilt angle of stroke plane γ and the yaw angle α . The elements of the matrix are calculated by 16 separate simulations based on the base condition and lead to the following matrix:

$$A = \begin{bmatrix} -1.317 & -0.473 & -0.09 & -0.035 & 0.0698 & -0.025 & 0 & -9.8 \\ -0.473 & -1.317 & -0.09 & -0.025 & 0.0698 & -0.035 & 0 & 0 \\ 0.081 & 0.081 & -3.041 & 0.003 & -0.009 & 0.003 & -9.8 & 0 \\ -454.5 & 48.59 & 4.941 & -9.652 & 5.1168 & 34.716 & 0 & 0 \\ -1.069 & -1.069 & -276.0 & -1.677 & -378.6 & -1.677 & 0 & 0 \\ 48.59 & -454.5 & 4.941 & 34.716 & 5.1168 & -9.652 & 0 & 0 \\ 0 & 0 & 0 & 1 & 0 & 0 & 0 & 0 \\ 0 & 0 & 0 & 0 & 1 & 0 & 0 & 0 \end{bmatrix}$$

The matrix is subjected to an eigenvalue decomposition and the eigenvalues are shown in Table 5-6. The analysis indicates that the revolving wing hawkmoth has three unstable modes: mode 1 and mode 2 are unstable real modes and mode 3 corresponds to an unstable oscillatory mode. Obviously, the magnitude of real part in mode 1 is much larger than mode 2 and mode 3, and this mode will therefore dominate the hover stability of the revolving wing hawkmoth The double time t_{double} corresponding to this mode is $0.67T$ which indicates an instability that is almost five times larger than the most unstable mode in flapping-wing regime ($t_{double} = 3.7T$).

Table 5-6 Eigenvalues of 6DoF LTI system matrix of revolving wing moth

Mode	1	2	3	4	5	6
Eigenvalues	25.9	2.1	$0.6\pm3.2i$	$-4.9\pm2.4i$	–44.5	–378.6

The eigenmode associated with mode 1 is shown in Table 5-7 and it mainly consists of the horizontal velocity δu and δw , along with the tilt angle $\delta\gamma$. However the horizaontal velocity is the most dominant component in this mode. The horizontal velocity here are the most dominant factor comparing with tilt angle $\delta\gamma$. As been pointed out before, the revolving wing model is inherently unstable because of the bilaterial anti-symmetric dynamics of this configuration which couples velocity perturbation in the horizontal plane with a tilting of the vehicle.

Table 5-7 Eigen-motion of revolving wing moth in mode 1

	δu	δv	δw	δp	δr	δq	$\delta\alpha$	$\delta\gamma$
Component	10.1	10.1	0.0	–0.7	0.0	–0.7	0.0	–3.8
Normalized Magnitude	1.5	1.5	0.0	0.0	0.0	0.0	0.0	0.6

Thus the general conclusion is that from the point of view of hover stability, the bilaterally symmetric configuration of a flapping wing vehicle is significantly less unstable than a comparable revolving wing vehicle.

5.3. Linear Time Periodic (LTP) Stability Analysis

The flapping frequency of insects such as fruit flies and bumblebees is very high (~100-300 Hz) and the LTI assumption (is that the equilibrium state does not vary too much during one wing-flap) is very reasonable for these insects. However, for an insect such as a hawkmoth that flaps at a relatively low (~25 Hz)) frequency, the assumption of linear time invariance may not be accurate. In order to take the periodic variation of variables into account we have carried out a more precise stability analysis for the hovering hawkmoth, which is based on a linear time-periodic (LTP) equilibrium state (the so called Floquet (Floquet 1885) analysis). In this model, all the state variables are assumed to be periodic over the flapping cycle. Recently Wu and Sun (2012) have employed the Floquet analysis to investigate the stability of a hovering hawkmoth and dronefly at equilibrium state. They found for both insect flyers that a passively stable hovering flight state cannot be achieved due to an unstable mode related to pitch motion. Because in their analysis, the crucial feature matrix A in the dynamical system is normalized before eigen-value extraction, the corresponding eigen-motion may be disconstructed and may not reflect the real essence of flight stability of these flyers. In the current study, we have carried out the Floquet analysis with dimensional variables and then normalized the resulting eigenvalues and eigenvectors by characteristic properties to study the flight stability of a hovering moth.

5.3.1. Floquet Analysis

The Floquet analysis conducted here is limited to the longitudinal plane. A small disturbance is added to the time-periodic equilibrium state as follows

$$\begin{aligned} u(t) &= u_e(t) + \delta u(t), \;\; w(t) = w_e(t) + \delta w(t) \\ q(t) &= q_e(t) + \delta q(t), \;\; \theta(t) = \theta_e(t) + \delta\theta(t) \end{aligned} \tag{5-12}$$

where $u_e(t)$, $w_e(t)$, $q_e(t)$ and $\theta_e(t)$ denote time-periodic equilibrium state variable for horizontal velocity, vertical velocity, pitch rate and pitch angle in the body frame respectively. The equations of motion (5-1) are now linearized around the equilibrium leading to the following equation:

$$\dot{U}(t) = A(t)U(t),$$

$$A(t) = \begin{bmatrix} \dfrac{F_u^X(t)\big|_e}{m} & \dfrac{F_w^X(t)\big|_e}{m} - q_e(t) & \dfrac{F_q^X(t)\big|_e}{m} - w_e(t) & -g\cos\theta_e(t) \\ \dfrac{F_u^Z(t)\big|_e}{m} + q_e(t) & \dfrac{F_w^Z(t)\big|_e}{m} & \dfrac{F_q^Z(t)\big|_e}{m} + u_e(t) & -g\sin\theta_e(t) \\ \dfrac{M_u^Y(t)\big|_e}{I(t)} & \dfrac{M_w^Y(t)\big|_e}{I(t)} & \dfrac{M_q^Y(t)\big|_e}{I(t)} & 0 \\ 0 & 0 & 1 & 0 \end{bmatrix}, \tag{5-13}$$

$$U(t) = \left[\delta u(t), \delta w(t), \delta q(t), \delta\theta(t)\right]^T$$

where the subscript `e' represents derivatives estimated around the dynamic equilibrium . Note that these time derivatives themselves are time-periodic.

Based on Floquet theory, we know that the fundamental solution set of Eq. (5-13) satisfies the Floquet normal form as follows

$$\Phi_{\delta U}(t) = P(t)e^{Bt} = P(t)Qe^{\Lambda t}Q^{-1} \tag{5-14}$$

where $\Phi_{\delta U}(t)$ is the solution set in matrix form; $P(t)$ is a data-based cycle-periodic matrix; Λ is complex matrix called the Floquet exponent such that $e^{\Lambda t}$, the eigenvalues

matrix of e^{Bt}, are the characteristic multipliers of the system, and matrix Q is the corresponding eigenvectors matrix.

Here we present the detailed procedure of the Floquet analysis. Given the general solution to Eq. (5-13), we could let the initial condition be $\Phi_{\delta x}(0) = P(0) = \mathbf{I}$, where $\mathbf{I}$ is a 4×4 identity matrix. Due to $P(T) = P(0) = \mathbf{I}$, we have,

$$\Phi_{\delta x}(T) = P(T)e^{BT} = e^{BT}$$

According to Eq. (5-13), we know that $e^{\Lambda T}$ and Q are the eigenvalue and eigenvector matrix of $\Phi_{\delta x}(T)$, respectively. Therefore, the Floquet exponents Λ and its corresponding eigenvector matrix Q can be easily solved for by standard algorithms of eigenvalue calculation. Then, we make a variable transformation with a new vector of variables $m(t)$, where $m(t) = Q^{-1}P^{-1}(t)\delta x(t)$; this transformation leads to

$$\dot{m}(t) = \Lambda m$$

and the solution set of $m(t)$ can be derived as,

$$\Phi_m(t) = \begin{bmatrix} c_{11}e^{\lambda_1 t} & c_{12}e^{\lambda_1 t} & c_{13}e^{\lambda_1 t} & c_{14}e^{\lambda_1 t} \\ c_{21}e^{\lambda_2 t} & c_{22}e^{\lambda_2 t} & c_{23}e^{\lambda_2 t} & c_{24}e^{\lambda_2 t} \\ c_{31}e^{\lambda_3 t} & c_{32}e^{\lambda_3 t} & c_{33}e^{\lambda_3 t} & c_{34}e^{\lambda_3 t} \\ c_{41}e^{\lambda_4 t} & c_{42}e^{\lambda_4 t} & c_{43}e^{\lambda_4 t} & c_{44}e^{\lambda_4 t} \end{bmatrix}$$

where λ_i, $i = 1,\ldots,4$ are the four Floquet exponents; c_{ij}, $i, j = 1,\ldots 4$ are unknowns, but can be easily determined by the correlation $e^{BT} = Q\Phi_m(T)$. Once these coefficients are obtained, the periodic matrix $P(t)$ can be determined as,

$$P(t) = \Phi_{\delta x}(t)\left[\Phi_m(t)\right]^{-1}Q^{-1}$$

where the eigen-motion corresponding to each eigenvalue is identified as $Q^{-1}P^{-1}(t)\delta x(t)$.

5.3.2. Time-Periodic Equilibrium State of Hovering Mode

Different from LTI model, which can simply assume that the equilibrium is at a fixed null point, LTP model has to determine the dynamic equilibrium limit cycle for the system variables satisfying the following equations simultaneously.

$$u(T)-u(0)=0 \tag{5-15a}$$

$$w(T)-w(0)=0 \tag{5-15b}$$

$$q(T)-q(0)=\int_0^T \frac{M(t)}{I(t)}dt=0 \tag{5-15c}$$

$$\theta(T)-\theta(0)=\int_0^T q(t)\,dt=0 \tag{5-15d}$$

Since the wing kinematics of hawkmoth is extracted from high speed video from animals stably hovering and feeding in front of a flower (Hedrick et al. 2006) and the reconstruction of wing kinematics is very precise (Zheng et al. 2013), the calculated drag and lift approximately satisfy cyclic-periodicity the aerodynamic induced longitudinal velocities are therefore also nearly cycle-periodic as in Eq. (5-15a) & (5-15b). The limit cycle of these numerically calculated velocities, which are approximated in Fourier series, is visualized in Fig 5-5.

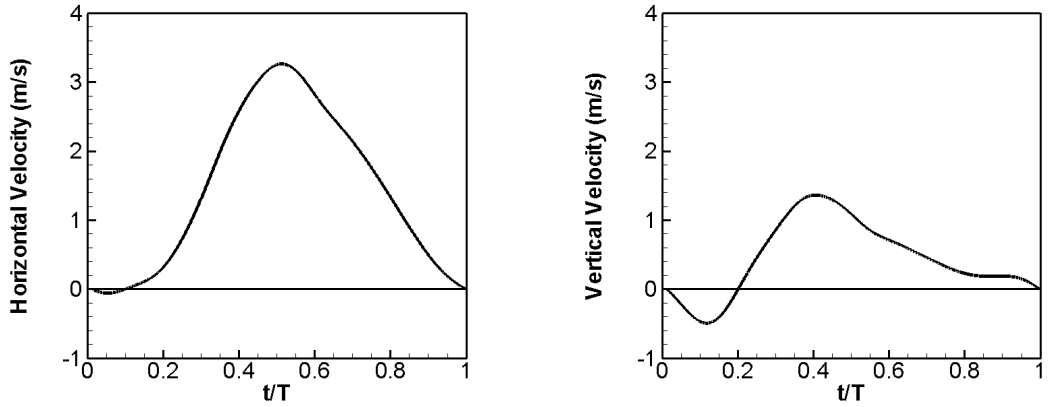

Figure 5-5 Limit cycle of (a) horizontal velocity $u_e(t)$ and (b) vertical velocity $w_e(t)$ at equilibrium state.

According to LTI model's result, the pitch motion is the key factor in the longitudinal instability. The only element that has not been clearly identified but which is of great significance in the calculation of pitch-torque is the location of center of mass (CoM). Due to the missing information about mass distribution of moth body and inherent errors in the 3D segmentation, the location of CoM cannot be simply obtained by numerical calculation. However, given the wing kinematics, the force production at each time instant is known via numerical simulation. Fig 5-5(a) shows the numerically computed force vectors and the trajectory of center of pressure in the longitudinal plane throughout the full cycle. If we consider that the center of mass of the moth body is fixed in space, then the pitch torque can be related to the force by the following equation,

$$M^Y(t) = F^Z(t)\left(x_{cop}(t) - x_{com}\right) - F^X(t)\left(z_{cop}(t) - z_{com}\right) \tag{5-16}$$

where $x_{cop}(t)$ and $z_{cop}(t)$ are the coordinates of the center-of-pressure CoP.; If we substitute Eq. (5-16) into Eq. (5-15c), we can obtain the neutral line for pitch-rate (green line in Fig 5-5(a)). The significance of this line is that if the CoM is located on this line,

the net change of pitch rate over one cycle will be zero. Similarly, we can determine the neutral line for pitch-angle by solving the coupled solution of Eq. (5-13) & Eq. (5-12d) and this is visualized as a cyan line in Fig 5-6(a).

These two sets of intersecting neutral lines provide a useful way to interpret the pitch stability of the hovering hawkmoth. Generally, if the CoM is located on the left side of the neutral lines, the net change of corresponding variables (pitch rate or pitch angle) will be positive and vice versa ($^{+}$: net increase; $^{-}$: net decrease for q and θ). Consequently, these two lines divide the longitudinal plane into four sub-domains. It follows from this divison that if and only if the CoM lies at the intersection of those two neutral lines, the dynamic equilibrium depicted by Eq. (5-15c) & Eq. (5-15d) will be achieved. For the purposes of conducting the LTP analysis, the CoM is artificially prescribed to be exactly located on the cross-point and the resulting limit cycles of pitch torque, pitch rate and pitch angle are plotted as shown in Fig 5-6(b)(c)(d).

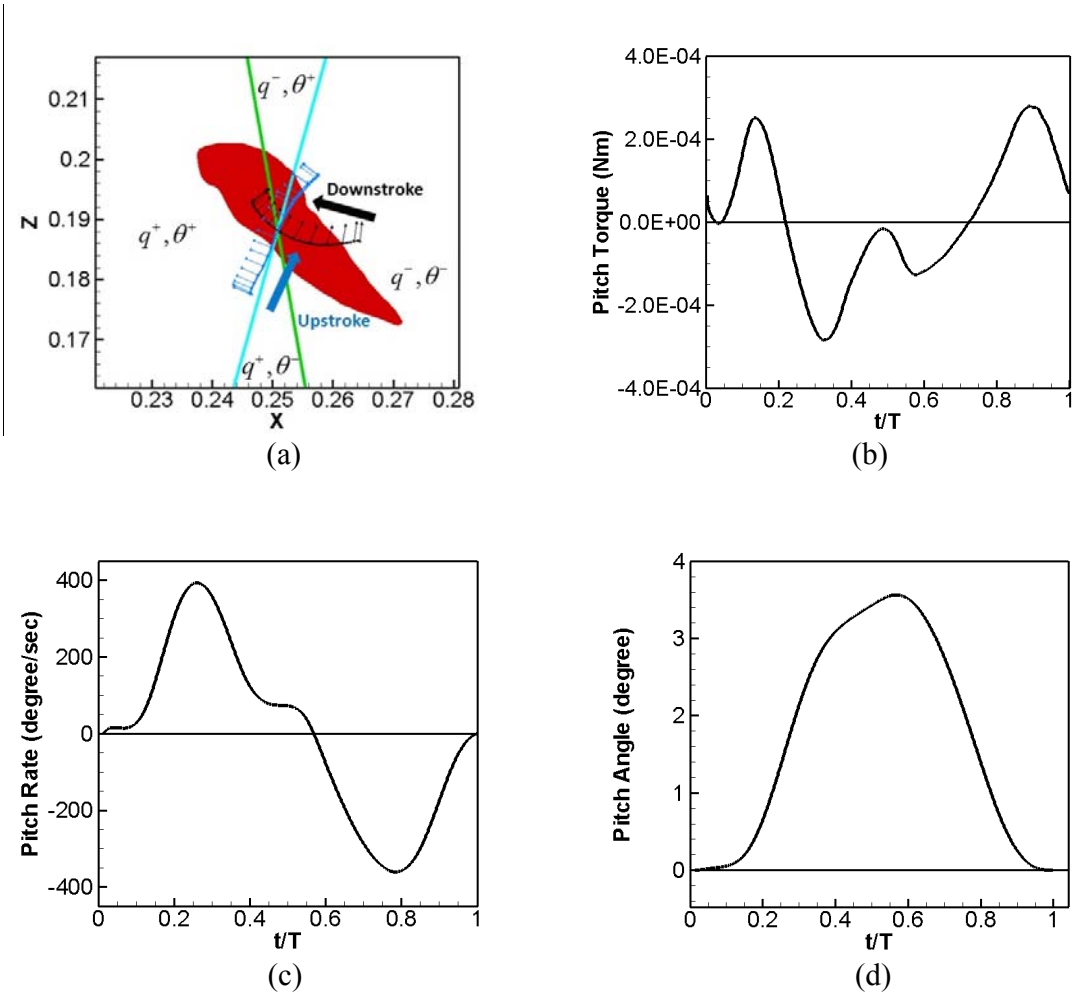

Figure 5-6 (a) Trajectory of instantaneous force vectors ("▬": Downstroke; "▬": Upstroke) and neutral lines for pitch rate "▬" and pitch angle "▬"; (b) Time series of pitch torque at equilibrium; (c) Limit cycle of pitch rate at equilibrium; (d) Limit cycle of pitch angle at equilibrium.

5.3.3. Results

In the current LTP analysis, each aerodynamic derivative is also obtained by running a reference group of simulations with varying magnitudes of initial time-invariant perturbations to the four key variables (u, w, q and θ). We note that a more general

Floquet analysis might include time periodic perturbtions but we don't address such perturbations in current work. The time series of the nine aerodynamic derivatives in Eq. (5-10) are presented in Fig 5-7. Note that all derivatives are expressed in terms of a Fourier series with 9th order to ensure strict cyclical periodicity.

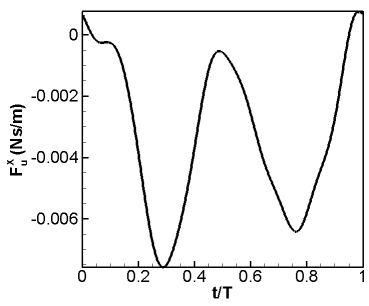

(a) $F_u^X(t)\big|_e$

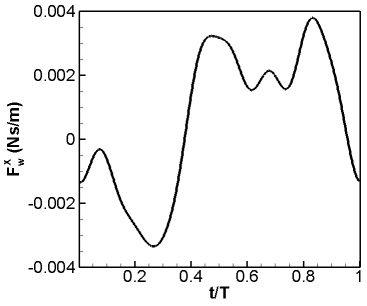

(b) $F_w^X(t)\big|_e$

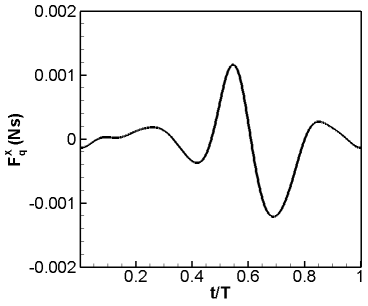

(c) $F_q^X(t)\big|_e$

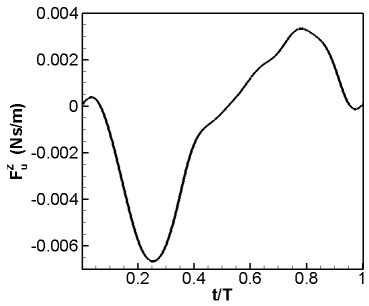

(d) $F_u^Z(t)\big|_e$

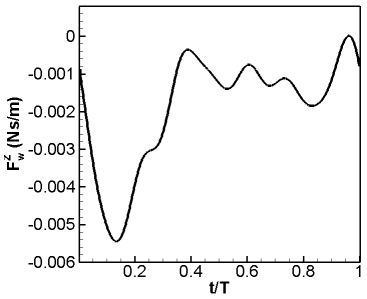

(e) $F_w^Z(t)\big|_e$

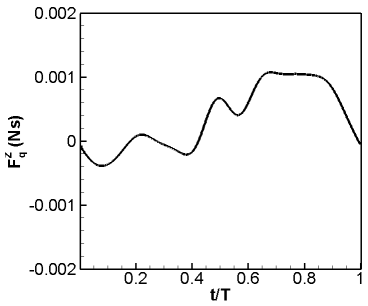

(f) $F_q^Z(t)\big|_e$

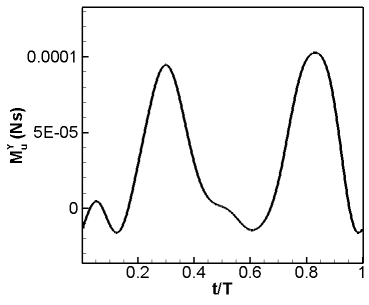

(g) $M_u^Y(t)\big|_e$

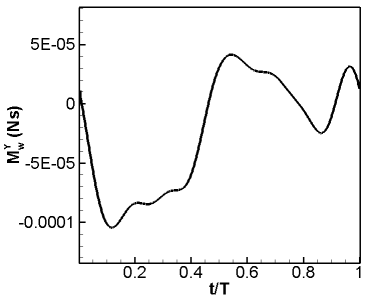

(h) $M_w^Y(t)\big|_e$

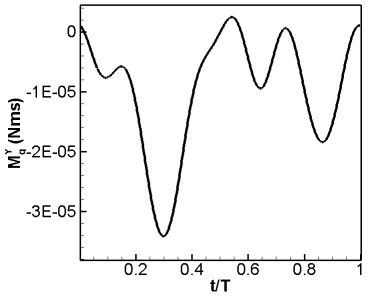

(i) $M_q^Y(t)\big|_e$

Figure 5-7 Time series of aerodynamic derivatives at equilibrium.

Through Floquet structure extraction, we have found the three Floquet exponents shown in Table 5-8. The fact that the real parts of all the exponents are negative indicates that the hawkmoth at the equilibrium of hovering is passively stable, although mode 3 is close to the margin of unstable region because of its smallest magnitude of real part.

Table 5-8 Floquet exponents of longitudinal LTP system matrix

Mode	1	2	3
Exponents	−59.57	−1.83	$-0.50 \pm 4.61i$

According to Floquet analysis, we know the form of solution of the LTP system is

$$x(t) = \sum_{i=1}^{n} c_i \mathrm{q}_i e^{\lambda_i t} \tag{5-17}$$

where c_i is the constant related to initial condition of system variables; λ_i is the Floquet exponents; q_i is the eigenvector corresponding to λ_i; and $i = 1, \ldots, n$ denotes different eigen-mode. Fig 5-8, 5-9 & 5-10 show the normalized components of each eigenvector q_i of the three modes. All components are normalized via Eq. (5-4) as well. From Fig. 5-10, we could see that the eigen-motion corresponding to the marginally stable mode ($\lambda_3 = -0.50 \pm 4.61i$) can be mainly characterized as the linear combination of horizontal velocity u, vertical velocity w and the pitch rate q.

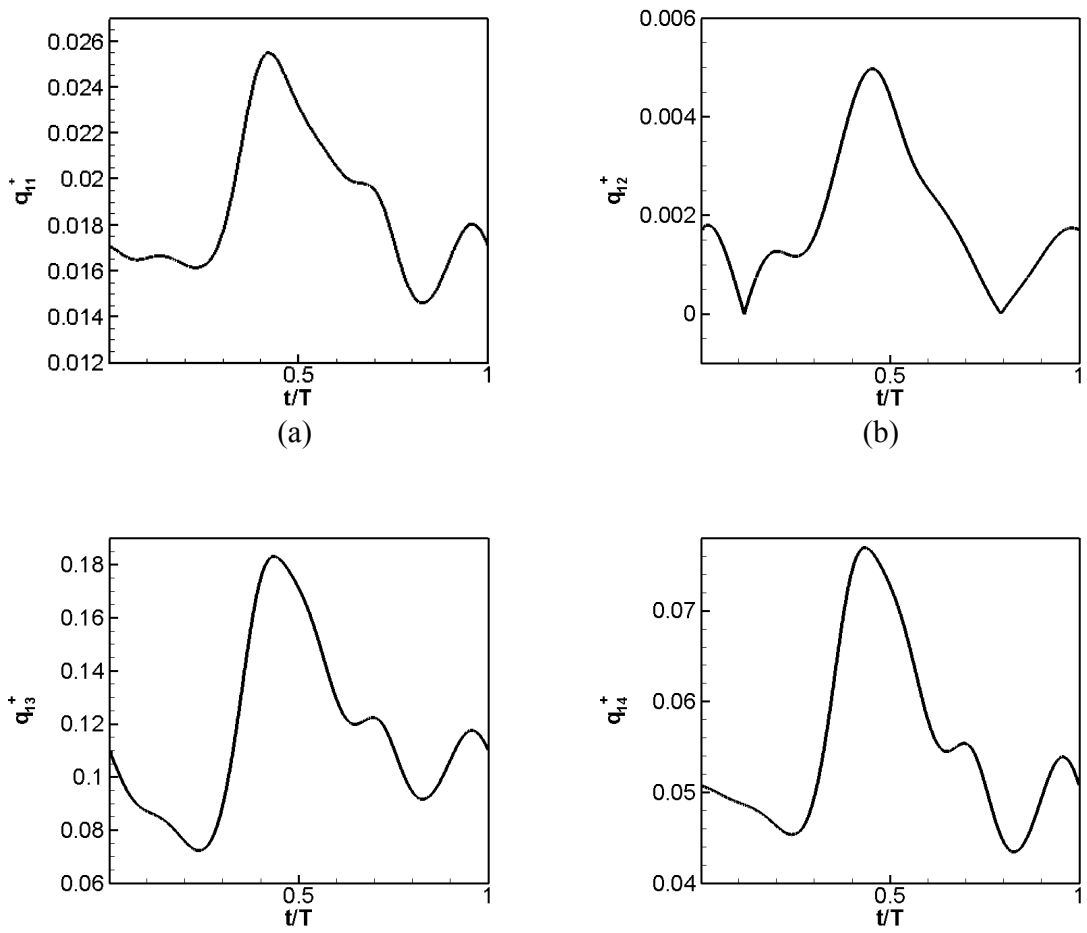

Figure 5-8 Time series of four components in mode 1

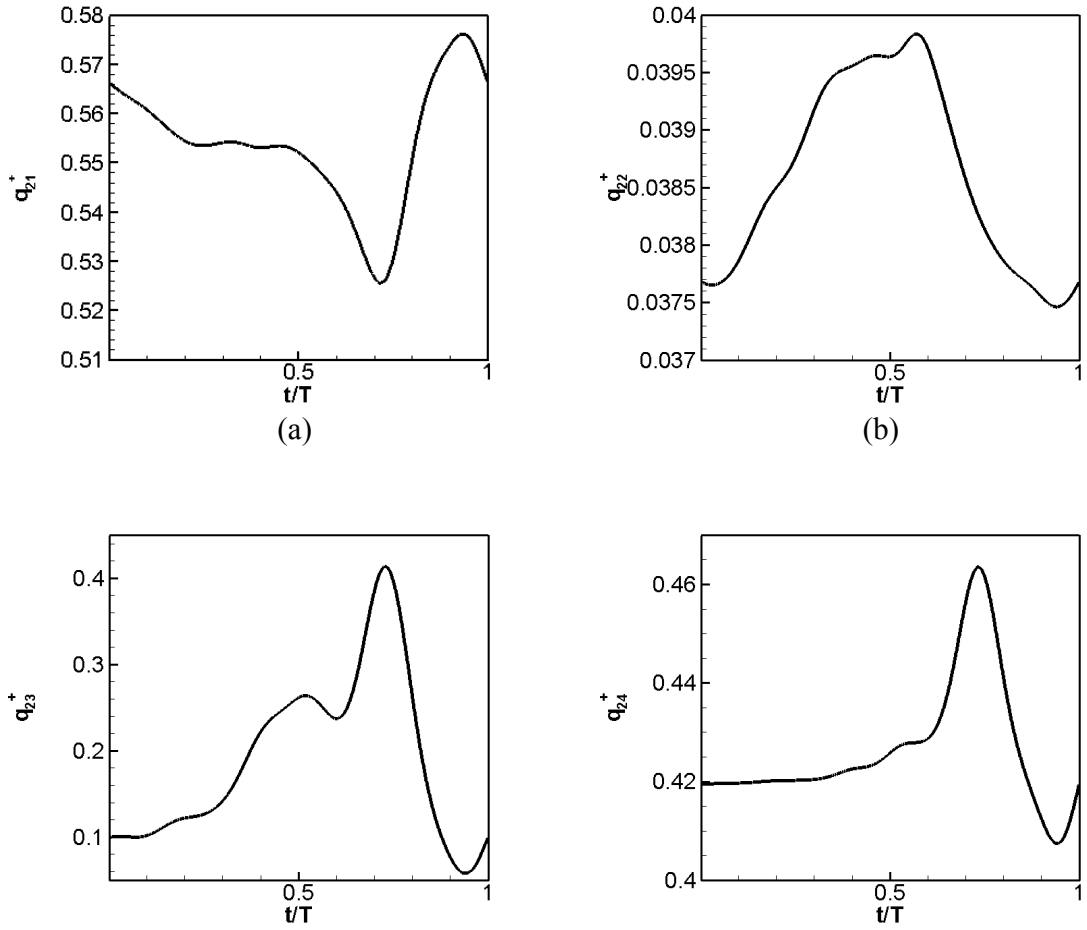

Figure 5-9 Time series of four components in mode 2

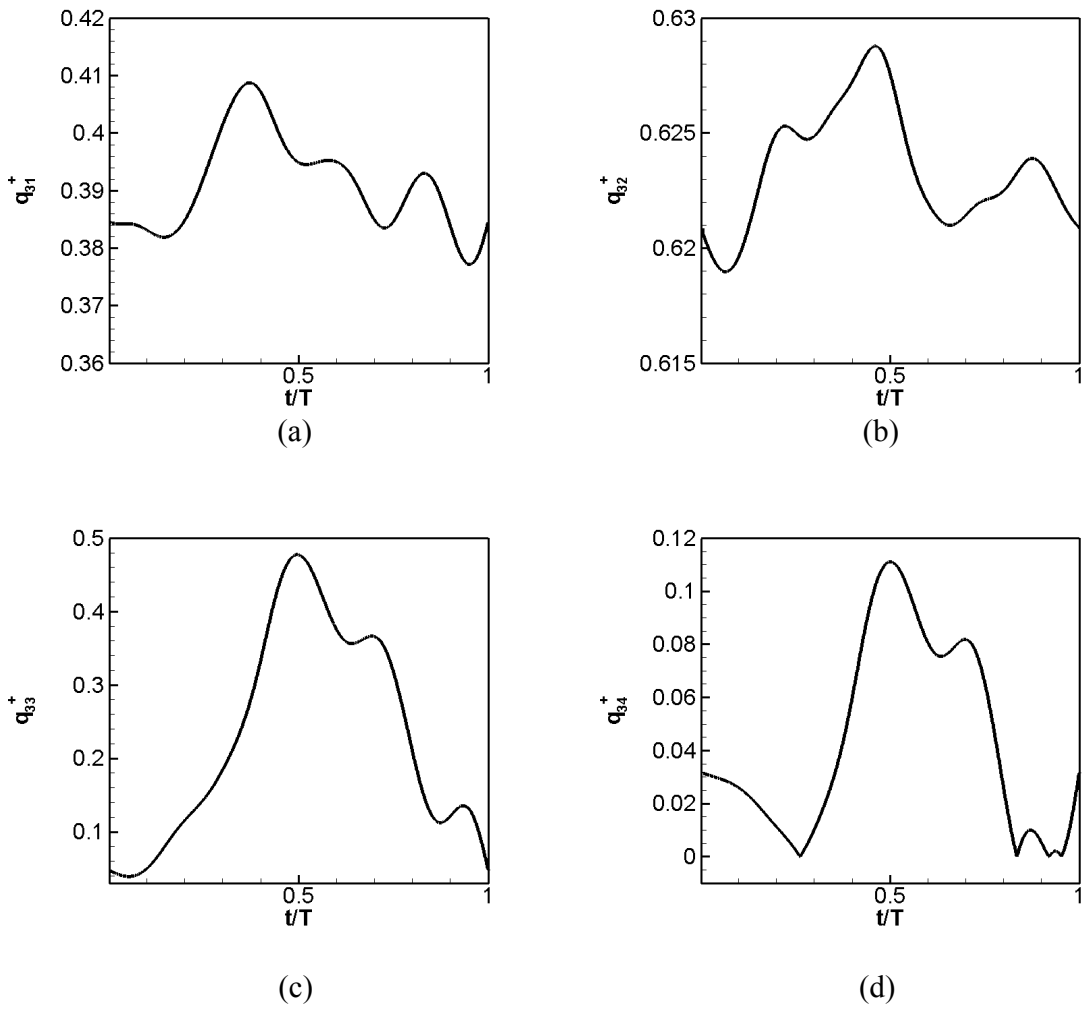

Figure 5-10 Time series of four components in mode 3

It is surprising that the LTP model gives a result that contradicts that obtained from the 3DoF LTI analysis. The result is also out of line with that by Wu and Sun (2012) and they also tend to go against what is considered conventional knowledge of the stability of hovering flight by flapping wings. A detailed investigation of the method of analysis was conducted to determine the possible sources of error but this investigation was unsuccessful in identifying any specific error. It is quite likely that the numerical value of the eigenmodes is sensitive to body geometry and wing kinematics and slight changes in

these might destabilize the marginally stable oscillatory modes. Confirmation of this is left as possible work to be done in the future.

CHAPTER 6. STABILIZATION OF HOVERING FLIGHT IN HAWKMOTHS USING FEEDBACK CONTROL

6.1. Introduction

The 3DoF and 6DoF linear time-invariant (LTI) stability analysis described in Chapter 4 of this dissertation indicate that dynamic (oscillatory) instability in pitch is one of the dominant modes of instabilities for a hovering hawkmoth. Analysis of the center-of-pressure (CoP) variation in time and the determination of neutral axes for pitch angle and pitch rate (see Fig. 6-1) below indicate that the CoM needs to be exactly coincident with the intersection of these two axes in order to eliminate this pitch instability. Such stabilization cannot be accomplished via an "open-loop" control system due to the following reasons: (a) the CoM varies slightly over the flapping cycles due to the motion of the wings which, although light, do contribute a small component to the mass; and (b) the CoM of a hawkmoth might change significantly over the period of hours/days due to natural behaviors such as feeding, dehydration and egg-bearing. Thus any stabilization strategy should be able to directly or indirectly "sense" the mismatch between the CoM and the neutral point during flight, and then be able to change the body/wing configuration so as to eliminate the destabilizing effect of this mismatch.

The objective of the research described in the current chapter is to propose and test a novel feedback control strategy for stabilizing the hovering flight of insects. The strategy described here has its foundation in experimental observations and the objective here is to demonstrate that not only can this strategy stabilize flight in quiescent flows, but that it also performs well in highly disturbed flows.

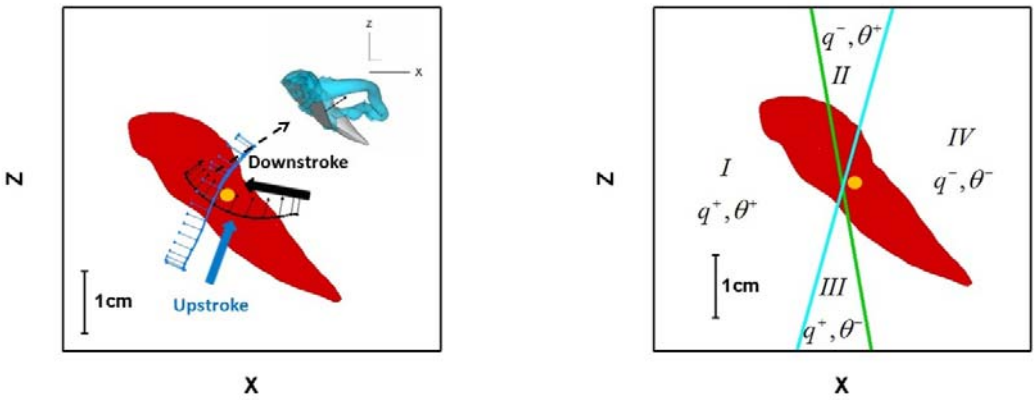

Figure 6-1 (a) Trajectory of instantaneous force throughout a cycle and the sub-figure inside shows the instantaneous flow structure at t/T=0.4; (b) Neutral lines for pitch rate (Green) and pitch angle (Cyan). Positive sign of pitch angle or pitch rate indicates it is anticlockwise rotating and vice versa. ”+” represents pitching down and ”−” represents pitching up. Yellow dot is the COM.

6.1.1. Abdominal Flexion and Stroke-Plane Adjustments as a Strategy for Flight Stabilization

It has been widely observed that abdominal flexion movement in hawkmoths is induced in response to changes in the orientation of the hawkmoth relative to the environment (Hedrick et al. 2006; Hinterwirth et al. 2010). Although these experiments were conducted for tethered insect flyers and the details of the sensory mechanism involved in this type of feedback control for a freely hovering hawkmoth is not totally clear, it has been suggested that this is a plausible feedback control based strategy that is employed by hawkmoths in free flight (Cheng, et al, 2011). A recent study by Dyhr (2013)

also suggests that abdominal flexion can be used to redirect lift forces and could be sufficient to stabilize the hover of a hawkmoth.

Additional evidence of such a mechanism can be seen in recordings of freely hovering hawkmoths. We have ourselves examined the hovering flight of a hawkmoth stably hovering and feeding from a stationary flower and have found evidence of periodic abdominal flexion. In Fig. 6-2, we show some qualitative proof for this phenomenon and make the following remarks:

1. Abdominal flexion follows an oscillatory mode (schematically marked by yellow lines) at a much lower frequency than flapping frequency;
2. The stroke plane of flapping wings (schematically marked by blue lines) stays nearly fixed w.r.t the lab frame while the abdomen is flexed by the hawkmoth throughout the whole recorded cycles.

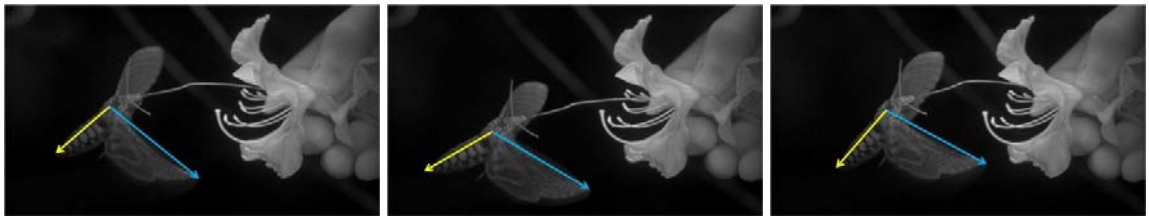

(a) (b) (c)

Figure 6-2 Snapshots from high speed video of free hovering hawkmoth feeding from a still flower (a) 1st cycle; (b) 5th cycle and (c) 8th cycle. The blue arrow connects the thorax to the wing tip and yellow arrow shows the location of tail w.r.t. thorax. These experiments have been conducted by Dr. Tyson Hedrick at UNC Chapel Hill.

We have also examined data generated by the Hedrick Lab (UNC Chapel Hill) on the stabilization of hovering hawkmoths to large aerodynamic perturbations. In these experiments, discrete flow perturbations are provided to hawkmoths in hover via directed vortex rings. Moth – vortex interactions are observed to produce large perturbations in the target moth (Fig. 6-3). Axial vortex perturbations like the one shown in the figure result in pitch perturbations; the vortex perturbations were also found to produce different responses from the moth depending on the timing of the moth-vortex interaction. If the oncoming vortex reaches the moth during the downstroke, as in Fig. 6-3, the moth pitches up in response. If the vortex reaches the moth during the upstroke, the moth pitches down in response.

Figure 6-3 A hawkmoth experiencing a longitudinal vortex perturbation. In this case the vortex reaches the moth at approximately mid-downstroke and results in a pitch-up perturbation of the moth. Vortices that arrive at mid-upstroke result in pitch-down perturbations of the moth. These

experiments have been conducted by Dr. Tyson Hedrick at UNC Chapel Hill.

The principle wing motion response of the moth to these axial perturbations is to adjust the stroke plane angle of the wings with respect to the horizontal plane back toward the original, unperturbed position. Fig. 6-4 shows the complete time course of the moth's pitch perturbation in response to the vortex interaction from Fig. 6-3 along with the orientation of the wing stroke plane with respect to horizontal and also with respect to the moth's body axis. One wing beat after the perturbation arrives, the moth begins changing its wing orientation with respect to the body, reaching a maximum deviation near wing stroke 6. The overall effect of changing the stroke plane angle so as to keep it close to the original orientation rather than allowing it to move along with the body is a mechanism for stability that is explored further in this chapter via computational modeling.

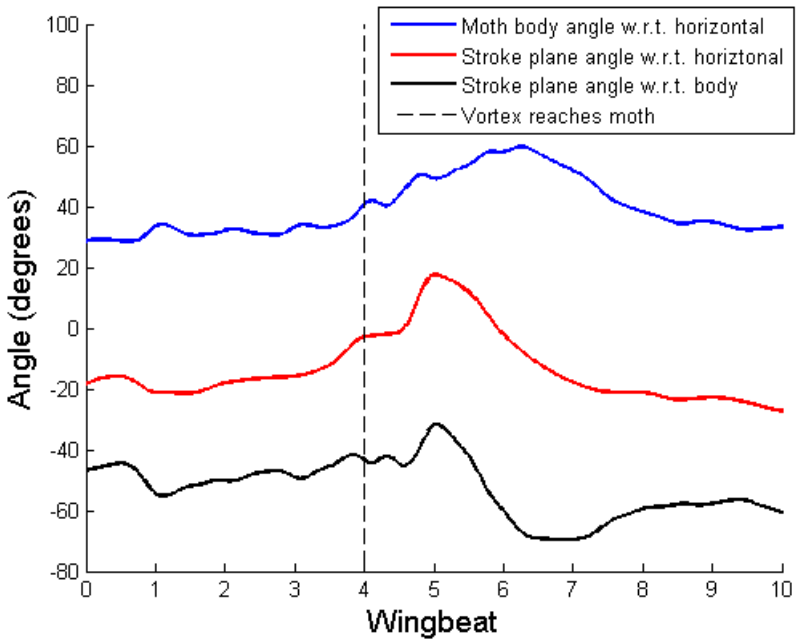

Figure 6-4 The time series of body pitch, wing stroke plane angle relative to horizontal and stroke plane angle relative to the body for the moth – vortex interaction shown in Fig. 6-3. The dashed vertical line corresponds to the upper right panel in Fig. 6-3. Note the decrease in the stroke plane angle relative to body during wing beats 6 and 7; this is part of the moth's flight control response to the perturbation.

6.1.2. Sensing and Actuation for Hover Stabilization

Feedback control of hover requires two elements in addition to the knowledge of aerodynamic force generation and body dynamics; these are modalities for sensing attitude (body position, attitude, horizon, rotation rate etc) and ways of actuating some appropriate mechanisms that can react to sensory inputs and generate forces/moments for control.

The various sensory modalities of insect flyers have been studied extensively in the past (Fry, et al, 2009; Sane, et al, 2007; Straw, et al, 2010; Hinterwirth, et al, 2010). The most widely used sensory system is the visual system. For instances, Fry et al. (2009) conducted a series of experiments in a one-parameter open-loop paradigm to investigate the modulation of flight speed via the visual sensory system, and eventually identified a meaningful high-level control principles by applying genetic algorithms. Straw et al. (2010) found the sensory-motor mechanism of motion control employed by Drosophila can be identified as an integrated visual feedback approach in the horizontal and vertical planes simultaneously. Besides the vision-based sensory controller, the antennal mechanosensor has also been found to serve a crucial role in the active control of hovering hawkmoth flight, in a role analogous to the halteres of two-winged insect flyers (Sane et al. 2007). It is reported (Sane, et al, 2007) that the mediation of rotational velocities in locomotion is accomplished by sensing the Coriolis force exerted on the flagellum of the antenna, which could be much faster than the vision-based control. Moreover, the antenna, as the mechanosensor of flying Drosophila, can also be used to detect the wing induced airflow during vision-guided turning process (Mamiya, et al, 2011). These two sensing modalities (i.e. visual sensing of angular position and mechanosensory measurement of angular rate) will be incorporated in the feedback control system that is investigated here.

With regard to actuation, it is well established (Anderson, et al, 1976; Federle, et al, 2001) that many insects have two sets of muscles; one set of the muscles (usually the indirect muscles) power the flapping of wings and the other set (usually the direct mucles)

are used for fine control of the flapping wing. This duality provides an effective paradigm for the actuation strategy required for hover stabilization.

6.2. Computational Framework

Investigation of flight stabilization in a hawkmoth involves interaction between flight forces and body dynamics and requires the incorporation of sensing and actuation for control. Therefore, in order to investigate the mechanism of flight stabilization of hawkmoths in unrestrained free flight in a realistic way, we have developed a complete computational framework (see Fig. 6-5) that incorporates all of these elements.

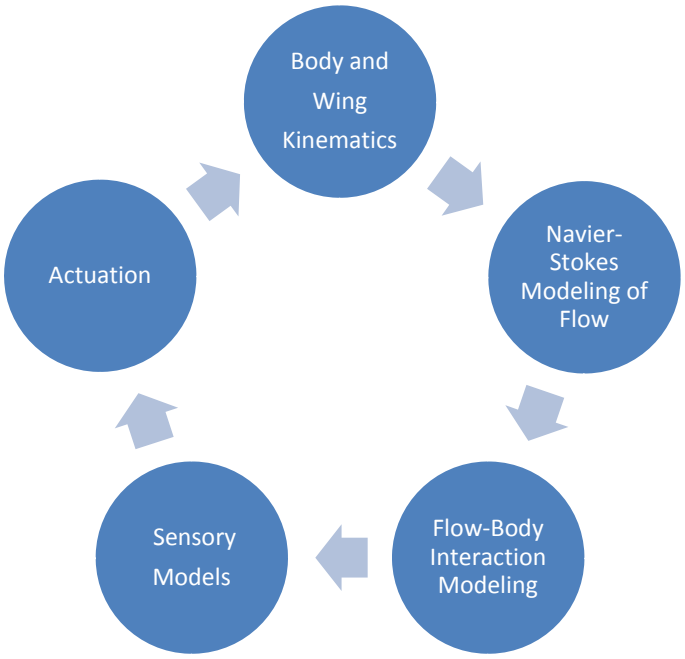

Figure 6-5 Computational framework developed for exploring flight stabilization.

6.2.1. Navier-Stokes Aerodynamics Solver and Simulation Set-up

In our study, a versatile sharp interface immersed boundary method (Ghias, et al, 2007; Mittal, et al, 2008; Seo, et al, 2011) is used to simulate the aerodynamics of the free hovering moth flight (Zheng, et al, 2013). The governing equations of aerodynamic flow

during insect flight are the three-dimensional unsteady, viscous incompressible Navier-Stokes equations:

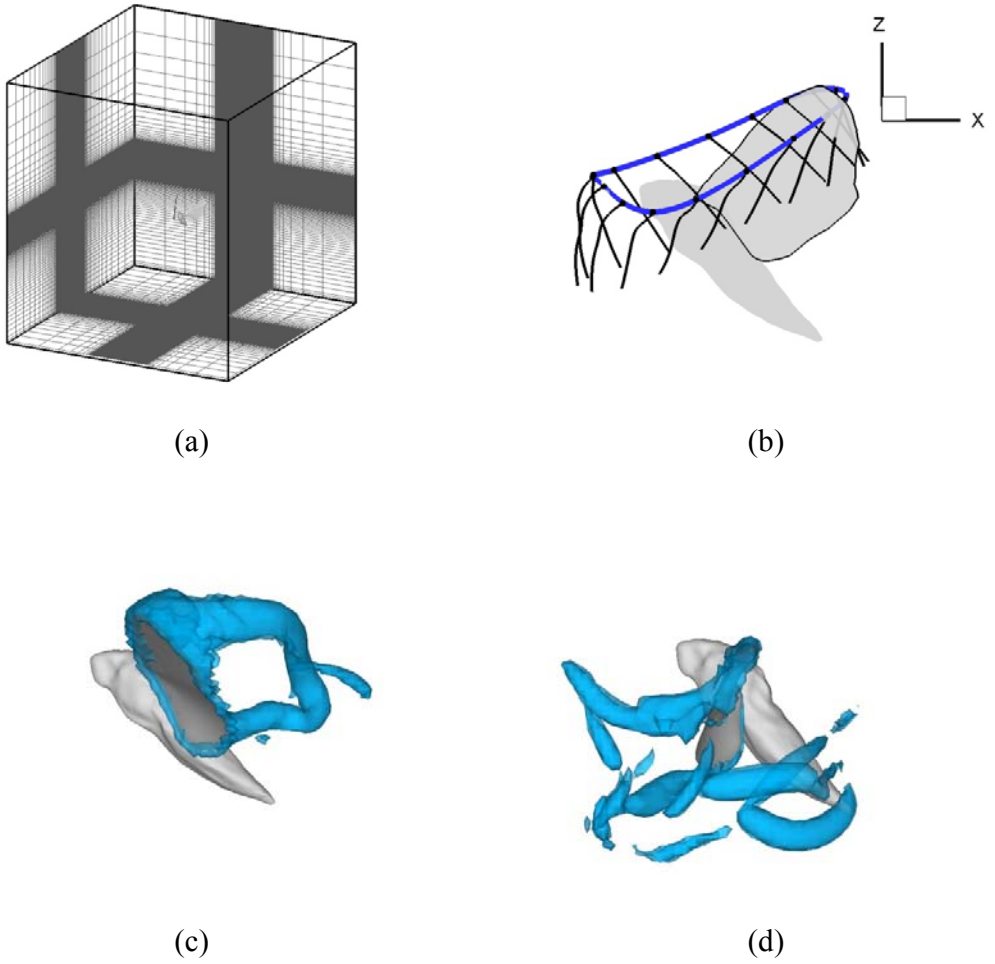

Figure 6-6 (a) The mesh setup of hovering hawkmoth; (b) Standard wing kinematics throughout a whole flapping cycle featured by trajectory of 2/3 wing span leading edge point and the chordlines; (c) Vortex Structure of fixed moth with standard wing kinematics at t/T=0.31; (d) Vortex Structure of fixed moth with standard wing kinematics at t/T=0.77.

$$\frac{\partial u_i}{\partial x_i}=0,\ \ \frac{\partial u_i}{\partial t}+\frac{\partial u_i u_j}{\partial x_j}=-\frac{1}{\rho}\frac{\partial p}{\partial x_i}+\nu\frac{\partial}{\partial x_j}\left(\frac{\partial u_i}{\partial x_j}\right);\ \ i,j=1,2,3 \tag{6-1}$$

where u_i is the flow velocity component corresponding to direction i; p is the flow pressure, and ρ and ν are the fluid density and fluid kinematic viscosity, respectively. All other details regarding this method can be found in Chapter 2. In this study, all the CFD simulations are conducted on a non-uniform $128\times128\times128$ point Cartesian grid with 700 time-steps per flapping cycle. Further detailed validation and grid convergence can be found in Zheng, et al (2013).

6.2.2. Wing Kinematics and Flow-Induced Body Dynamics (FIM) Simulation

Without losing much fidelity, we employ a biologically derived wing shape and kinematics for our model; these are based on an earlier high-speed video recording and Navier-Stokes simulation of moth flight (Zheng, et al, 2013). In order to achieve flight control, we assume that the entire stroke plane can be "pitched" about the wing hinge by an additional actuator. This produced the standard wing kinematics input for the simulation as in Fig. 6-6(b). The Reynolds number of hovering hawkmoth is defined as $\mathrm{Re}=U_{tip}\bar{c}/\nu$. Here U_{tip} is the averaged wing tip velocity; $\bar{c}$ is the mean wing chord length; ν is the kinematic viscosity. For this particular hovering hawkmoth, the mean chord length and mean tip velocity are measured to be $\bar{c}=1.77\mathrm{cm}$ and $U_{tip}=4.3ms^{-1}$, respectively. The Reynolds number is specified to be Re=1000. The motion of hawkmoth is governed by 6DoF equations of motion in the global frame fixed to the ground as shown in Eq. (6-2).

$$M\frac{d\vec{x}}{dt}=\vec{F},$$

$$M=\begin{bmatrix} m & 0 & 0 & 0 & 0 & 0 \\ 0 & m & 0 & 0 & 0 & 0 \\ 0 & 0 & m & 0 & 0 & 0 \\ 0 & 0 & 0 & I_{xx} & I_{xy} & I_{xz} \\ 0 & 0 & 0 & I_{yx} & I_{yy} & I_{yz} \\ 0 & 0 & 0 & I_{zx} & I_{zy} & I_{zz} \end{bmatrix},\quad \vec{x}=\begin{bmatrix} u \\ v \\ w \\ \omega_x \\ \omega_y \\ \omega_z \end{bmatrix},\quad \vec{F}=\begin{bmatrix} F_x \\ F_y \\ F_z \\ M_x \\ M_y \\ M_z \end{bmatrix} \tag{6-2}$$

$\vec{x}$ and $\vec{F}$ denote the 6DoF velocity vector and force and moment vector respectively; M is the mass matrix. However it cannot be explicitly solved because the instantaneous force vector $\vec{F}$ is directly connected to the solution of Navier-Stokes equation in the following way,

$$\vec{F}=\int_B (p\hat{n}+\hat{\tau})\cdot\vec{f}dS,\quad \vec{f}=\begin{bmatrix} \vec{e}_x \\ \vec{e}_y \\ \vec{e}_z \\ y\vec{e}_z - z\vec{e}_y \\ z\vec{e}_x - x\vec{e}_z \\ x\vec{e}_y - y\vec{e}_x \end{bmatrix} \tag{6-3}$$

where $\vec{e}_x$, $\vec{e}_y$ and $\vec{e}_z$ denote the unit vector in x, y and z axis respectively; and the pressure p and shear stress $\hat{\tau}$ are calculated by solving the Navier-Stokes equation. Eq. (6-2) can be coupled with the Navier-Stokes equations either with an explicit or implicit coupling scheme. The explicit coupling (weakly or loosely coupled) scheme calculates the current time derivative by interpolation with the information of force and moment at previous time step as follows:

$$M_{n-1}\frac{\vec{x}_n-\vec{x}_{n-1}}{\Delta t}=\vec{F}_{n-1} \tag{6-4}$$

A number of studies show that the explicit coupling scheme exhibits an inherent instability due to added mass effects when the density ratio (the ratio of solid density to the surrounding fluid density) is close to 1 or even smaller (Mok, et al, 2001; Causin, et al, 2005; Forster, et al, 2007, Zheng, et al, 2010). Many types of full or partitioned implicit coupling schemes have been developed as alternatives with good numerical stability, but at a much higher computational cost. However, because the density ratio of the hawkmoth examined here is very large (~ 800) explicit coupling is viable for this configuration and is the scheme of choice.

6.2.3. Length Preservation Scheme for Fluid Body Interaction

As mentioned earlier, the wing kinematics are extracted from high speed video and numerically pre-stored in terms of instantaneous local velocity vectors defined in the ground-fixed frame. At every computational time step, due to the fact that the orientation is always varying, we use a 3D rotation matrix to convert the vectors to those in the body-fixed frame. Theoretically, this matrix is of the form:

$$\vec{V}_n' = R_1 \cdot R_2 \cdots R_n \vec{V}_n,$$

$$R_n = \begin{bmatrix} \cos\theta_n + \left(\omega_x^n\right)^2 (1-\cos\theta_n) & \omega_x^n \omega_y^n (1-\cos\theta_n) - \omega_z^n \sin\theta_n & \omega_x^n \omega_z^n (1-\cos\theta_n) + \omega_y^n \sin\theta_n \\ \omega_y^n \omega_x^n (1-\cos\theta_n) + \omega_z^n \sin\theta_n & \cos\theta_n + \left(\omega_y^n\right)^2 (1-\cos\theta_n) & \omega_y^n \omega_z^n (1-\cos\theta_n) - \omega_x^n \sin\theta_n \\ \omega_z^n \omega_x^n (1-\cos\theta_n) - \omega_y^n \sin\theta_n & \omega_z^n \omega_y^n (1-\cos\theta_n) + \omega_x^n \sin\theta_n & \cos\theta_n + \left(\omega_z^n\right)^2 (1-\cos\theta_n) \end{bmatrix} \tag{6-5}$$

where $\vec{V}_n'$ and $\vec{V}_n$ denote the local velocity vector in the body-fixed and lab-fixed frame respectively at current time step n; matrix R_n is the rotation matrix at time step n, θ is the magnitude of rotational angle between $\vec{V}_n$ and $\vec{V}_{n-1}$; ω_x^n, ω_y^n and ω_z^n are the

instantaneous rotational velocity components in x, y and z axis respectively. However, treatment of the local velocity induced by rotation as time invariant within the short time interval dt specified in the simulation introduced error in length that can accumulate over time. On the basis of Eq. (6-5), an additional length-preserved correction step is applied to the local velocity calculation. By using the following formulation (Eq. (6-6)), we can prevent the length of any two local points on the rotating body from being stretched or shrunk numerically.

$$\vec{V}_n'^c = \frac{(I + R_n)\vec{V}_n'}{2}\cos\frac{\theta_n}{2} \tag{6-6}$$

where $\vec{V}_n'^c$ is the correction term of the local velocity vector in the body-fixed frame. Eventually, the real value for local velocity on the body is obtained by summing the flow-induced velocity component with the prescribed velocity component $\vec{V}_n'^c$.

6.2.4. Mass Properties of Hawkmoth

The mass properties of moth body and wings were measured from a moth population (Zheng, et al, 2013). Although the mass of two wings accounts for only $\sim 0.07 gram$ ($\sim 4\%$ of the total mass), the contribution to the moment of inertia (MoI) is much greater (the averaged MoI component corresponding to pitch is up to $\sim 22\%$ of the total MoI). Here we assume the mass distribution for hawkmoth body and wings are uniform through the body and wing.

6.2.5. Free Hovering Hawkmoth Simulation without Controller

The first simulation conducted in this study was for a hawkmoth hovering in a quiescent flow with no feedback control implemented. In these simulations the Navier-

Stokes are fully coupled to the 6DoF equations of motion for the hawkmoth body with wing kinematics fixed with respect to the body. The governing equations for this configuration can conceptually be thought of as the following,

$$M\frac{d\vec{V}}{dt} = \vec{F}_{aero} - Mg\hat{k} \tag{6-7a}$$

$$\frac{d}{dt}\left(\vec{\mathrm{M}}_W\right) = \vec{T}^{W}_{aero} + \vec{T}_{W-B} \tag{6-7b}$$

$$\frac{d}{dt}\left(I_B\vec{\Omega}_B\right) = \vec{T}^{B}_{aero} - \vec{T}_{W-B} \tag{6-7c}$$

where I^B is the pitch-related moments of inertia (MoI) of the moth body; $\vec{\Omega}_B$ denotes the pitch rate of the body and wings and $\vec{\mathrm{M}}_W$ denotes the angular momentum of two wings in pitch; T^B_{aero} and T^W_{aero} are the external aerodynamic pitch torques physically exerted on the body and wings; T_{W-B} is the internal pitch torque exerted by the flight muscles to generate the flapping of the wings;

Fig. 6-7 summarizes the results from this simulation. The results clearly show that the hovering moth is highly unstable in pitch. It also comes as no surprise that the observed deviation is in longitudinal motion (pitch, vertical and fore-aft) since prior studies, as well as our own LTI analysis (see Chapter 5) have established this is the least stable mode (Taylor, et al, 2002; Wu, et al, 2012).

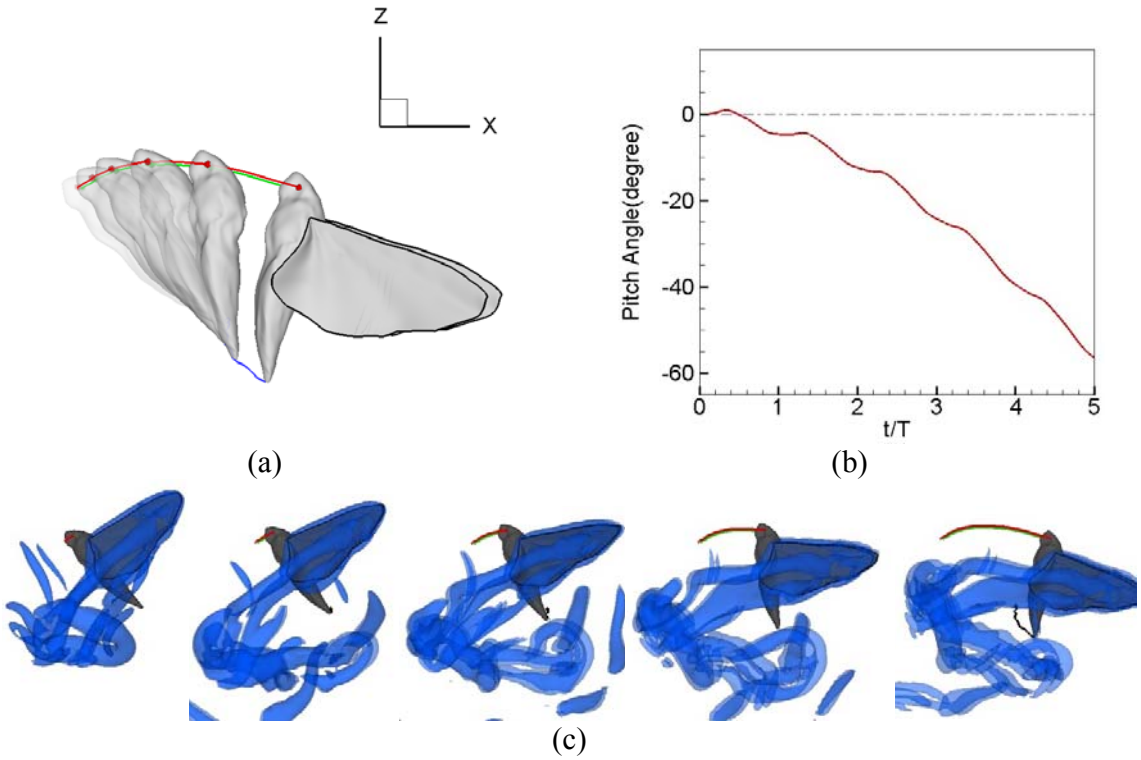

Figure 6-7 (a) The trajectory of motion of a simulated freely hovering hawkmoth throughout five flapping cycles without active control; (b) The pitch angle of the hawkmoth through time. Positive sign of pitch angle or pitch rate indicates it is anticlockwise rotating and vice versa; (c) Sequence of plots showing vortex structures and body configuration for moth in open-loop hover mode.

6.3. Longitudinal Stabilization of Hover via Feedback Control

6.3.1. Equilibrium State for Hover

Before feedback control of longitudinal motion can be considered, we first need to identify a dynamic equilibrium condition for the moth. The details of how the dynamic equilibrium is achieved, is described in Sec. 5.3.2 of Chapter 5 and will not be repeated here.

6.3.2. Idealized Controller of Pitch Motion by Preventing Stroke Plane from Tilting

The relative change in angle between the body and stroke plane of the wing as well as the tendency of the hawkmoth to preserve it original inclination of the stroke plane inspired us to hypothesize that relative rotation between wing and body in such a way as to maintain the original inclination of the stoke plane could be a possible strategy for hover stabilization. From the high-speed video, the stroke plane is observed to be non-tilted throughout many cycles, despite changes in abdominal and body orientation. We also note that when the CoM is shifted to the left side of the neutral line of pitch angle (zone I and zone II in Fig. 6-1(b)), the net change of pitch angle θ will be positive (pitching down). However, if the position of the stroke plane is kept fixed, the increase of pitch angle will lead to the motion of the COM back to the right side of angle neutral line, resulting in an upward pitching motion, and back and forth. This non-tilted stroke plane configuration couple with body oscillation relative to the stroke plane could result in a stable loop because the instantaneous forces generated by the non-tilted stroke plane act to damp pitch angle and prevent the COM from going too far as it consistently pitches up or pitches down.

To conduct a "sanity test" of this hypothesis we have conducted a fully coupled 6DoF CFD simulation with this idealized controller embedded into the equations that couple the flow and the 6DoF dynamics model. This may be viewed as being governed by the following equations,

$$M\frac{d\vec{V}}{dt} = \vec{F}_{aero} - Mg\hat{k} \tag{6-8a}$$

$$\frac{d}{dt}\left(I_W\omega\hat{j}+\vec{\mathrm{M}}_W\right)=\vec{T}_{aero}^{W}+\vec{T}_{W-B}+\vec{T}_C \tag{6-8b}$$

$$\frac{d}{dt}\left(I_B\vec{\Omega}_B\right)=\vec{T}_{aero}^{B}-\vec{T}_{W-B}-\vec{T}_C \tag{6-8c}$$

where $\vec{T}_C$ is an internal control torque that is designed to impart an additional prescribed pitch-rate $\omega\hat{j}$ to the wing. In the current phase of the study, we assume zero latency in the sensory-actuation system and the control torque is chosen so as to cancel any deviation in the pitch of the wing from equilibrium condition at each time-step.

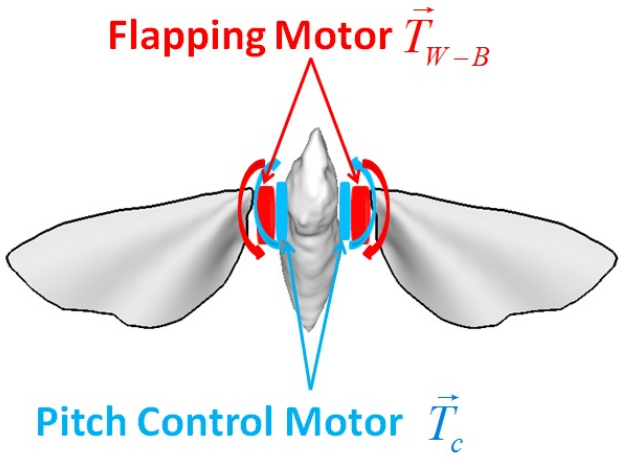

Figure 6-8 Schematic of two sets of flight controllers based on wing root.

As Eq. (6-8) describes, the ideal model exactly transfers the instantaneous aerodynamic torque required for a fixed stroke plane from the pair of wings to the moth body with no time delay. In this scenario, the latency of feedback to aerodynamics stimulus is zero and the bandwidth is infinite. And as shown in the Fig. 6-8, only the constraint of rotation at wing root of the 6DoF full coupled model hawkmoth is released

and replaced by a rotation damper, which can operate to prevent the stroke plane from tilting with no latency.

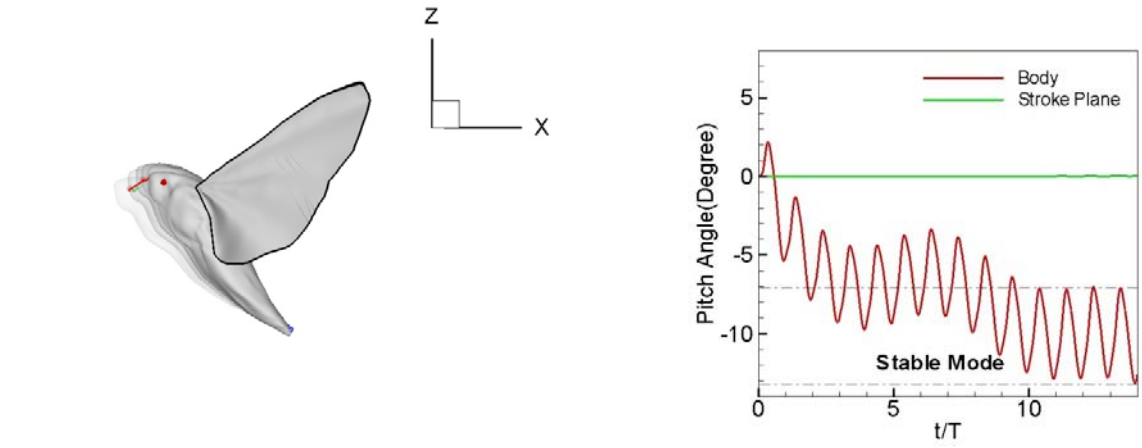

(a) (b)

(c)

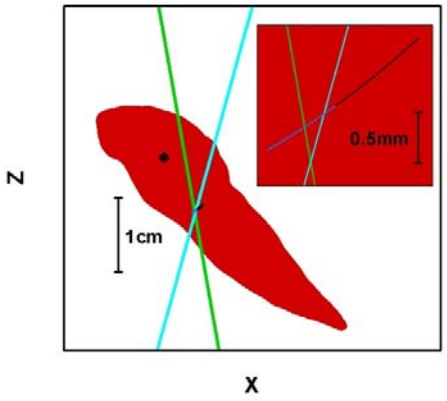

(d)

Figure 6-9 (a) The trajectory of motion of simulated free hovering hawkmoth throughout six

cycles with the non-tilted stroke plane pitch controller in global frame; (b) The time series of pitch angle of the hawkmoth body and stroke plane (fixed); (c) The vorticity iso-surface of hovering moth with idealized controller at t/T=1,2,3,4,5 respectively; (d) The vorticity iso-surface of hovering moth with idealized controller at t/T=5.03; (e) The trajectory of COM in hinge-fixed frame.

We implemented this idealized pitch controller in our simulated hawkmoth with fully coupled 6DoF flow induced motion simulation. Fig. 6-9(a) shows the trajectory of motion in six cycles with the trajectory of the eyes and abdomen tip color-coded so as to enable easy tracking of the motion of the moth. Fig. 6-9(b) shows that by transferring the pitch torque from wings to body, the resulting relative pitch angle of hawkmoth body will cause a torque of the opposite sign on the body of the hawkmoth and the stetem eventually reaches a stable oscillatory state (i.e. limit-cycle) with an amplitude of oscillation of approximately 6 degrees. Furthermore, the final limit-cycle configuration has a mean relative pitch-angle between the body and the wing stroke plane of only about about 10 degrees, which provides further confirmation that the feedback control strategy employed here is not unreasonable. If for instance, the final configuration had a much larger relative angle that would not be consistent with the experimentally based recording of the hawkmoth on which these simulations are based. Fig. 6-9(e) shows the movement of the CoM during the stable portion of the hover and interestingly, we find that the stable configuration corresponds to an oscillation of the CoM about the neutral point that take it back-and-forth between quadrants I and IV (as shown in Fig. 6-1(b)).

The strategy of transferring pitch torque among body and wings for pitch stabilization can be used in various circumstances, including large longitudinal perturbations such as

those resulting from a hovering hawkmoth encountering a vortex ring. The Hedrick lab has carried out these experiments and we simulated this situation as a test of our feedback stabilization strategy. In the experiment, the longitudinal vortex ring with the incoming was shot from a spring-loaded plunger vortex gun aimed at the abdomen of a freely hovering hawkmoth; The diameter of vortex gun is $0.1m$ and velocity of the vortex ring is about 0.3 m/s. In the numerical simulation, the vortex wing perturbation is generated by a jet impulse from the boundary of computational domain with the same circular diameter and at the same distance; furthermore, the idealized pitch controller with zero latency is also activated and fully coupled with the 3DoF body-dynamics simulation. Fig. 6-10 shows a comparison of the experiment (left panel) and the simulation (the right panel). The simulations are carried over the entire duration of the ring impact and its eventual passage past the hawkmoth which is a total of about 8 flapping cycles and it is clear from Fig. 6-10 that the simulated moth maintains stability despite the large aerodynamic perturbation.

(a) 2nd cycle

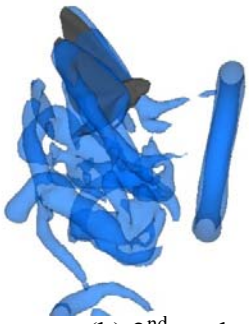

(b) 2nd cycle

(c) 4th cycle

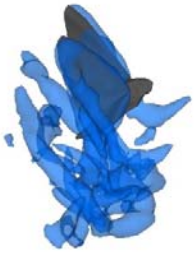

(d) 4th cycle

(e) 6th cycle

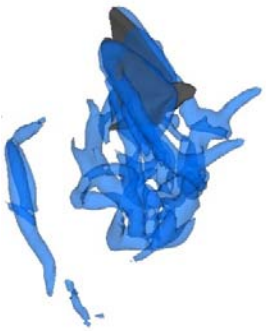

(f) 6th cycle

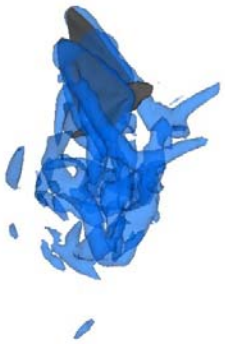

(g) 8th cycle (h) 8th cycle

Figure 6-10 Snapshots of free hovering hawkmoth from high-speed video 8(a)8(b)8(c)8(d) and from numerical simulation 8(e)8(f)8(g)8(h) at 2nd , 4th , 6th and 8th cycle respectively. These experiments have been conducted by Dr. Tyson Hedrick at UNC Chapel Hill.

Fig. 6-11 shows the time-variation of the pitch angle of the body and the wing w.r.t. their original values over the duration of the eight wing-strokes simulated here we clearly see that the initial pitch-up motion generated due to the impact of the vortex ring is damped out over 5 cycles (3rd to 8th cycle) by rotation of the body relative to the stroke plane. After the effect of perturbation is gone, the moth body will finally return to the oscillatory stable mode as shown in Fig. 6-6(b).

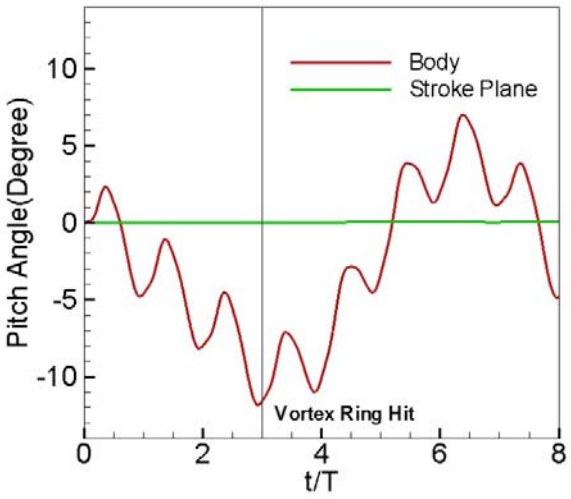

Figure 6-11 Time series of pitch angle of body and stroke plane under vortex ring perturbation.

6.4. Neurosensory System Mediated Active Pitch Controller

The idealized controller with zero latency indicates that the strategy of relative pitch motion between the wing and the body might be effective in stabilizing hover even in the face of large aerodynamic perturbations. However, all sensory motor control systems in animals operate with some finite latencies and gains and the objective of the research described in this section is to examine the pitch-stabilization strategy with a more realistic model of the sensory motor control system of the hawkmoth. The sensory modalities for insect flight stability and control have been the subject of much research over the past decade (Sane, et al, 2007; Maimon, et al, 2010; Straw, et al, 2010; Mamiya, et al, 2011; Noda, et al, 2014) and we employ some of this previous knowledge in developing a mathematical model of our pitch controller.

The notion underlying the pitch controller is that there are two primary sensory systems that are employed by a hawkmoth to detect it's orientation in the longitudinal plane: the antennae which sense pitch-rate via the Coriolis force and the visual system

that detects pitch angle; both these systems are used simultaneously in order stabilize hover and each of these sensory modalities have specific latencies and gains. The equation describing this type of sensory-motor control system for hover stabilization is written in terms of the pitch control torque as follows:

$$T_C = G_C \cdot \left(\omega^{W*} - \omega^W \left(\lfloor t/t_C \rfloor \cdot t_C \right) \right) + G_V \cdot \left(\theta^{W*} - \theta^W \left(\lfloor t/t_V \rfloor \cdot t_V \right) \right) \tag{6-9}$$

ω^W and θ^W are pitch rate and pitch angle of the stroke plane (of two wings) and superscript "$*$" denotes the desired condition for the corresponding quantity; G_C and G_V are the output gains for the Coriolis force and visual sensory systems respectively, and t_C and t_V are the corresponding time-latencies. The operator $\lfloor \ \rfloor$ is the truncation or "floor" operator that ensures that control outputs are kept constant over the duration of the time-latency for a given modality. The objective of the current research is to explore the effect of the control gains and latencies for the two sensory modalities on hover stabilization.

6.4.1. Linearized Model of Aerodynamic Torque

Investigation of the effect of the control gains and latencies for the two sensory modalities on hover stabilization requires simulation of many dozens (even hundreds) of case of flow-induced body dynamics and this is not feasible to accomplish with the full Navier-Stokes body dynamics coupled model. Each of these simulations takes many weeks to complete on a large scale parallel computer and conducting $O(100)$ simulations is just not possible.

In order to circumvent this problem, we have developed a linearized model of the aerodynamic torque as an alternative to the Navier-Stokes model. The model is based on the idea of Dickson, et al. (2006) who proposed this idea for investigating flight control model in a fruit-fly (*Drosophila melanogaster*). This model is based on the assumption of quasi-steady aerodynamics. We focus here on the aerodynamic pitch torque, which is the key element in the stabilization and propose the following linearized model for this quantity:

$$T_{aero} = T^*_{aero} + \left(\frac{\partial T_{aero}}{\partial \omega}\right)^* \left(\omega - \omega^*\right) + \left(\frac{\partial T_{aero}}{\partial u}\right)^* \left(u - u^*\right) + \left(\frac{\partial T_{aero}}{\partial w}\right)^* \left(w - w^*\right) \qquad (6\text{-}10)$$

where T_{aero} is the total aerodynamic torque exerted on the hawkmoth and $\frac{\partial T_{aero}}{\partial \omega}$, $\frac{\partial T_{aero}}{\partial u}$ and $\frac{\partial T_{aero}}{\partial w}$ are the torque derivatives with respect to pitch rate, horizontal velocity and vertical velocity, respectively. These derivatives are obtained in a way similar to that explained in Chapter 5 for the Floquet analysis (See Fig. 5-7): simulations are carried out for two different perturbation values of each variable (ω , u and w) about its equilibrium value (which is limit cycle introduced in Chapter 5) and the time series of instantaneous aerodynamic wing torque is calculated for each of these conditions. A simple finite-difference approximation then provides the above derivatives.

Eq. (6-10) then replaces the Navier-Stokes equations in the parameter exploration of latencies and gains. The idea is to use this simplified aerodynamic model to determine the effect of latency and gain on the moth stability and to simulate the full Navier-Stokes – 3DoF coupled system for some selected cases to assess the prediction of the simplified aerodynamic model.

6.4.2. Effect of Gain on the Sensory-Motor Control System on Hover Stabilization

In order to start the exploration of latency and gain, we need some estimate typical values of the latencies and gains of these systems. The response time of the two sensory modalities (visual and mechanosensory) in Drosophila flight control has been studies experimentally by Dickson et al. (2006). In their study, the temporal response of the mechanosensory system (which in the case of the Drosophila is the haltere) is found be fast (approximately one tenth of the flapping cycle) compared to its visual system, which can take up to a full flapping cycle. Taking a cue from this, we choose the baseline latencies of the Coriolis force sensor and the visual sensor in the hawmoth to be $0.1T$ and $1T$ respectively, where T is the period of the flapping cycle. There is very little understanding of what values of the gains are typical for these sensory modalities and this is the first issue that we explore using the simplified model.

The gains and latencies in both systems are normalized in the following way,

$$G_C^* = G_C / mgLT, G_V^* = G_V / mgL \tag{6-11}$$

$$t_C^* = t_C / T, t_V^* = t_V / T \tag{6-12}$$

where G_C and G_V are the gains for mechanosensory and visual systems, respectively; superscript "*" denote the normalized parameter; $m$is the total mass of hawkmoth ($1.6g$), g is the gravity ($9.8N/mg$), L is the span of a single wing ($0.044m$) and T is the stroke period ($0.04s$).

In the first set of studies, the latencies for Coriolis force sensor and the visual sensor are fixed to the baseline values indicated above. Then, the value of the gains G_C and G_V

are varied from 0 to 0.56 and from 0 to 0.56, respectively in steps ΔG_C and ΔG_V of 7×10^{-3} and 7×10^{-3} spacing respectively. This corresponds to a total of 6400 simulations, and this large search of the parameter space is made possible by the simple, linearized model of the aerodynamic torque. Each simulation is carried out for 20 flapping cycles and hover stability measured by the maximum cycle-averaged pitch (or tilt) angle of the stroke plane relative to its starting value. Fig. 6-12, shows this quantity plotted over non-dimensional parameter space of G_C^* and G_V^*

1. Except for two points where the stability boundary touches the x and y axis of the plot, non-zero gains for both the visual sensor and the Coriolis force sensor are required in order to stabilize the hover of the hawkmoth.
2. Due to the non-linearity of the dynamical system, there is a sharp bifurcation from stability to instability and this occurs once the pitch angle of stroke plane reaches 20 degrees.
3. The gains for the two sensory systems, that are most effective for stabilization and which confine the tilting of the stroke plane to within a low (below 5 degrees), range of tile angles are in the vicinity of $G_C^*=0.029$ and $G_V^*=0.058$.

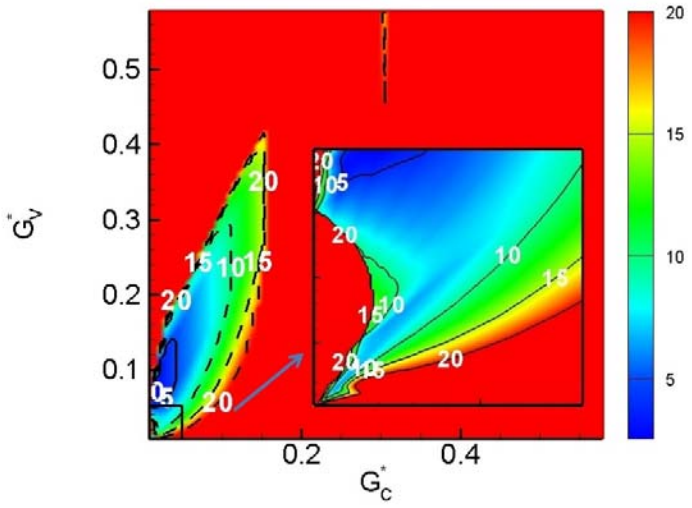

Figure 6-12 Contour map of peak value of stroke plane tilt angle over 20 cycles correlated with the non-dimensional gains of mechanosensory (Coriolis force sensor) and visual feedback.

In order to validate the results of the simple aerodynamic torque model, we have also conducted fully coupled CFD-3DoF simulations for two specific cases located in the stable region and unstable region respectively. In both cases, the non-dimensional latencies of the mechanosensory feedback and visual feedback are fixed as 0.1 and 1 respectively. In Case 1 (stable), we chose the non-dimensional gains of mechanosensory system and visual system to be 0.029 and 0.058 respectively while in case 2 (unstable), the value of the two non-dimensional gains are chosen to be 0.435 and 0.145. Fig-13 shows a comparison of the tilt angle between the CFD-3DoF and the simplified model for both the case, and the plots show an exceptionally good agreement between the two models. In case 1, the tilt angle of stroke angle is stably confined in the range of $(-5^\circ, 5^\circ)$ in either calculation; while in case 2, a sudden surge of tilt angle occurs due to the over-amplified gains. Figure 6-13(c) and (d) show the time variation of control torque and aerodynamic torque for these two cases and it is observed that in the stable case (see Fig.

6-13(c)) the control torque two orders-of-magnitude smaller than the aerodynamic torque; while in the unstable case, the control torque is apparently comparable to the aerodynamic torque. For the stable case, the fact that the control torque is significantly smaller than the flapping torque is inline with what is expected since the indirect muscles that power wing flapping are significantly more powerful than the direct muscles control the make small adjustments to the wing kinematics. From the viewpoint of bioinspired control also, this is a useful finding since is shows that a control system based on the current idea would need very small control inputs in order to stabilize a flapping wing vehicle.

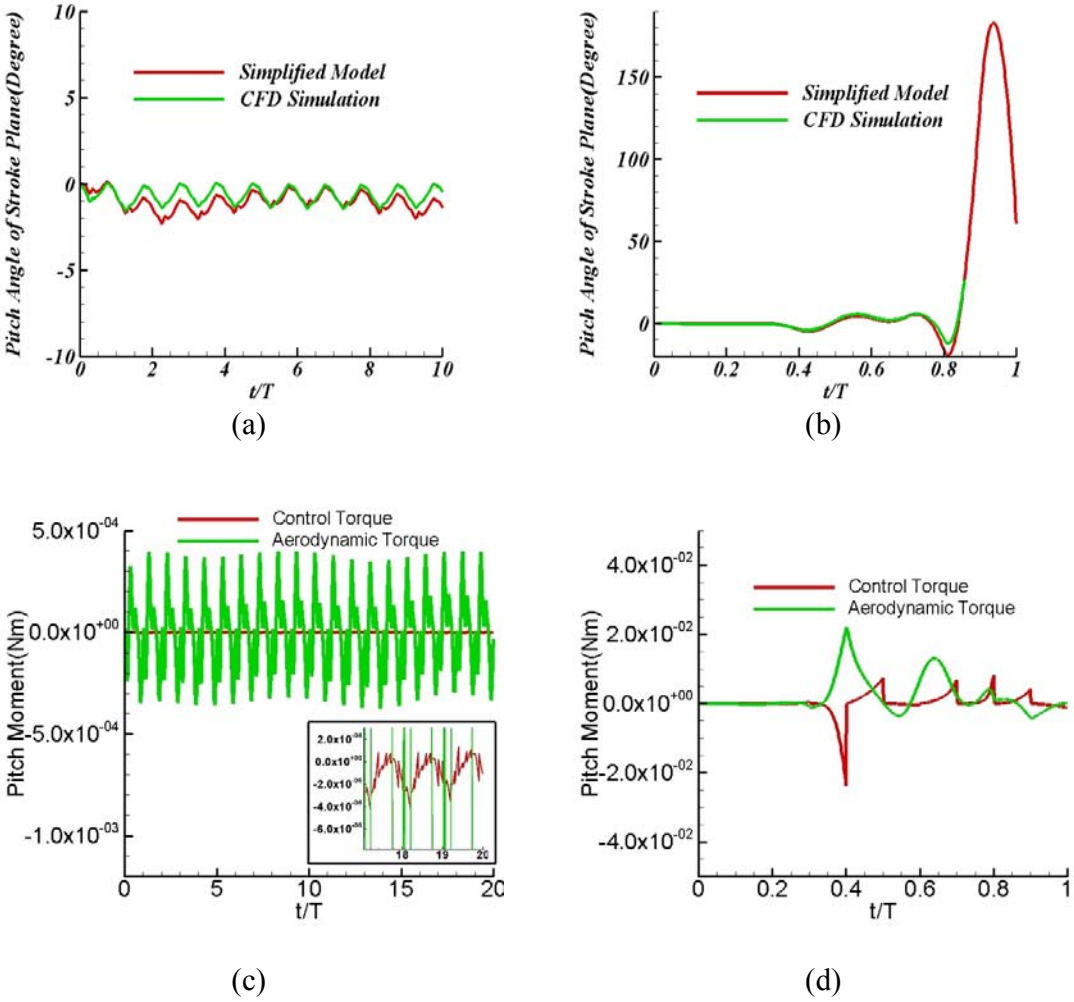

Figure 6-13 Comparison of simplified model and CFD simulation in time series of stroke plane tilt angle (a) case 1 with $G_C^* = 0.029$ and $G_V^* = 0.058$; (b) case 2 with $G_C^* = 0.435$ and $G_V^* = 0.145$; Time series of control torque and aerodynamic torque in case 1 (c) and case 2 (d).

6.4.3. Effect of Latency on the Sensory-Motor Control System on Hover Stabilization

Once our simplified model is validated and the appropriate values of the two gains are obtained, we can now use the same procedure to explore the effect of latency on the

control effectiveness. Values of $G_C^* = 0.029$ and $G_V^* = 0.058$ are chosen Fig. 6-14 increasing varying the non-dimensional mechanosensory and visual latencies from 0 to 1 and 0 to 10 respectively with corresponding steps sizes of 0.0125 and 0.125. The phenomenon of bifurcation is presented as well. It is found that the contour map in this case is significantly more complex and disordered than that for the gains. Nevertheless, some overall patterns are clear: stability requires the non-dimensional mechanosensory latency to be less than about 0.8 and the visual latency to be less than 2. The bifurcation to instability is particularly sharp as the visual latency increases past 2T and seems to be somewhat insensitive to the mechanosensory latency.

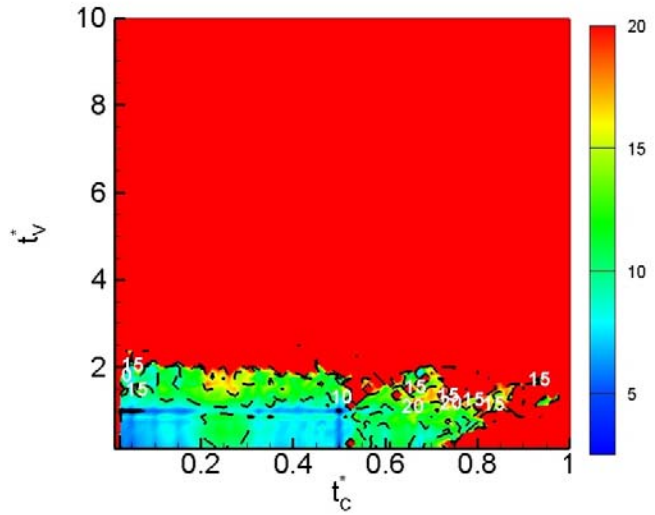

Figure 6-14 Contour map of peak value of stroke plane tilt angle over 20 cycles correlated with the non-dimensional latencies of mechanosensory (Coriolis force sensor) and visual feedback.

If we choose the combination of $G_C^* = 0.029$, $G_V^* = 0.058$, $t_C^* = 0.1$ and $t_V^* = 1$ to be the standard value for the gains and latencies, which is located in the stable region of the map, then the time series of stroke plane tilt angle and moth body oscillation can be also computed via the simplified model, and these are plotted in Fig. 6-15. It can be noticed

from this figure that not only is stroke plane strictly bounded in the low range of tilt angle, the oscillations in the position of the hawkmoth body can be stabilized by keeping stroke plane horizontal via the feedback control strategy. Furthermore, a low dominant low-frequency oscillation is very apparent in the pitch angle of the body which is further examined below.

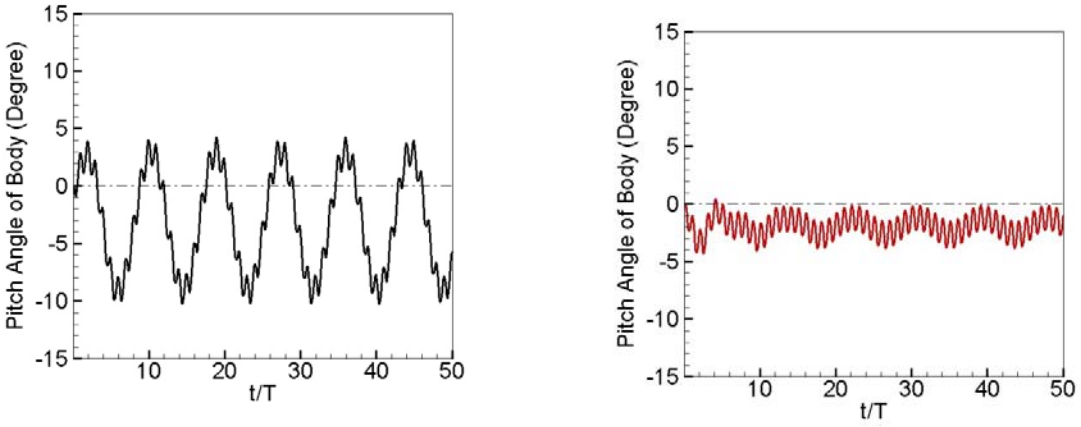

(a) (b)

Figure 6-15 Time series of pitch angle of (a) hawkmoth body and (b) stroke plane with standard latencies and gains.

It can be also be recalled from the previous observation of the high speed video recording of the moth in hovering flight that the flexion of abdomen performs at a much lower frequency the than flapping frequency. We have taken these video recordings and computed the frequency spectrum of the abdomen pitch angle w.r.t to the lab frame during hover and this data is compared to our mathematical prediction for the case described above. The two spectra are found to have some significant similarities: both spectra have a large peak in the frequency range between 2.5Hz and 4Hz and this

corresponds to the large time scale (6 to 10 flapping cycles) time-period over which the abdomen is flexed, thereby slowly oscillating the CoM back and forth across the neutral stability point. Both spectra also show a second smaller peak around 25 Hz, which corresponds to the flapping frequency of the hawkmoth.

Thus, the above serves as an assessment (validation would be too strong a word for this) of the feedback control strategy against actual moth data. The conclusion is that the strategy of maintaining the stroke plane in its original orientation by allowing relative rotational motion between the wing and the body is effective for hover stabilization and might indeed be one strategy that is used by hovering hawkmoths. Furthermore, this feedback control requires a combination of mechano- and visual sensing with non-dimensional latencies of about 0.1 and 1, respectively.

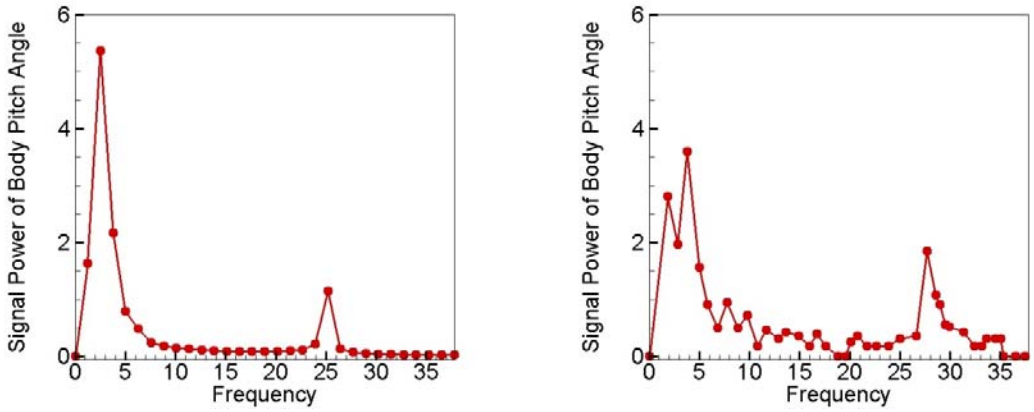

Figure 6-16 Power spectrum of pitch angle of body from (a) simplified model simulation and (b) experimental recording.

6.4.4. Horizontal and Vertical Motion in Longitudinal Plane

Finally we provide some additional data on the translational motion of the moth during stable hover as predicted by our simple models. Fig. 6-17 shows the translational motion of case 1 ($G_C^* = 0.029$, $G_V^* = 0.058$, $t_C^* = 0.1$ and $t_V^* = 1$) in the longitudinal plane From the trajectory of the motion shown in Fig. 6-17, we find that the translational drift (both horizontal and vertical) is relatively small (limited to the order of about one body length) over 20 flapping cycle. This slight drift would be easy to correct by further slight adjustments of the wing kinematics in the real moth; for instance, the downward vertical drift may be halted by a very slight increase in the flapping frequency. Similarly, forward/backward drift required modulation of the net drag force which could be done by slight changes in the phase between translation and rotation of the wing.

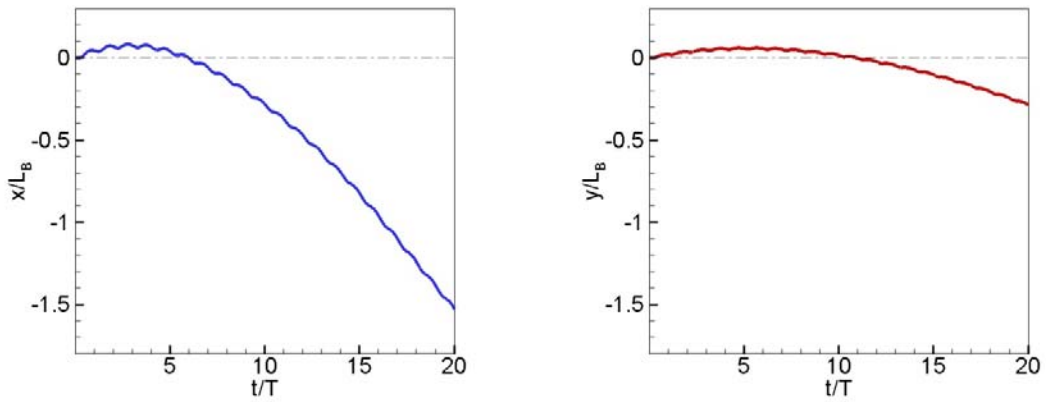

Figure 6-17 Time series of translational Distance in (a) horizontal direction and (b) vertical direction with close-loop control strategy. All the distances are normalized by the length of hawkmoth body.

6.5. Conclusion

A feedback control strategy for pitch-stabilizing hovering flight in a hawkmoth is proposed and tested. The pitch controller functions by actively attempting to maintain the stroke plane of wings in its original orientation w.r.t. to the laboratory frame regardless of body orientation. This is accomplished by allowing for a pitch control actuator that introduces relative pitch motion between the body and the wing. This strategy is based on visualization and analysis of actual hawkmoths hovering in quiescent as well as highly perturbed flows.

The feedback control also requires the introduction of a model for the sensory motor control system and the current model incorporates mechanosensory (antennae) as well as visual feedback. A simple model of these feedback mechanisms is developed that is parameterized by four parameters: two latencies and two gains.

A simplified model of the aerodynamic pitch torque is developed based on the Navier-Stokes simulations and is coupled with the 3DoF body dynamics equations to explore this large four parameter space and the simulations and these simulations indicate that a mechanosensory latency of about $0.1T$ and a visual latency of $1T$ is ideal for hover stabilization. These values are in line with those for other insects (Sane, et al, 2007; Sherrnan, et al, 2003). The simulations also allow us to determine values of gains that provide the highest degree of stability and also the overall sensitivity of the control scheme to these parameters.

A fully coupled Navier-Stokes-6DoF body dynamics simulation is conducted for two selected cases (one stable and one unstable) and the results are found to be in excellent agreement with the predictions from the simplified model. Comparisons from the

simulation data are also made with an actual hovering hawkmoth and it found that the body pitch varies over a longer time scales (6-10 flapping stroke) in a way similar to that observed in the experiments. The simulations also indicate that with these values of gains and latencies, the sensory-motor-control system hypothesized here requires control inputs that are two-orders of magnitude smaller than that required to power the flapping of the wing.

The conclusion therefore is that the strategy of maintaining the stroke plane in its original orientation by allowing relative rotational motion between the wing and the body is effective for hover stabilization and might indeed be one strategy that is used by hovering hawkmoths. Such a strategy could also be used for small flapping wing MAVs.

CHAPTER 7. CONCLUSIONS

This work explored two key questions in the aeromechanics of insect flight: what are the aerodynamic mechanisms and features that are responsible for the generation of lift in insects, and what sensory-motor control strategies could be used by insects to stabilize their flight in unperturbed as well as perturbed environments. These questions are important both from the point-of-view of organismal biology as well as the engineering design of micro-aerial vehicles.

The study employed an immersed boundary method based computational fluid dynamics code (ViCar3D) as a basic tool for this study and also employed a variety of stability analyses. Data from high speed videogrammetry is also used gain insights into the natural flight in a hawkmoth and also for validation of the simulation results.

A novel force partitioning method (FPM) is developed to clearly delineate the contribution of various aerodynamic mechanisms and features on the generation of lift force by flapping insect wings. Based on this method, the total force experienced by a body is decomposed into distinct components, each of which is associated with a clear physical mechanism. Simple cases are used to validate and assess the various force components. By using FPM, we have precisely quantified the contribution of the leading-edge vortex to lift production for two distinct insect flyers, the hawkmoth and the fruit fly. The analysis has also identified a new mechanism, what we call the *centripetal acceleration reaction*, which contributes a significant component to the total lift and it exists only in viscous flows. This mechanism, which is connected solely with the wing-kinematics, is independent of the Reynolds number and environmental flow disturbances,

and requires little power. It therefore provides an efficient and robust mechanism for weight support at all scales.

While the focus of the current paper is on insect flight, FPM has wide ranging applications to virtually all fields of fluid dynamics, and in particular, to vortex dominated flows and flows with dynamically moving bodies. Similarly, the mechanism of centripetal acceleration reaction that has been identified here likely plays an important role in flows that involve bodies undergoing complex motions such as those encountered in the flying and swimming of animals, flow induced vibration and deformation in biology and engineering, and multiphase flows.

For the flight stability of a hovering hawkmoth we start the analysis with the widely used 3DoF (longitudinal) linear time-invariant (LTI) model which indicates that moth is open-loop unstable due to instability in pitch. LTI analysis with a 6DoF model however indicates that there is an equally unstable rolling mode of instability. Comparison of a flapping and revolving wing configuration suggests that the revolving wing is significantly more unstable than the flapping wing.

By combining insight from the stability analysis with observations from high-speed videogrammetry of hawkmoths in free hovering flight, a feedback control strategy is proposed for the stabilization of hovering flight in a hawkmoth that is based on controlling the stroke angle relative to the lab-frame by allowing relative pitch between the body and wing. The strategy is testing in simulations by employing a simple model of the sensory-motor control apparatus of the hawkmoth. Simulations indicate that the strategy is effective in stabilizing the flight and the simulations also predict the allowable values of latencies and gains for the controller. The results of the stabilized hawkmoth are

compared to the experiment and similarities between the two indicate that the strategy proposed here could indeed be one of the plausible strategies that is used by the hawkmoth.

LIST OF REFERENCES

Anderson, D. A., Tannehill, J. C. and Pletcher, R. H., (1984), Computational Fluid Mechanics and Heat Transfer, Hemisphere Publishing Corporation, Taylor & Francis Group, New York.

Anderson, M. and Finlayson, L.H. (1976) The effect of exercise on the growth of mitochondria and myofibrils in the flight muscles of the tsetse fly, Glossina morsitans. J. Morph. 150: 321–326.

Balachandar, R., and Kells, J. A. (1997). Local channel scour in uniformly graded sediment: the timescale problem. Canadian Journal of Civil Engineering, 24:799-807

Batchelor, G. K. (1967) An Introduction to Fluid Dynamics. Cambridge University Press.

Birch, J. M. and Dickinson, M. H. (2001). Spanwise flow and the attachment of the leading-edge vortex on insect wings. Nature 412, 729-733.

Birch, J. and Dickinson, M. H. (2003). The influence of wing-wake interactions on the production of aerodynamic forces in flapping flight. J. Exp. Biol., 206, 2257-2272.

Birch, J. M., Dickson, W., and Dickinson, M. H. (2004). Force production and flow structure of the leading edge vortex at high and low Reynolds numbers. J. Exp. Biol., 207, 1063-1072.

Causin, P., Gerbeau, J. F. and Nobile, F. (2005). Added-mass effect in the design of partitioned algorithms for fluid-structure problems. Comput. Methods Appl. Mech. Engrg. 194:4506C4527

Chang, C.C., Yang, S.H. and Chu, C.C. (2008) A many-body force decomposition with applications to flow about bluff bodies. J. Fluid Mech. 600, 95–104

Cheng, B., Deng, X. and Hedrick T. L. (2011) The mechanics and control of pitching manoeuvres in a freely flying hawkmoth (Manduca sexta) J. Exp. Biol., 214, 4092-4106.

Demir, A. (2000) Floquet theory and non-linear perturbation analysis for oscillators with differential-algebraic equations. International Journal of Circuit and Theory Applications 28, 163-185

Dickinson, M. H., Lehmann, F.-O., and Sane, S. (1999). Wing rotation and the aerodynamic basis of insect flight. Science 284, 1954.

Dickson, W. B., Straw, A. D., Poelma, C. and Dickinson, M. H. (2006) An integrative model of insect flight control, In 44th AIAA Aerospace Sciences Meeting and Exhibit.

Dyhr, J. P., Morgansen, K.A., Daniel, T. L. and Cowan, N. J. (2012) Flexible strategies for flight control: an active role for the abdomen, J. Exp. Biol. 216, 1523-1536

Ellington, C. P. (1984). The aerodynamics of hovering insect flight. I–V.Philos. Trans. R. Soc. Lond. B Biol. Sci. 305,1 -181.

Ellington, C. P., van den Berg, C., Willmott, A. P. and Thomas, A. L. R.(1996). Leading-edge vortices in insect flight. Nature 384,626 -630.

Federle, W., E. L. Brainerd, T. A. McMahon, and B. Hölldobler. (2001) Biomechanics of the movable pretarsal adhesive organ in ants and bees. Proc. Nat. Acad. Sci. U.S.A, 986215-6220.

Felten, F.N. and Lund, T.S. (2000) Kinetic energy conservation issues associated with the collocated mesh scheme for incompressible flow, J. Comput. Phys. 215 :465–484.

Floquet, G. (1883), "Sur les équations différentielles linéaires à coefficients périodiques", Annales de l'École Normale Supérieure 12: 47–88

Forster, C., Wall, W. A. and Ramm, E. (2007). Artificial added mass instabilities in sequential staggered coupling of nonlinear structures and incompressible viscous flows. Comput. Methods Appl. Mech. Engrg. 196:1278C1293

Fry, S. N., Rohrseitz, N., Straw, A. D. and Dickinson, M. H. (2009) Visual control of flight speed in Drosophila melanogaster, J. Exp. Biol. 212, 1120-1130

Gao, N., Aono, H., HaoLiu, (2010) Perturbation analysis of 6DoF flight dynamics and passive dynamic stability of hoveringfruitfly Drosophila melanogaster, Journal of Theoretical Biology 270:98-111

Ghias, R., Mittal, R. and Dong, H. (2007) A sharp interface immersed boundary method for viscous compressible flows, J. Comput. Phys. 225:528–553.

Hedrick, T. L. and Daniel, T. L. (2006). Inverse problems in the flight control of the hawkmoth Manduca sexta. J. Exp. Biol. 209, 3114-3130

Hinterwirth, A. J. and Daniel, T. L. (2010) Antennae in the hawkmoth Manduca sexta (Lepidoptera,Sphingidae) mediate abdominal flexion in response to mechanical stimuli, J Comp Physiol A, 196, 947–956

Howe, M. S. (1995). On the force and moment exerted on a body in an incompressible flow. Q. J. Mech. Appl. Maths 48:401-426

Lamb, H. (1932) Hydrodynamics. Dover.

Lighthill, M. J. (1986) An Informal Introduction to Theoretical Fluid Dynamics. Oxford University Press.

Mamiya, A, Straw, A. D., Tómasson, E., Dickinson, M. H. (2011). Active antennal movements enhance visually-guided steering in flying Drosophila. J Neurosci. 31, 6900-6914.

Maimon, G., Straw, A.D., Dickinson, M.H. (2010). Active flight increases the gain of visual motion processing in Drosophila. Nature Neuroscience 13, 393-399.

Mamiya, A., Straw, A. D., Tomasson, E. and Dickinson, M. H. (2011), Active and passive antennal movements during visually guided steering in flying Drosophila, The Journal of Neuroscience, 31:6900–6914

Mavriplis, D. J. and Venkatakrishnan, V. (1994) Agglomeration multi-grid for viscous turbulent flows. AIAA Paper 94-2332

Mittal, R., Dong, H., Bozkurttasa, M., Najjarb, F.M., Vargasa, A. and von Loebbecke, A. (2008). A versatile sharp interface immersed boundary method for incompressible flows with complex boundaries. J. Comp. Phys. 227:4825-4852

Mok, D. and Wall, W. (2001) Partitioned analysis schemes for the transient interaction of incompressible flows and nonlinear flexible structures, in: W.A. Wall, K.-U. Bletzinger, K. Schweizerhof (Eds.), Proceedings of Trends in Computational Structural Mechanics, 689–698.

Noca, F., Shiels, D., Jeon, D. (1999) A comparison of methods for evaluating time-dependent fluid dynamic forces on bodies, using only velocity fields and their derivatives. J Fluids Struct 13:551–578

Noda, R., Nakata, T. and Hao Liu. H., (2014) Body flexion effect on the flight dynamics of a hovering hawkmoth. Journal of Biomechanical Science and Engineering. 14-00409

Prasadd, A. and Williamson, C. H. K. (1997) Three-dimensional effects in turbulent wakes, Experimental, Thermal and Fluid Science, 14, 9.

Press, W. H., Teukolsky, S. A., Vetterling, W. T. and Flannery, B. P. (1992) Numerical Recipes in C: The Art of Scientific Computing. Second Edition, Cambridge University Press, New York

Quartapelle, L. and Napolitano, M., (1983). Force and moment in incompressible flows. AIAA Journal, Vol. 21, 911–913

Ragazzo, C. G. and Tabak, E. G. (2007) On the force and torque on systems of rigid bodies: a remark on an integral formula due to Howe. Phys. Fluids 19, 057108.

Ramamurti, R. and Sandberg, W. C. (2002). A three-dimensional computational study of the aerodynamic mechanisms of insect flight. J. Exp. Biol. 205:1507-1518.

Roshko, A. (1954) On the Development of Turbulent Wakes from Vortex Streets. N.A.C.A. Rep. 1191.

Sane, S. P. and Dickinson, M. H. (2001). The control of flight force by a flapping wing: lift and drag production. J. Exp. Biol. 204:2607C2626

Seo, J. H. and Mittal, R. (2011) A sharp-interface immersed boundary method with improved mass conservation and reduced spurious pressure oscillations. J. Comput. Phys. 230, 7347–7363

Sherman, A. and Dickinson, M. H. (2003). Summation of visual and mechanosensory feedback in Drosophila flight control. J. Exp. Biol. 207:133-142

Spedding, G. R. (1986). The wake of a jackdaw (Corvus monedula) in slow flight. J. Exp. Biol. 125, 287–307.

Spedding, G. R. and Maxworthy, T. (1986). The generation of circulation and lift in a rigid two-dimensional fling. J. Fluid Mech. 165:247-272

Straw, A. D., Lee S. and Dickinson, M. H. (2010) Visual control of altitude in flying drosophila, Current Biology 20, 1550–1556

Stuben, K., (2001). A review of algebraic multigrid, Journal of Computational and Applied Mathematics (JCAM) 128, 281-309.

Sun, M. and Xiong, Y. (2005) Dynamic flight stability of a hovering bumblebee. The Journal of Experimental Biology 208, 447-459

Sun, M., Wang, J. K. and Xiong, Y. (2007) Dynamic flight stability of hovering insects. Acta Mech. Sin. 208,447–459.

Tan, B. T., Thompson, M. C. and Hourigan, K. (2005) Evaluating fluid forces on bluff bodies using partial velocity data. J. Fluids Struct. 20, 5–24

Taylor, G. K. and Thomas, A. L. R. (2003). Dynamic flight stability in the desert locust Schistocerca gregaria. J. Exp. Biol. 206, 2803-2829.

VandenBerg, C. and Ellington, C. P. (1997a). The three-dimensional leading-edge vortex of a hovering model hawkmoth. Phil. Trans. R. Soc. Lond. B 352:329-340.

Van kan, J. (1986) A second-order accurate pressure correction scheme for viscous incompressible flow, SIAM Journal on Scientific and Statistical Computing. 7, 870 – 891

Weis-Fogh., T. (1973) Estimate of flight fitness in hovering animals, including novel mechanisms for lift production, The Journal of Experimental Biology, 59,169-230

Wu, J. C. (1981). Theory for aerodynamic force and moment in viscous flows, AIAA Journal, 19, 432-441.

Wu, J. H. and Sun, M. (2012) Floquet stability analysis of the longitudinal dynamics of two hovering model insects, J. R. Soc. Interface, 9, 2033–2046

Wu, J. Z., Ma, H. Y and Zhou, M. D. 2006 Vorticity and Vortex Dynamics. Springer

Wu, J. Z., Lu, X. Y. and Zhuang, L. X. (2007) Integral force acting on a body due to local flow structures. J. Fluid Mech. 576:265-286.

Wu, J. H., Zhang, Y. L. and Sun, M. (2009) Hovering of model insects: simulation by coupling equations of motion with Navier–Stokes equations. J. Exp. Biol. 212, 3313–3329.

Ye, T., Mittal, R., Udaykumar, H.S. and Shyy, W. (1999) An accurate Cartesian grid method for viscous incompressible flows with complex immersed boundaries, J. Comput. Phys. 156 : 209–240

Zang, Y., Streett, R.L. and Koseff, J.R. (1994) A non-staggered fractional step method for time-dependent incompressible Navier–Stokes equations in curvilinear coordinates, J. Comput. Phys. 114 : 18–33.

Zheng, L., Hedrick, T. L. and Mittal, R. (2013) A comparative study of the hovering efficiency of flapping and revolving wings, Bioinspiration and Biomimetics, 8, 036001-13

Zheng, L., Hedrick, T., Mittal, R. (2013). A multi-fidelity modelling approach for evaluation and optimization of wing stroke aerodynamics in flapping flight. J. Fluid Mech. 721:118- 154

Zheng, X., Xue, Q., Mittal, R. and Beilamowicz, S. (2010) A coupled sharp-interface immerse boundary-finite element method for flow-structure interaction with application to human phonation, Journal of Biomechanical Engineering, 132:111003

Vita

Chao Zhang received the Sc. B. degree in Engineering Mechanics in 2007, and Master of Science in Engineering Mechanics from Tsinghua University in 2010. From 2010 to 2015, he was pursuing doctoral degree in Mechanical engineering at Johns Hopkins University under the guidance of Prof. Rajat Mittal.

Starting in March 2015, Chao Zhang will work for Covergent Science Inc., where he will conduct CFD simulation/development and provide the solution to the industry professionals.